

# **POLITECNICO DI TORINO**

Corso di Laurea Magistrale  
in Ingegneria Meccanica

Tesi di Laurea Magistrale

**Mechanical characterization of Ti-6Al-4V lattice structures  
manufactured by Electron Beam Melting process (EBM)**



**Relatore:**

Prof. Luca Iuliano

**Co-relatori:**

Ing. Manuela Galati

Ing. Abdollah Saboori

**Candidato:**

Giuseppe Del Guercio

Anno Accademico 2018/2019

# 1 Literature Review

## 1.1 Introduction

The study on Titanium (Ti) alloys started 40 years ago, mainly for the aerospace sector because of the high specific properties of these alloys [1–3]. However, Ti alloys are today considered extremely important for the high corrosion resistance and the high biocompatibility with human tissue. The melting point of pure Ti is around 1670°C for which occurs the allotropic transformation from a hexagonal structure  $\alpha$  (HCP), stable at low temperature, to a body-centered cubic structure  $\beta$  (BCC), stable at high temperature [3–5]. Ti-6Al-4V is a  $\alpha+\beta$  Titanium alloy; due to the presence of  $\beta$ -stabilizing elements such as Vanadium, the transformation is unfinished at room temperature, resulting in a mixture of  $\alpha$  and  $\beta$  phases [6–8]. Starting from a total  $\beta$  field and cooling the alloy, around 995°C the transformation from the  $\beta$  phase to the  $\alpha$  phase starts. This specific temperature is named  $\beta$ -transus [9]. The kinetics of the transformation affects the constitution of the phases and their relative volume ratio in the alloy, which, on the other hand, affects the properties of the resulted alloy. During the rapid cooling from the temperatures above the  $\beta$ -transus temperature, the  $\beta$  phase transforms to a metastable  $\alpha'$  martensite phase through a diffusionless transformation [1]. It is indeed reported that this diffusionless transformation results in the formation of fine colonies of laths [3].

Focusing on the Ti-6Al-4V alloy, it has been found that a balance of the  $\alpha$  and  $\beta$  phases is the best way to enhance the mechanical properties [10]. In the Ti-6Al-4V production, traditional melting techniques like casting have shown to suffer from several limitations, such as the need to remove high-density inclusions (HDI) and low-density inclusions (LDI) to provide composition homogeneity [10]. Moreover, this alloy exhibits high surface oxidation, especially at high temperatures. In the last few years, the scientific community focused on new ways to fabricate titanium made parts to reduce the presence of the cited defects. Particularly, Additive Manufacturing (AM) has become one of the most interesting new fabrication techniques to produce titanium components [5,11,12].

AM technologies are defined as “processes of joining materials to make objects from 3D model data, usually layer upon layer, as opposed to subtractive manufacturing methodologies” [13]. This kind of approach allows the production of parts with free design constraint enabling the construction of integrated components, lightweight structures or topologically optimized geometries [2,14–16]. At the industrial level from the beginning of

the 21<sup>st</sup> century, there has been an increment of interest in AM technologies due to their large production flexibility, both on the cost and lead-times [17]. In the last few years, the industrial sector interest has been focused mainly on metal AM for aerospace, automotive and medical applications [17]. For aerospace and automotive applications, the main drivers for the AM introduction as a production technique are the possibility to obtain lightweight components and integrated parts [14]. For medical applications, instead, the main driver is the possibility to obtain personalized implants which allow the reduction of the recovery times, due to the better interaction with prior tissues [14]. Metal AM techniques can be divided into Powder Bed Fusion (PBF) techniques [18–21] and Directed Energy Deposition (DED) techniques [22–24]. PBF systems are systems in which “thermal energy selectively fuses regions of a powder bed” [13]. The main advantages of this kind of approach are the ability to build workpiece with complex details and assure a good dimensional control, due to the excellent resolution of these systems [11]. The most common PBF techniques in the industrial field are Laser PBF, also known as Selective Laser Melting (SLM), and Electron Beam Melting (EBM).

Among the metal AM processes, EBM has been already used for mass production for aerospace and medical applications. EBM is able to build complex geometry workpieces with great precision [25–27]. Different materials such as stainless steel [28], tool steel [29], Ni-based superalloys [21], Ti-alloys [25,30] and intermetallics like TiAl [25,31], particularly for the aerospace, automotive and medical [32] sectors, can be processed by EBM [31]. Among the Ti alloys, Ti-6Al-4V alloy is today the most attracting alloy for the EBM.

During the EBM process, an electron beam (EB) with high power selective melts metallic powder using. Arcam AB, Sweden, has developed the first EBM system which mainly consists of two main elements: the column in the upper part of the system, and the work chamber in the lower part of the system [33]. The EB is produced by a tungsten filament [34] or a LaB<sub>6</sub> crystal located in the column in which an anodic potential of 60 kV is applied. The electrons are accelerated up to 10-40% the speed of light [35], and they are guided from the top gun towards the working chamber. The EB is controlled by three sets of coils, also called electromagnetic lenses [36]. The first set of coils (astigmatic lenses) controls the shape and the deflection of the electron beam, the second set (focus lenses) controls the focus of the beam, and the last set (deflection lenses) controls the size of the beam [37]. Despite having a small mass, the accelerated electrons have a remarkable amount of kinetic energy, that is converted in heat when the electrons impact the powder bed. This energy ensures the melting of the metallic particles [38].

During the process, the working chamber is maintained under vacuum to avoid the deflection of the electrons due to air molecules. To assure these conditions, EBM systems are equipped with a turbo-molecular pump [38]. The typical residual gas pressures are  $10^{-3}$  Pa in the working chamber and  $10^{-5}$  Pa in the column [25]. Unlike the other PBF process, the EBM process starts with a preheating of the powder bed by using a defocused EB, high beam current and speed values. The preheating phase sinters the powder bed and facilitates the heat conduction. The typical preheating temperature for Ti-6Al-4V alloy is around 650°C-700°C [9,39]. EBM process is considered as a hot process. In fact, due to the presence of preheating before the melting phase and the vacuum environment, the working temperature in the chamber is approximately equal to the preheating temperature. This aspect ensures small thermal shrinkages and a medium grade of sintering between the particles that results in a certain strength of powder bed [40]. For these reasons, a small number of supports, mainly to distribute uniformly the amount of heat provided during the melting, is required to produce metallic components through the EBM process. After the melting phase, an additional step, called post-heating, takes place [41]. In this step, the layer can be either cooled down or further heated depending on the total amount of energy supplied during the previous steps. Thereafter, the start plate is lowered, and the powder is spread by the raking system [41], and the process is repeated up to the part is completed. When the workpiece construction is finished, the whole part cools down inside the EBM chamber, under a helium flux [42]. When the workpiece is removed from the working chamber, the part is entirely covered with a soft agglomerate powder called breakaway powder [42]. To remove this material, a sandblasting process is required. To allow the re-use of the powder and avoid contamination, the same powder processed in the EBM process is used for the sandblasting operation [43]. The typical residual pores in the as-built EBM parts are below 100  $\mu\text{m}$  [44]. The presence of these pores may be due to residual gas pores in the particles from the gas atomization process, lack of fusion and tunnel defects. According to the application, to close those residual porosities hot isostatic pressure (HIP) treatment is usually run after the EBM process [44–49]. The reduction of such defects allow an improvement of the fatigue and compression behaviour of the part.

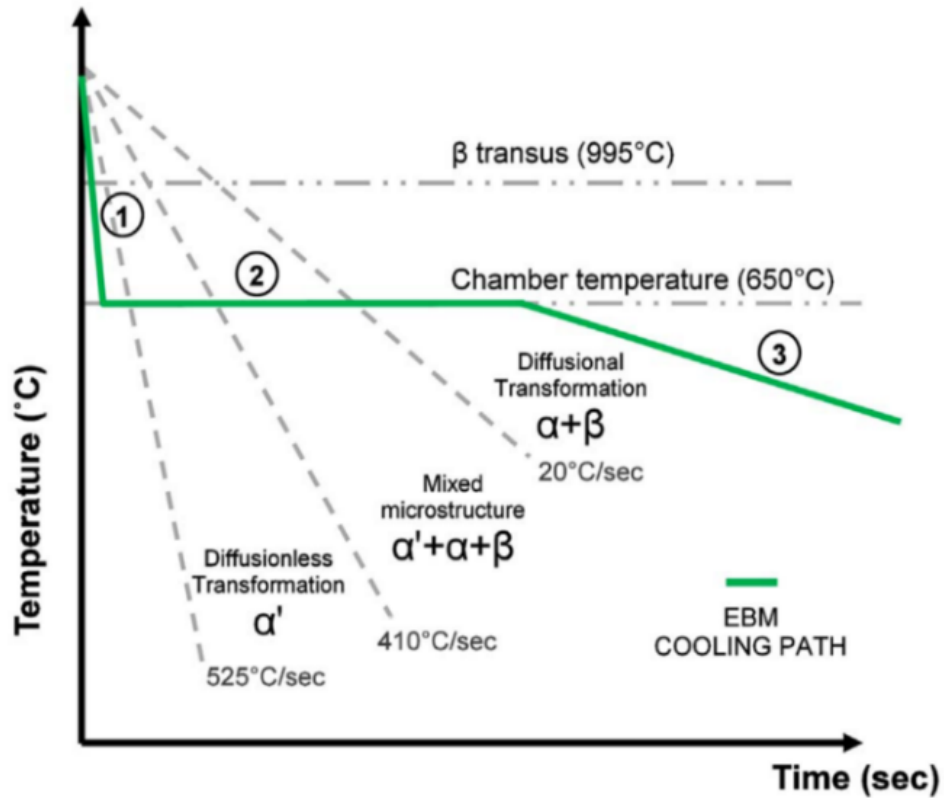


Figure 1: Thermal evolution in the EBM process [9]

During the EBM process, three main stages can be considered for the Ti-6Al-4V transformation as shown in Figure 1 [9]. The first stage is characterized by a high cooling rate and leads a diffusionless transformation that transforms the  $\beta$  phase in  $\alpha'$  martensite. During the second phase, several diffusional transformations change the microstructure into a mixture of fine  $\alpha+\beta$  phases at a constant temperature of about 650°C-700°C [9,39]. At these temperatures, the diffusion causes the decomposition of the martensite phase  $\alpha'$ . In the third and last phase, the diffusion causes a coarsening of the microstructure, with a final microstructure of  $\alpha+\beta$  phases with a specific laths size of about 1.4  $\mu\text{m}$  [9].

Differently from the EBM, Laser PBF techniques do not perform preheating, thus the temperature after the scanning phase drops immediately up to the ambient temperature. In these conditions, a diffusionless transformation occurs causing the formation of the martensitic phase. Differently from the EBM process, in the cited temperature conditions the diffusion of the ligand elements does not occur due to kinetic reasons. Thus, the decomposition of  $\alpha'$  does not occur and the final microstructure is so characterized by fine martensite  $\alpha'$ .

Regarding the EBM process, several literature studies have been focused on the microstructure modifications by subsequent heat treatments on bulk material [9,30,44,47–50]. Particularly of interest to be produced by the EBM process are the micro-architected

or so-called cellular materials. In the last few years, these materials have been largely addressed due to the possibility to achieve a design with a unique combination of properties [51] such as mechanical, thermal and acoustic properties [52]. As an example, topology optimization design technique has been used to tune the thermal expansion (CTE) coefficient for the design of a high-performance heat exchanger [53]. Among the cellular materials, foams and random topology structures have shown a good impact resistance [54]. Differently from the foams, lattice structures belong to the cellular material family that does not have a stochastic structure. A lattice material was defined by Fleck et al. [51] as a cellular, reticulated, truss, mesh arrays or lattice structure made up of a large number of uniform lattice elements and generated by tessellating a unit cell, comprised of just a few lattice elements, throughout space. A lattice cell consists of a certain number of struts, also called lattice struts, that are jointed in one or more nodes. Therefore, a lattice strut is a link between two nodes. Arranging differently the connections between the nodes with lattice struts, different types of unit cells can be designed. The characteristic dimension of the unit cell is named unit cell size. On the other hand, the peculiar dimensions of the struts are the strut size, which represents its diameter, and the strut length, namely the distance between two nodes linked by a strut.

The construction of lattice structures with traditional techniques results to be expensive due to the numerous cutting and welding phases required or even impossible [55]. Due to the possibility to build such structures without supports and using a nesting strategy, EBM process offered an effective way to realize this kind of structures economically. Jointly to the use of Ti-6Al-4V or Ti-6Al-4V ELI, the EBM structures showed high specific properties such as specific strength [56], oxidation resistance [56,57] and biocompatibility with human tissues [57,58]. The behaviour and properties of this kind of structures have been showed to be dependent from the design and process [53,59,60]. For this reason, efforts have been carried out to understand and characterize the Ti-6Al-4V lattice structures made by the EBM process. The presented work's aim consists of a systematic and comprehensive review of the current state of the art on the mechanical characterization of the Ti-6Al-4V lattice structures made by the EBM process. To provide a comprehensive overview, the literature has been reviewed according to the aspects that mainly affect the mechanical behaviour of the lattice structures. The aspects have been categorized considering the EBM process at the center of the characterization. Therefore, the main steps to produce EBM part were considered as guidelines to review the literature on the lattice performance: 1) design 2) process and 3) post heat treatment. For the just cited reasons, the paper has been organized as follows. Firstly, the investigation on the effect of the design of the lattice structure on the mechanical properties

has been presented. The effect of relative density obtained by different lattice design has been reviewed as well as the models to forecast the lattice properties. Then, the effect of the precision of the EBM process on the lattice structure has been investigated, especially looking for the deviation between the design and the actual structure. At the end, the studies on the effects of the heat treatments on the mechanical properties have been reviewed.

## **1.2 Mechanical behaviour of Ti-6Al-4V lattice structures made by EBM**

The properties of cellular materials extend the range of features available to design a component.

Figure 2 shows the variation of the design properties range illustrated by Ashby and Gibson [61]. Moving from true solids to foams, the presence of air gaps inside the material causes a reduction of density, conductivity, Young modulus and strength. Ashby identified three main factors that influence the properties of cellular materials: 1) material of which is made, 2) cell topology and shape, 3) relative density [62]. The first factor affects the mechanical, thermal and electrical properties. Cell topology and shape are relevant to the behaviour distinction between bending and stretching-dominated structures [63]. The relative density, which is the ratio between the density of cellular material  $\rho^*$  and the density of the bulk material  $\rho_s$ , affects the general properties of cellular solids [61].

Deshpande et al. [63] introduced the classification of cellular materials according to their collapse response under load. This classification distinguished the structures into bending-dominated or stretching-dominated. In bending-dominated structures, the behaviour of the cellular material is based on the rotational stiffness and strength of nodes and struts [51]. Foams exhibit most likely a bending-dominated behaviour, while the lattice can be both stretching-dominated or bending-dominated materials [63]. The macroscopic behaviour of the lattice structure, therefore, depends on the axial stiffness and strength of the struts [51]. Maxwell studied the equilibrium and stiffness of frames [64] and provided a criterion to discern stretching and bending-dominated structures, which has been validated by the studies of Deshpande et al. [63]. According to this criterion, in a 2D rhombic structure if a longitudinal beam is inserted the vertical stiffness of the frame is given by the axial stiffness of the longitudinal beam itself [64].

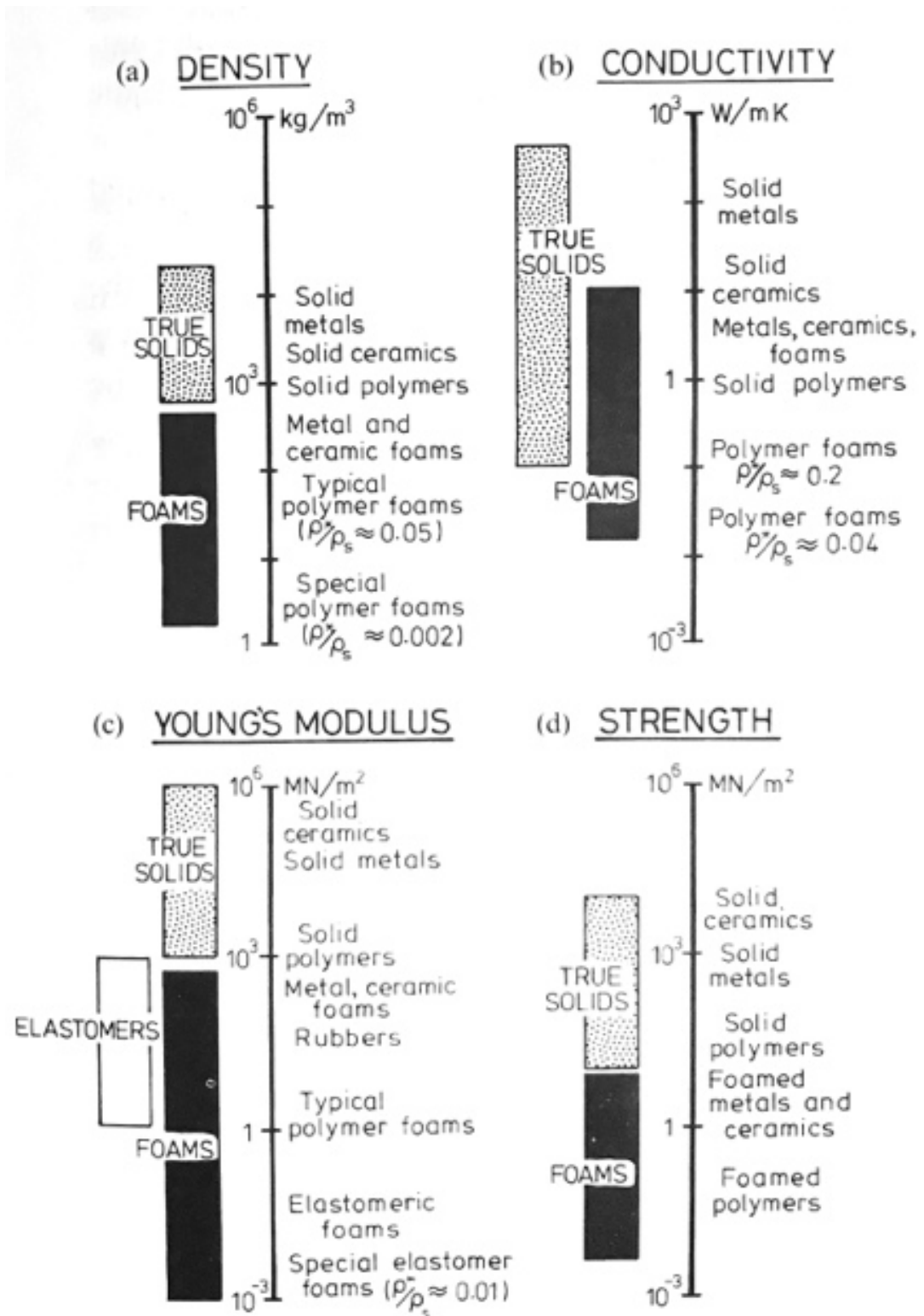


Figure 2: The range of properties available to the engineer through foaming: (a) density; (b) thermal conductivity; (c) Young modulus; (d) compressive strength [61]

Murr et al. studied cellular structures with a specific aim to investigate their mechanical properties and microstructure in the as-built condition [56]. From a material point of view, they conducted SEM analysis in order to investigate the microstructure of the foams and

lattice structures. The results showed a great presence of  $\alpha'$  martensite, given by the high cooling rate of cellular solids. The presence of large air gaps between the struts causes a rapid temperature drop to the working chamber temperature.

In a more recent work, Murr et al. evaluated the differences between the microstructure a fully dense and foam specimens [65]. In comparison with their previous work [56], the aim of this work [65] was to investigate the differences between cellular solids and bulk specimens. As it is possible to see from Figure 3, the microstructure of the bulk material is given by a coarse mixture of  $\alpha$  and  $\beta$  phases. The foam shows a finer microstructure with the presence of  $\alpha'$  martensite. This work confirmed that the topology of the material has a big impact on which phases the microstructure is made by [65].

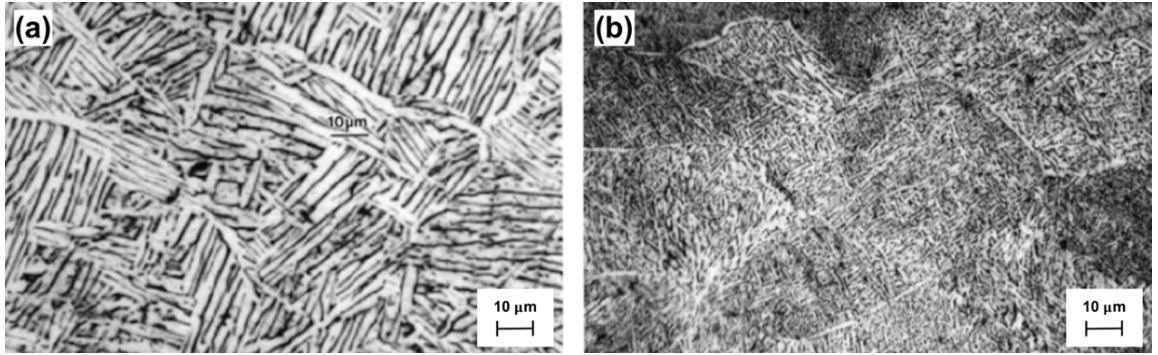


Figure 3: Optical micrographs showing different microstructures for a bulk material (a) and a foam (b) [65].

### ***1.2.1 The behaviour of the lattice structure under compression test: experimental and numerical models***

Ashby and Gibson [61] proposed the first model to describe a property of the generic cellular material as a linear function in a logarithmic scale graph of its relative density. Considering the mechanical performance under compressive load, one of the most important properties to estimate is the compressive Young modulus. Ashby and Gibson proposed the following relationship [61]:

$$\frac{E^*}{E_s} = C_1 \left( \frac{\rho^*}{\rho_s} \right)^2 \quad (1)$$

Here  $E^*$  and  $\rho^*$  are respectively the Young modulus and the material density. The star values are referred to the cellular material, while the ones sub-s are referred to the bulk material.  $C_1$  is a constant. For the lattice structure  $C_1$  was assumed to be equal to 1 [56,60,65] despite its value can be slightly affected by the cell shape. Another important property is the Ultimate Compressive Strength (UCS\*), which can be evaluated through the following expression:

$$\frac{UCS^*}{UCS_s} = C_5 \left( \frac{\rho^*}{\rho_s} \right)^{3/2} \quad (2)$$

Here,  $C_5$  is an empirical constant which is determined experimentally. Murr et al. [56] assumed a  $C_5$  value equal to 1.5 while it was 2.2 in [60]. These variations on the value of the cited constant is caused by the different cell type.

Murr et al. [56] showed that while the foam behaviour is well described by its relative density, the lattice properties are also influenced by the topology and dimensions of the unit cell.

Differently, Cheng et al. [60] investigated the differences between the mechanical properties of lattice and foams. They indeed evaluated the compression behaviour of cellular solids with two different topologies: foam and rhombic dodecahedron shaped lattice structure. The samples showed brittle fractures with crush bands at an angle of approximately  $45^\circ$  for lattice structure, while the foam failures occurred at a random angle. The specific strength of lattice structures has been found to be higher than the foams with the same specific stiffness. This result occurs due to the microstructural difference between foams and lattice. Lattice structures, as said, show fine  $\alpha'$  martensite, while foams show a coarser microstructure.

Both Murr et al. [56] and Cheng et al. [60] evaluated Young modulus of lattice structures at different relative density using the resonant frequency method and the damping analysis. Similar to the Ashby-Gibson model, lattice structures followed a linear law in a logarithmic scale graph with different exponents. On the other hand, studying the effect of density and feature size on mechanical properties Hernández-Nava et al. found that only for specific structures the Ashby-Gibson model for the prediction of Young modulus and the compressive strength can be accurate enough to model the structure behaviour [66]. Differently, Mortensen et al. proposed an analytical approach in which the porous structure is designed by interpenetrating spheres simulating the pores where the porosity variations were obtained just moving the centres of the spheres [67]. Since the topology of the structure used has not changed, the increase in the strut size entails an increase also in the Young modulus and the Ultimate Compressive Strength. Similarly to Mortensen et al. [67], Horn et al. suggested a modification of the Ashby-Gibson model specifically for the compressive behaviour of lattice structure made by rhombic dodecahedron open cells [68]. To evaluate the size effect, three sets of specimens with different cell sizes have been investigated. The strut size has been changed to evaluate the effect of relative density and strut thickness for each batch of samples. Differently from the previous analysed works, flexural tests were conducted to evaluate the relative Young modulus with respect to the relative density. From the analysis of the results, it was detected that the Ashby-Gibson relationship is an appropriate approximation of the experimental behaviour.

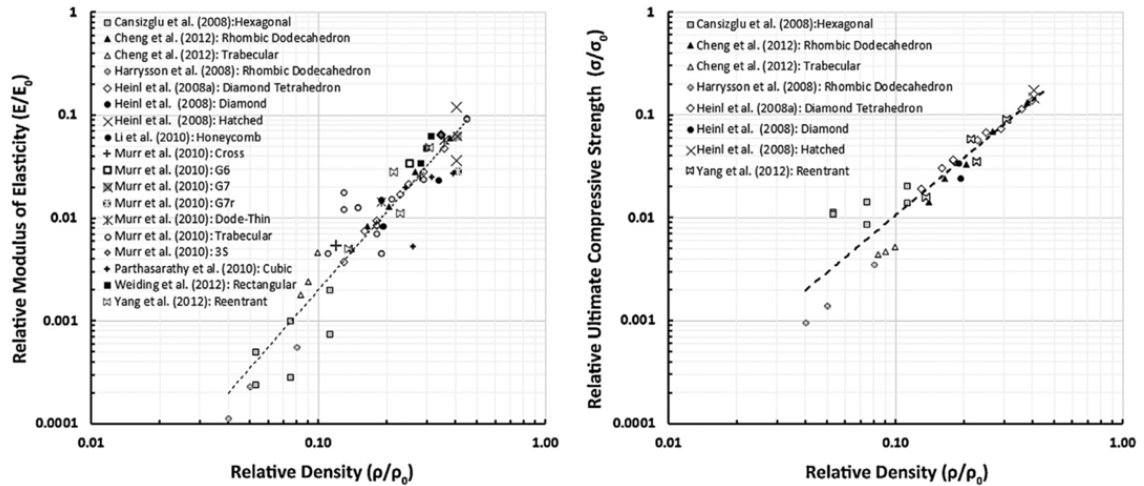


Figure 4: charts summarizing the relationship between relative density and relative modulus of elasticity (a) and relative compressive strength (b) derived from Ti-6Al-4V cellular structures [68].

Horn et al. also presented two useful charts that collected a considerable number of experimental data from literature papers regarding the mechanical characterization of cellular structures (Figure 4) [68]. Both on the relative modulus of elasticity (Fig.4a) and the relative UCS (Fig.4b), laws similar to Equation 1 and Equation 2 were found to yield acceptable forecast. Experimentally, Cansizoglu et al. [69] evaluated the behaviour under uniaxial compressive conditions (to evaluate the Ultimate Compressive Strength) and flexural conditions (to evaluate Young modulus) of the honeycomb lattice structures with different strut sizes [69]. A linear law in a logarithmic scale graph between mechanical properties and relative density was detected. The same kind of relationship between the relative density and both the relative UCS and Young modulus was shown to exist also by Parthasarathy et al. [70]. In their study, a cubic lattice structure was analysed by four sets of specimens with different pores and strut sizes, with an overall designed porosity ranging from 60.91% to 75.83%. They stated that the difference between the Ashby-Gibson model and the experimental results occurred due to the size of the specimens used for the experiments. In fact, the Ashby-Gibson model for cellular solids [61] assumed a structure with an infinite number of pores. Practically, such structure could be obtained only reducing the dimensions of the cell that may be incompatible with the EBM process due to the process precision [68,70] and also to the need to remove the powder entrapped inside the cell [42,68]. The differences between theoretical and experimental results could also be explained by the irregularities and corrugations of the surface of the struts [70] that will be discussed further. To predict the elastic modulus of porous lattice structures a Finite Element Analysis (FEA) model based on the volume element method (RVE method) [71,72] was developed by

Parthasarathy et al. [73]. The design of the lattice structures adopted in the application of the RVE method was as same as the previous work [70], and the results showed that for porosities ranging from 28.18% to 78.14% the relative elastic modulus progressively decreases (Figure 5).

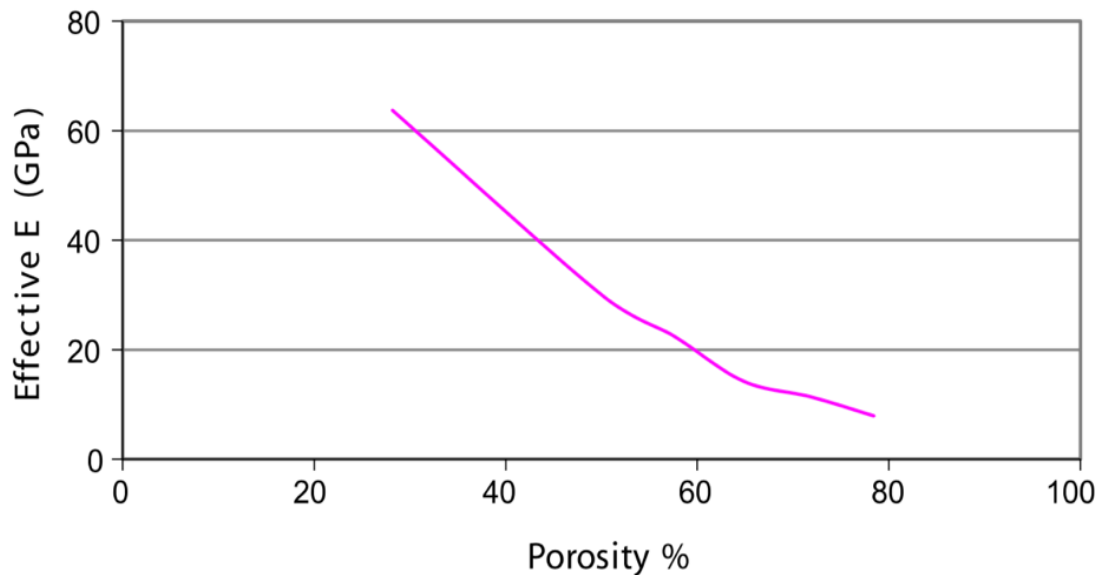


Figure 5: Variation of Effective E as a function of porosity [73]

The comparisons between numerical and experimental results showed a better prediction of Young modulus at high relative density, meaning a more precise model response for lattice structure with a low porosity content. The compression results showed that lattice structures with graded porosity could be a good application both for craniofacial implants and hip implants since the range of elastic modulus and compressive strength cater to the requirements of the loading conditions of actual bones [62]. Compressive strength for the diamond lattice structures with graded porosity was evaluated by van Grunsven et al. [74]. Four sets of the structure were produced; for three of them, a fixed unit cell side length was used. Different relative densities were obtained only varying the strut thickness. The last design was made by three layers, each one with a height of 2 mm and made of one of the previous designs to obtain a graded porosity structure. An increasing in both compressive strength and Young modulus with the relative density and the strut thickness was revealed.

The stress-strain curves of graded lattice specimens are shown in Figure 6. The black line indicates the predicted form of the stress-strain curve calculated upon the data obtained from the tests conducted on uniform lattice structures, while the coloured lines indicate the stress-strain curves obtained for all the three graded specimens. All curves showed a clear collapse on the individual layer. A formulation for predicting the Young modulus of a graded lattice

structure has been proposed assuming a simple series of uniform layers of the same thickness. In the iso-stress conditions that correspond to axial compression, the rule of the mixture has been applied to calculate the elastic modulus of the whole structure [74]:

$$\frac{1}{E_{graded}} = \frac{1}{3E_1} + \frac{1}{3E_2} + \frac{1}{3E_3} \quad (3)$$

In Equation 3  $E_{graded}$  is the Young modulus of the graded lattice structure, whereas  $E_1$ ,  $E_2$  and  $E_3$  are the Young modulus of each layer of the whole structure. This result is useful in the design process of orthopaedic implants in which the possibility to tune the mechanical characteristics and the relative density according to the properties of the actual bone structure could be a turning point for this kind of applications in the medical sector.

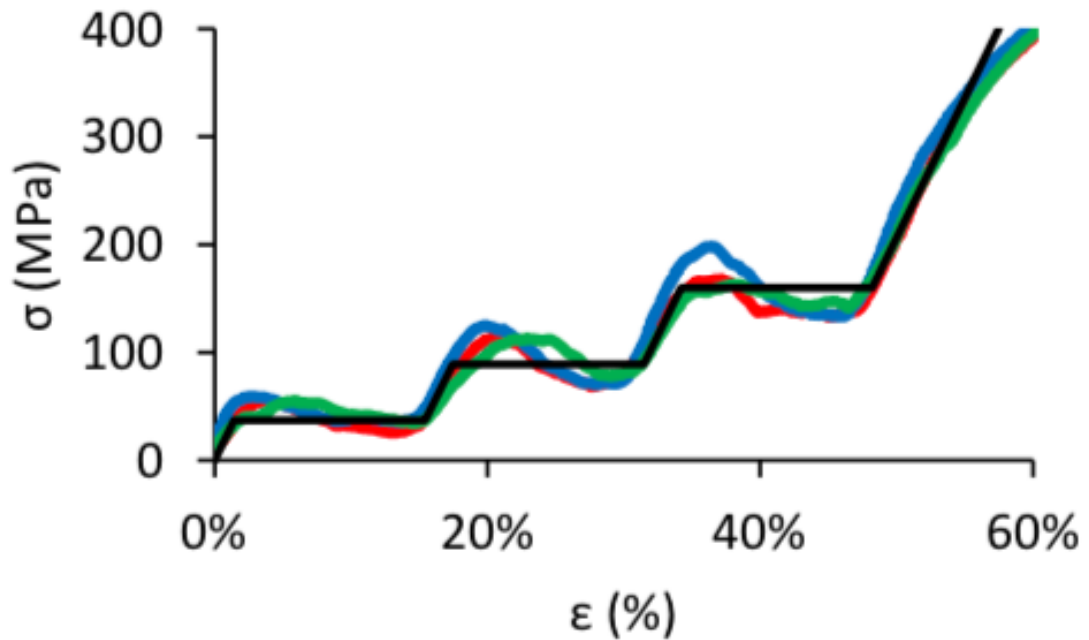


Figure 6: Mechanical behaviour of the graded lattice structure [74]

Remaining in the medical application field, Heinel et al. studied cross and diamond unit cells with interconnected macro porosity made by EBM for bone implants applications [59]. Differently from the previous analysed studies, they were focused on the effects of chemical surface modification on the mechanical behaviour and biocompatibility features of lattice. For the bioactivity test, several chemical etchings were performed. The derived results showed the apatite formation in simulated body fluid under dynamic conditions that provided better fixation of the implant in the prior tissues and bones. Cross unit cell structures showed better mechanical characteristics due to lower porosity content with respect to diamond structures. This result is consistent with the Ashby-Gibson model [61]. In addition, the values of elastic modulus were found to be coherent with human bone values.

Moving to the dental application field, Jamshidinia et al. [75] studied three different unit cells (cross, honeycomb and octahedral) with different cell sizes. The aim of their work was to provide a dental abutment with specific elastic micro-motion. Larger size caused an increase in total elastic deformation and, therefore, the higher elastic modulus could be obtained by using smaller dimensions. Comparing the results between the different unit cells types, the honeycomb is the stiffer lattice while the least stiff structure is the cross-unit cell. This result occurs because the cross-unit cell shaped lattice structures show a higher number of stress concentration points with respect to the lattice structures made of other unit cell type.

Jamshidinia et al. [75] also proposed a numerical simulation for predicting the mechanical response, varying the angle of the load. The numerical results showed that for angles above  $30^\circ$ , the maximum stress decreases [51]. This phenomenon was explained as a failure of the structure when the higher stress levels are over the yield stress. Fatigue properties have also been investigated [76]. The experimental results showed that with the increase of the load, the life of the specimens decreases. The comparisons between the experimental and numerical data suggested that the best way to correct the mean stress is the Soderberg relationship. According to the numerical results, the sharp corners of the structures are the most stressed points. The reduction of fatigue life is suggested to occur much frequently with high levels of surface roughness, especially in lattice structures with a low strut size.

Epasto et al. studied rhombic dodecahedron lattice structures investigating the effect of unit cell size [77]. After the conduction of the compressive tests, it was possible to conclude that with an increase of the cell size both the compressive strength and Young modulus decrease. This result occurs because with a reduction of the cell size, the relative density of the whole material increases. Thus, since lattice structures follow the Ashby-Gibson relationship, an increase in both compressive strength and Young modulus is expected [61].

Table 1 collects all the testing conditions of the mechanical tests conducted in the literature. As can be observed from the previous discussion and Table 1, the conducted experiments cannot be easily compared because different standards, different structure and different ultimate load conditions have been analysed in the studies. However, the main findings of all the investigated studies confirmed that the lattice properties are influenced by the design and dimensions of the unit cell, as stated earlier by Murr et al. [39]. Most of the initialised paper used the relative density as the main descriptor of mechanical behaviour. Figure 7 collects the results found in terms of Young modulus of the reviewed studied according to the Ashby and Gibson model which confirm a net relationship with respect to the relative density [61].

Table 1: Testing conditions for compression tests conducted in literature.

Ref.	Test typology	Adopted Standard	Ultimate load condition	Strain velocity [mm/min]	Strain rate [s <sup>-1</sup> ]
[70]	Compression	ASTM D695-02	Until Failure	1	
[69]	Compression			5	
	Flexural			1	
[74]	Compression		Until 50% of the original size	0.25	
[52]	Compression		100 kN		
[78]	Compression		Until total strain exceeded 65%	0.9	0.001
[79]	Compression		50 kN – 5 kN		
[75]	Compression		400 N		
[45]	Tensile	ASTM T8			0.0044
[73]	Compression	ASTM 695-02	Until Failure	1	
[60]	Compression				0.001
[59]	Compression	ASTM E9		0.5	
[68]	Flexural	ASTM F2921		2.54	
[66]	Compression				0.0002
	Flexural	ASTM C1684-13	5 kN		0.0022
[80]	Compression			0.9	0.001
	Hopkinson bar				10 <sup>2</sup> – 10 <sup>4</sup>

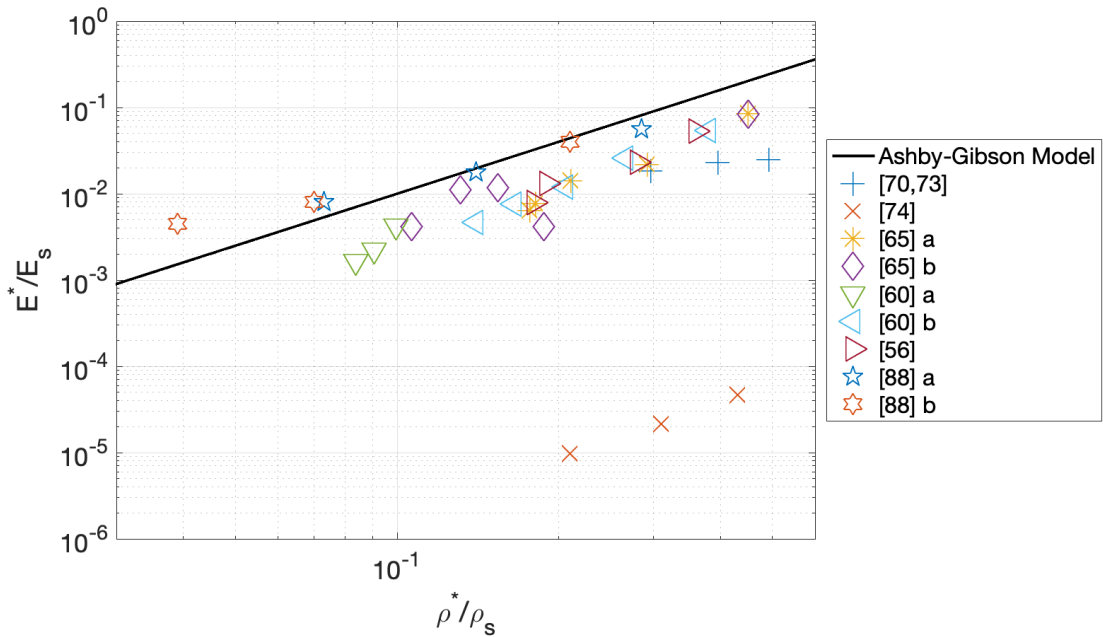


Figure 7: experimental results for relative Young modulus from literature

### 1.2.2 Effect of working temperature on the compression behaviour of the lattice structures

As far as the effect of the working temperature is concerned, Xiao et al. analysed the response of open-cell rhombic dodecahedron structure [78]. Their study also analysed the effects of the ratio between the length ( $l$ ) and the diameter ( $d$ ) of the struts. Two different configurations have been studied: in the first one, the previous mentioned  $l/d$  ratio is equal to 2.5, whereas in the second one  $l/d$  is equal to 1.5. The specimens have been produced with an Arcam A2 system and then were tested with the same quasi-static compressive conditions at room temperature, 200°C, 400°C and 600°C, respectively. A high-temperature furnace was used to regulate thermal conditions.

Figure 8 shows the room temperature nominal stress-strain curves of lattice structures under uniaxial compression, also detected in other studies in the literature [60,80,81]. The curves can be divided into three main segments. The first part is the elastic behaviour of the lattice structure, the second one represents the progressive collapse of the layers up to when the structure has the same behaviour of the bulk material that is visible in the last part of the graph. The failure of the specimens occurred at 45° by brittle fracture, as also Cheng et al. observed in a previous study [60].

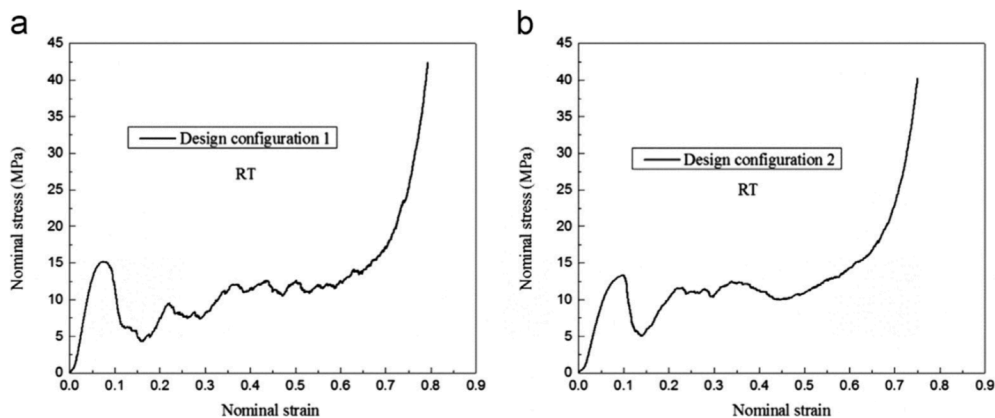


Figure 8: Nominal stress-strain curves for configuration 1 with an  $l/d$  ratio of 2.5 (a) and configuration 2 with an  $l/d$  ratio of 1.5 (b) [78].

The same compression test was also conducted at different temperatures, and the resulted stress-strain curves are shown in Figure 9. The increase in the temperature causes the curves to become smoother, and the plateau stress decreases. This result can be explained because the material shows a thermosoftening behaviour and a change of failure mode. As said, at room temperature lattice structure shows a brittle behaviour with failures at 45°. With the increment of the temperature, the specimens did not show a clear fracture angle, random

failure surfaces were indeed detected. As far as the effect of the size is concerned, the performances of the structure with the larger cell size (configuration 1) are worse than the ones with the smaller cell size (configuration 2) for both elastic modulus and collapse strength. According to the Ashby-Gibson theory, this behaviour is explained by the lower relative density of the structure with larger cell size.

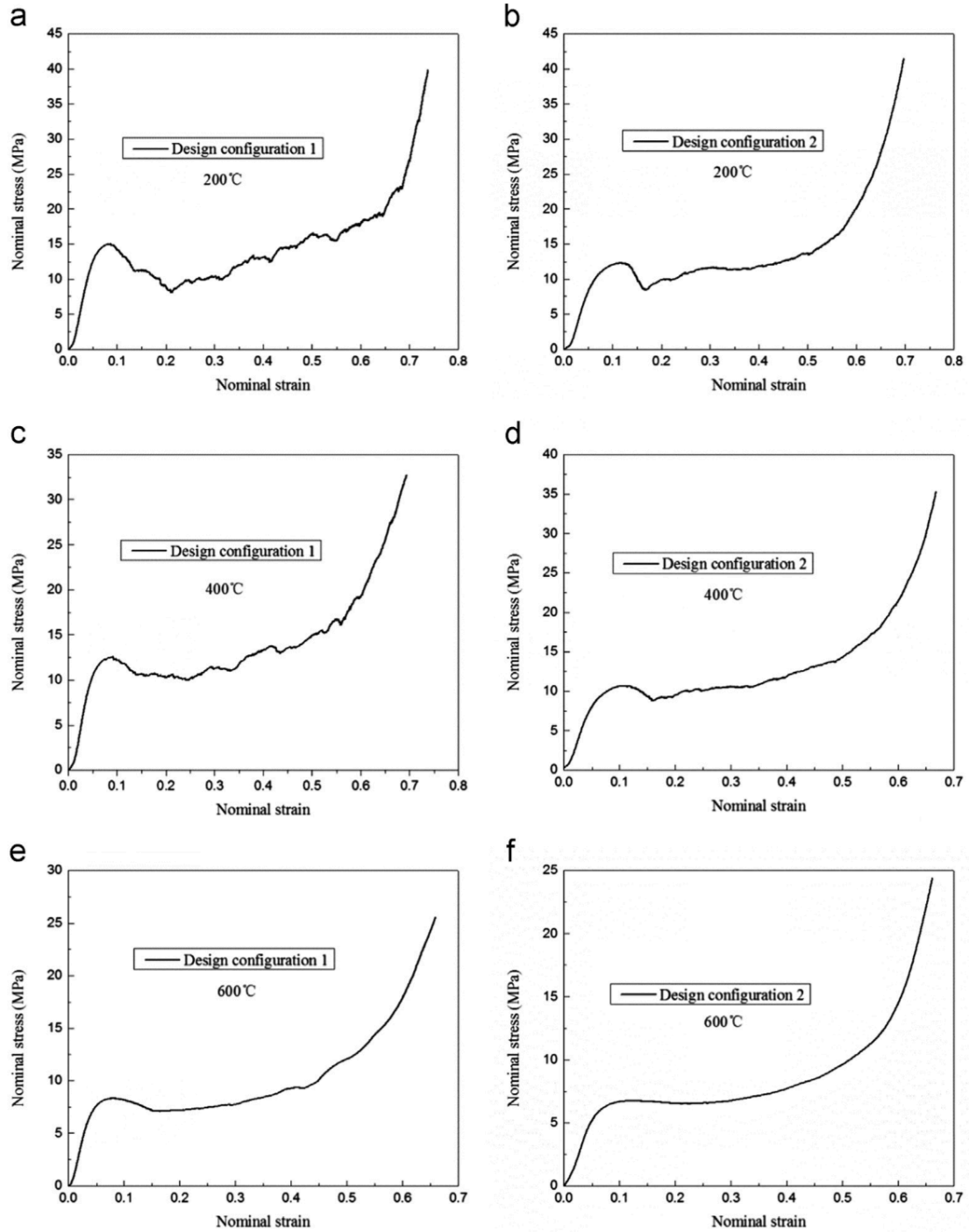


Figure 9: Nominal stress-strain curves at different temperature for configuration 1 (a,c,e) and configuration 2 (b,d,f) [78].

### 1.2.3 Hardness

The hardness characterization of titanium made lattice structure has been rarely investigated in the literature. Cheng et al. [60] investigated the hardness of lattice and foam ligaments (or struts). Hardness tests were conducted on both foam and lattice specimens with different strut size. As it is possible to see from *Table 2*, an increase in Vickers hardness occurs with the decrease of the strut size. Optical observation showed for foams a finer microstructure with respect to the lattice structures, as it is possible to see from Figure 10. This result suggests that foams exhibit fast cooling with respect to the lattice structure. The cooling rate increases with the decrease of ligament/strut thickness, thus it was possible to conclude that with a decrease of the thickness of the ligament/strut, a finer microstructure forms that consequently increases the cell hardness.

Table 2: Hardness Vickers of the cell for specimens tested by Cheng et al. [60].

Samples	Ligament (strut) length [mm]	Ligament (strut) thickness [mm]	Cell Hardness, HV [GPa]
Foam 1#	~ 4.19	~ 1.04	3.23 ± 0.25
Foam 2#	~ 3.68	~ 0.99	3.30 ± 0.10
Foam 3#	~ 3.15	~ 0.84	3.36 ± 0.19
Lattice 1#	~ 3.13	~ 1.08	3.03 ± 0.22
Lattice 2#	~ 2.54	~ 0.94	3.15 ± 0.09
Lattice 3#	~ 2.07	~ 0.86	3.24 ± 0.16
Lattice 4#	~ 1.69	~ 0.77	3.31 ± 0.14
Lattice 5#	~ 1.24	~ 0.72	3.51 ± 0.16

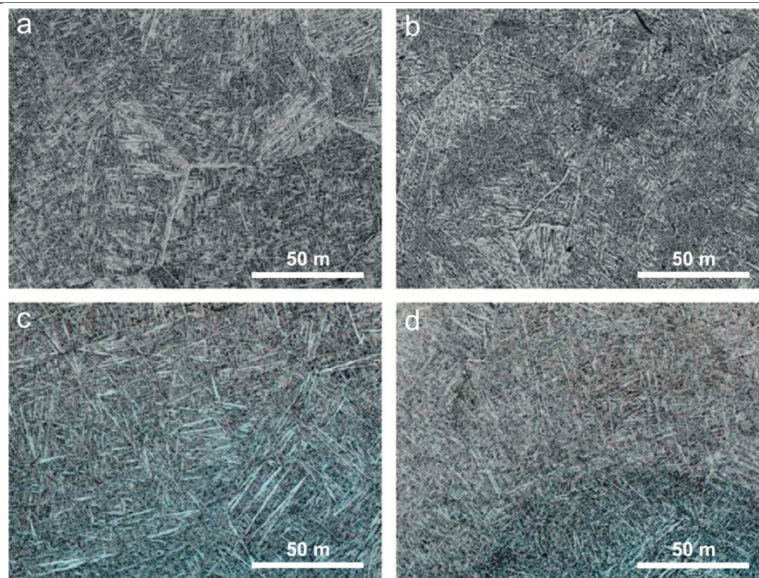


Figure 10: Optical microstructure of the foams (a,b) and the lattice structures (c,d) from [60].

#### ***1.2.4 The behaviour of the lattice structure under cyclic loads: fatigue investigations***

The influence of loading frequency between 2 Hz and 30 Hz on implant failure under cyclic fatigue conditions has been investigated by Karl and Kelly studies [82]. The experimental results showed that fatigue failures occurred more likely at low loading frequencies. On the other hand, no particular effect was found regarding the loading magnitude. After the conduction of Weibull and SEM analyses, it was possible to understand that damage accumulation is the main failure mechanism for fatigue behaviour of lattice structures.

Li et al. investigated the compression fatigue behaviour at different load levels of rhombic dodecahedron unit cells lattice structures with a range of relative density between 0.73 g/cm<sup>3</sup> and 1.68 g/cm<sup>3</sup> [81]. Figure 11 shows that for a low load level the vertical asymptote, which matches with the unstable crack propagation, was set at a higher number of cycles. With the increase of load conditions, the fatigue limit was found to be lower. Comparing the results of the different density specimens, the fatigue strength was higher for higher density structures. A like-Ashby-Gibson relationship was found between relative fatigue strength and relative density [61]. The fatigue mechanism observed from the experimental results seemed to be a combination of cyclic ratcheting and fatigue crack propagation.

Xiao et al. studied the mechanical properties of open-cell rhombic dodecahedron structure at different loading rates for dynamic loading [80]. Different sizes of both unit cell and strut were also investigated. The results showed that for low values of loading rate, the stress-strain curves respect the three-stage trends. These results were comparable to previous studies meaning that the low strain rate may be considered static [60,78,81]. When the loading rate increased the typical trend of the lattice behaviour disappeared since the bulk elastic behaviour was not detected (the last part of the typical trend). The failure mode for all the structures was the same also shown by previous studies with failure bands at 45° [60,78]. In addition to experimental test, an FE model was also developed considering the actual surface quality of the struts based on X-ray tomography. The numerical results matched well with the results from mechanical tests.

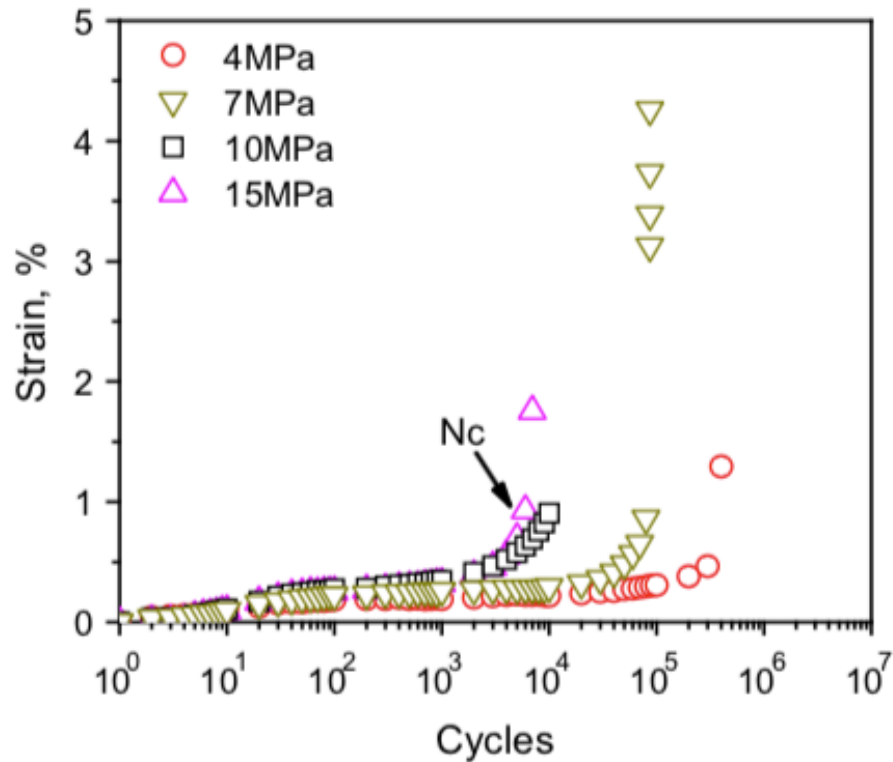


Figure 11: a strain-cycles diagram showing the trends of strain accumulation for different load conditions [81].

### 1.3 Effect of the precision of the EBM process and the surface roughness on the mechanical properties

The accuracy of the EBM process is mainly affected by heat transfer [37]. Due to the high working temperature, the shrinkage of the material and the unmelted powder that could be found attached to the part can cause an error of size and dimensions. Especially, for the smaller details and features, as in the case of the lattice structures, this deviation affects the final performance of the structure.

According to the study presented by van Grunsven et al. [74], the bigger deviation has been found for the smaller strut thickness when the nominal geometry (CAD model) was compared with the actual lattice produced parts by the EBM Arcam S12. This difference occurs because smaller strut sizes have a characteristic dimension of about the size of the minimum melted volume, equal to the spot of the electron beam. Thus the replication of the CAD model with dimensions around 200-500  $\mu\text{m}$  becomes less accurate with respect to the bigger geometrical features.

Horn et al. evaluated the precision of the Arcam A2 system [68]. For several specimens, a theoretical relative density from the CAD model and then after the building phase were

evaluated. For each specimen was also evaluated the actual density from measured weight and volume. Respect to the calculated theoretical relative densities, the actual relative densities resulted to be dependent by the cell size. In particular, for the lower cell sizes the deviation between the theoretical and the actual values is bigger than the values for the bigger cell size. Especially, the actual relative densities for the smaller cells are not affected by the size change. This difference occurs due to the precision of the machine which is lower for the smaller strut sizes because the melt pool size is comparable with the strut size. For the Arcam A2 system, Horn et al. [68] suggested that the strut size limit is around 0.5 mm; this value is in accordance with the previous mentioned study by van Grunsven et al. [74].

Parthasarathy et al. evaluated the process precision for the building of the cubic lattice structures [70]. Four sets of specimens were fabricated on an Arcam S12 system with differences in the pore and strut size, with an overall designed porosity ranging from 60.91% to 75.83%. A low-pressure pycnometer was used to evaluate the relative density and a CT-scan with an image reconstruction software to reconstruct the 3D model of the fabricated parts for evaluating the actual strut and pore sizes. For the fourth set of specimens with minimum strut size of 0.450 mm the porosity error between the CAD model and the fabricated model was maximum, more or less in the amount of 22%, and the EBM process was more accurate with the increasing of the strut size. This result occurs for the same reasons previously explained by [74] and [68].

Sun et al. studied the effect of surface roughness on the mechanical properties of Ti-6Al-4V specimens [83]. Both chemical etching and machining were used to improve the surface corrugation height. The results of tensile tests were compared with the results of the as-built condition specimens. To investigate surface morphology, a field emission scanning electron microscope (FESEM) and an Alicona infinite focus microscope were used. Figure 12 depicts the different surface morphologies with both the cited methods. The surface roughness of lattice structure was reduced with both chemical etching and machining. The  $R_a$  and  $R_z$  were respectively 38.9  $\mu\text{m}$  and 209.5  $\mu\text{m}$  for the as-built structure. The values for the chemical etching and the machining were 10.9  $\mu\text{m}$  and 58.19  $\mu\text{m}$  and 0.13  $\mu\text{m}$  and 0.95  $\mu\text{m}$ , respectively. As far as the tensile test is concerned, the as-built specimens showed the lowest value for both yield stress and ultimate tensile strength while the etched and machined specimens resulted similar. The results can be explained considering that the as-built condition presents the highest values of surface roughness. Thus, since the external corrugations cause stress concentrations, the as-built specimens reached fracture faster. On the other hand, since the difference between etching and machining is not so evident through

the tensile tests, chemical etching can be considered as a good technique to enhance the properties of lattice structures.

Suard et al. studied the structural characterization and the geometrical imperfection derived from the construction on the EBM system of the octet-truss lattice structure at the scale of a single strut [84]. The roughness was measured using the images captured by X-ray tomography, and it resulted in having a period of about 50  $\mu\text{m}$ .

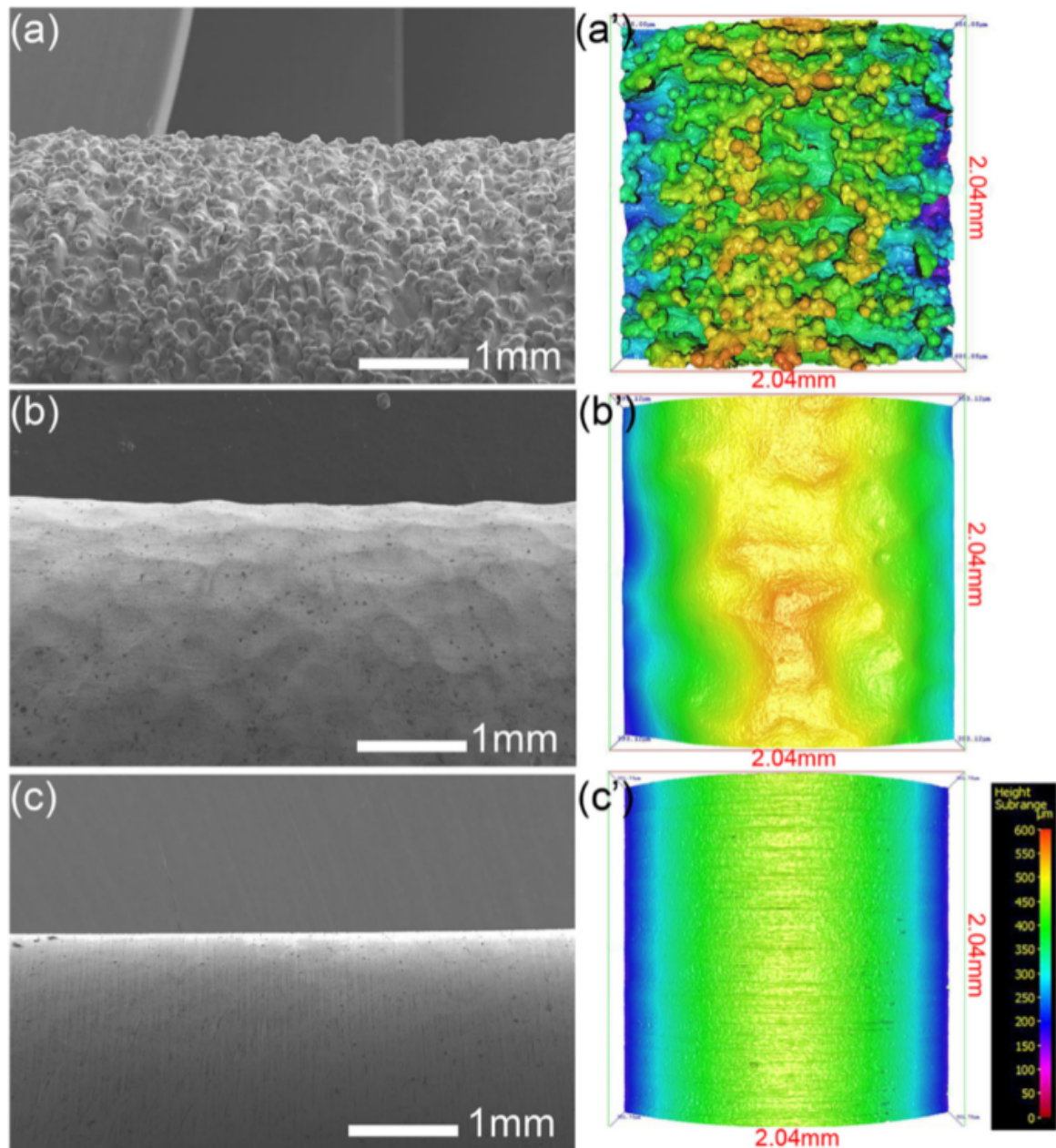


Figure 12: FESEM surface images of as-fabricated (a), surface-etched (b) and machined (c) specimens; surface conditions of as-fabricated (a'), surface-etched (b') and machined (c') specimens observed under Alicona IFM [83].

Figure 13 shows images of the octet-truss; *Fig. 13b* and *Fig. 13c* depict the reconstruction of a single strut based on the X-ray tomography images. The surface roughness is partly due to unmelted powder stuck to the melted zone. Suard et al. [84] defined an efficient volume ratio given by the relationship:

$$\varphi = \frac{V_{inscribedcylinder}}{V_{strut}} \quad (4)$$

Here  $V_{inscribedcylinder}$  is the volume of the inscribed cylinder inside the strut and  $V_{strut}$  is the volume of the strut itself. These two parameters were estimated from the 3D image analysis. The aim of the present study was to evaluate the dependency of this volume ratio upon strut orientation and strut diameter. The first result of the study was obtained after studying  $\varphi$  with respect to the CAD strut size: with the increase of the theoretical cross-section of the struts, the volume ratio had an increase that was lower with respect to the increment of the theoretical cross-section of the struts. This is justified by the fact that an almost constant roughness value was detected for all the struts analysed. Investigating the effects of strut orientation, it was possible to see smaller volume ratios for struts build parallel to the building platform and higher volume ratios for struts build perpendicular to the building platform [84].

Suard et al. compared the nominal CAD structures and the produced ones [52]. They showed that the produced struts were always thinner than the nominal ones. Consequently, the manufactured relative density was lower than the designed one. Additionally, the final dimension of the strut is also affected by the orientation on the dimension of the structure.

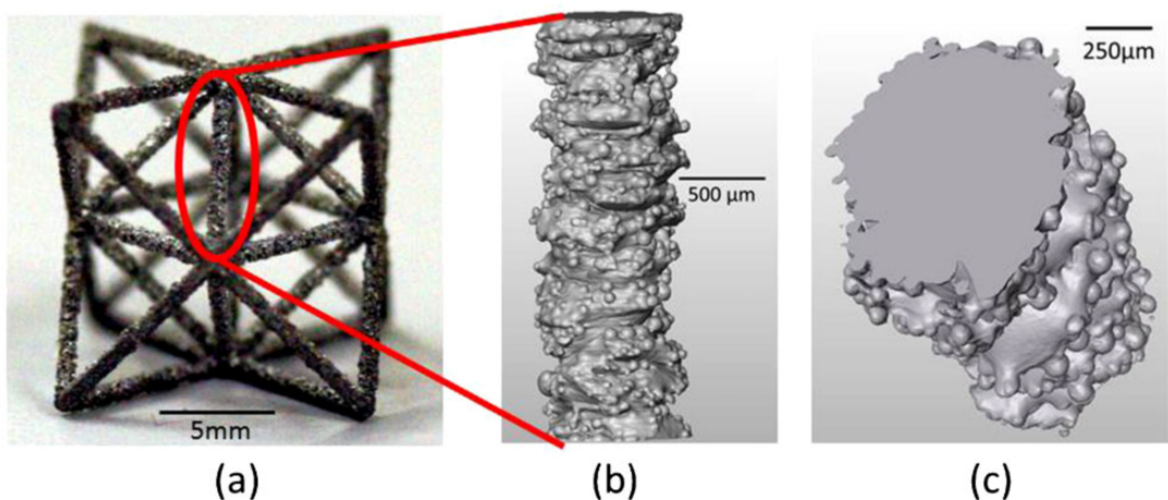


Figure 13: images showing a global octet-truss unit cell (a), a 3D reconstruction of one strut (b) and an isometric view of a 1 mm strut (c) [84].

Figure 14 shows the aspect ratio for struts build at  $0^\circ$ ,  $45^\circ$  and  $90^\circ$  with respect to the building platform. For struts build vertically, the shape of the section was nearly circular, instead,

moving towards the horizontal strut, its actual section cannot be considered circular. This phenomenon was explained by considering the heat transfer during the construction phase on the EBM system. Since the powder has a lower thermal conductivity with respect to the melted area, for the struts build at  $0^\circ$  a heat accumulation resulted in an over-melted zone that increases the aspect ratio [52]. To consider this deviation and predict the mechanical behaviour of a lattice structure, the mechanical equivalent diameter of single struts has been introduced [52]. The equivalent diameter  $D_{EQ}^{NUM}$  is intended as the diameter that produces the elastic behaviour of a build strut calculated by a Fast Fourier Transform calculation. A geometrical equivalent cylinder diameter  $D_{EQ}^{GEOM}$  was also defined as the diameter of the inscribed cylinder into the strut.

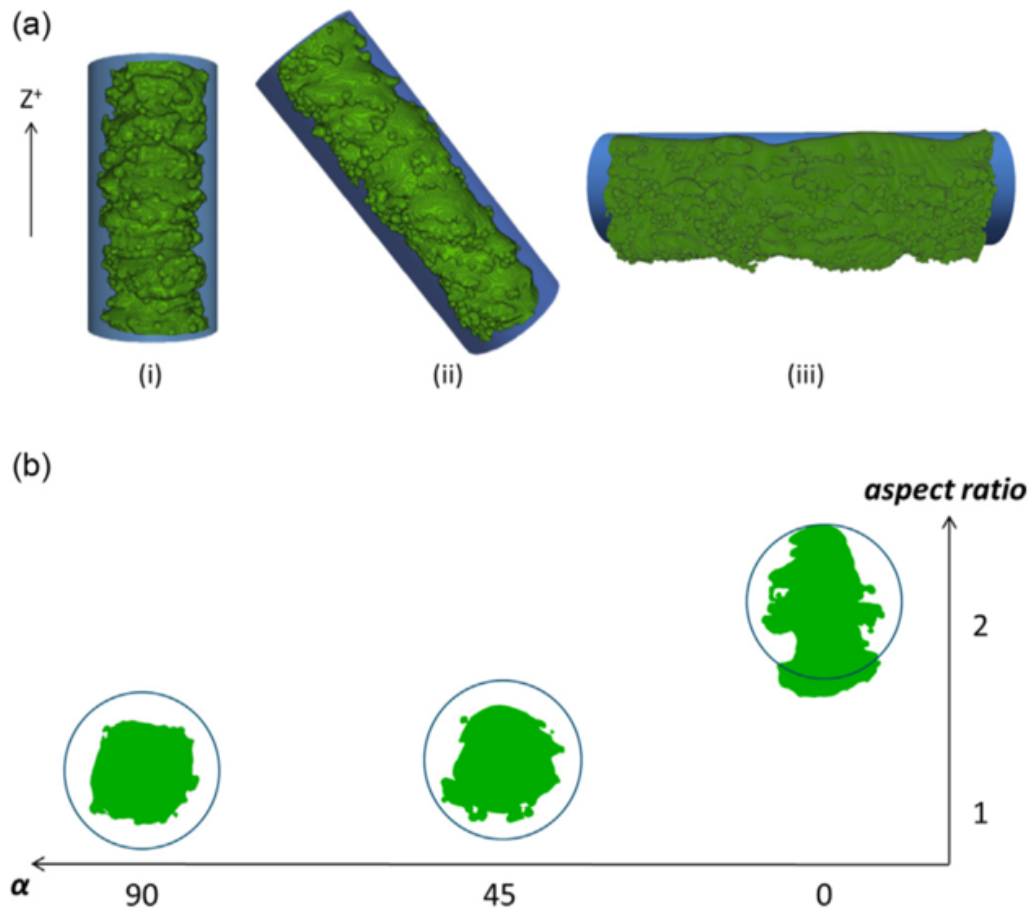


Figure 14: (a) comparisons between the CAD design (in blue) and the build struts (in green) at different construction angles; (b) aspect ratio with respect to construction angle [52].

Table 3 resumes the results of the present study; it is possible to see that equivalent diameter is averagely significantly thinner than the nominal diameter  $D^{CAD}$ ; in addition,  $D_{EQ}^{GEOM}$  is thinner than  $D_{EQ}^{NUM}$ . An FE simulation based on these data was conducted to evaluate the relative stiffness of octet-truss type lattice structures with each diameter shown in Table 3. To

obtain the range of relative density, the unit cell size was adapted with a fixed strut size for each case. These results were compared with experimental results from uniaxial compressive tests conducted on the build specimens.

Table 3: values of CAD, numerical and geometrical equivalent diameters with respect to strut's construction angle [52].

	$\alpha$		
	90°	45°	0°
$D^{CAD}$ [mm]	1	1	1
$D_{EQ}^{NUM}$ [mm]	0.576	0.581	0.706
$D_{EQ}^{GEOM}$ [mm]	0.456	0.414	0.518

Figure 15 collects the trends of FEM and experimental results. FEM simulations with the nominal diameter of the struts of 1 mm overestimated the experimental trend. FEM simulations conducted with both equivalent diameters underestimated experimental results, but the curve calculated with the numerical approach was similar to the experimental data.

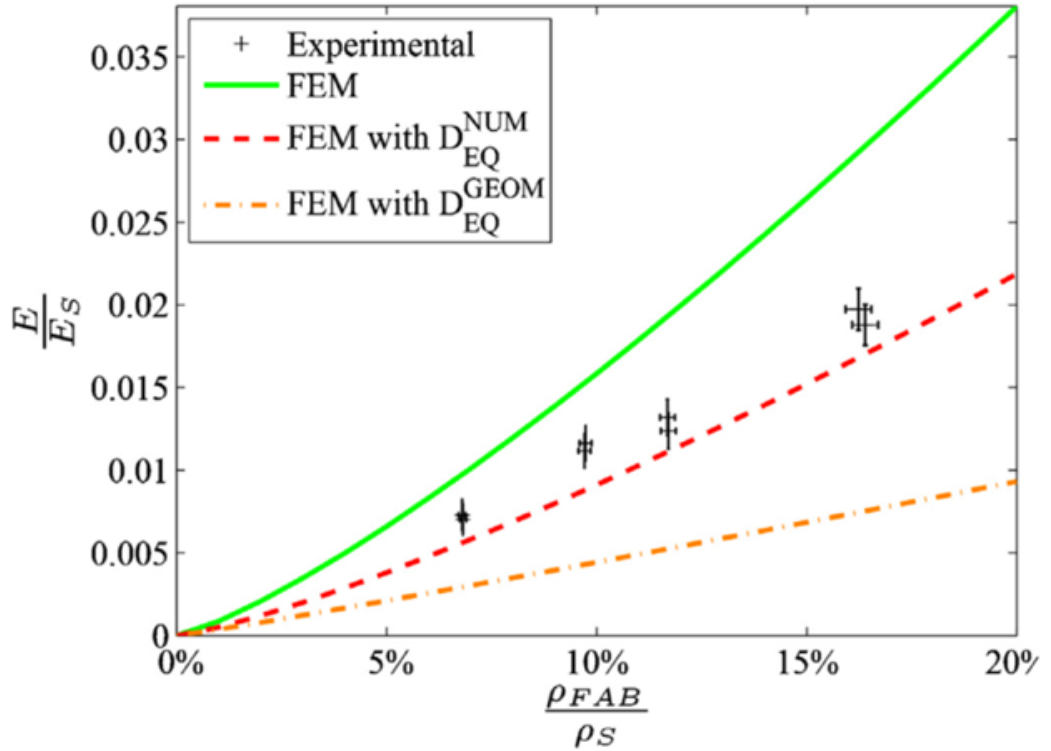


Figure 15: Relative elastic modulus with respect to relative density for different strut sizes: green curve for DCAD, the red dashed curve for DEQNUM, the orange curve for DEQGEOM. Experimental results are depicted in black [52].

Yang [79] developed an experimental-assisted design for octahedral lattice structures in which the unit cell was modelled analytically and analysed through FE analysis. For the

validation, the structure was produced by an Arcam S400 system. After the modelling phase, uniaxial compression was simulated by FE analysis to detect the effects of both the number of layers in the z-direction and the number of unit cells in the XY plane. The modelling successfully represented the Young modulus prediction for the octahedral lattice structures. Additionally, the chosen cell exhibited a good predictable size effect. The elastic modulus increases with the increase of both the number of layers and the unit cells in the XY plane. This result is in good accordance with the previously analysed study by Horn et al. [68].

Differently from the previous analysed studies which focus on just the cellular specimens made by EBM, Chang et al. [85] investigated the differences between two different AM metal techniques. They indeed studied the specific effect of surface roughness on fatigue properties of dental implants made with both L-PBF and EBM parts made of Ti-6Al-4V ELI. The surface of as-built EBM specimens was rougher than the surface of as-built SLM. Consequently, in fatigue behaviour it was possible to see that L-PBF made specimens exhibit higher values of fatigue life with respect to the other conditions analysed. The EBM made specimens had instead the worst values of fatigue life, even lower than the cast samples. This result occurred because in fatigue behaviour the roughness of the surface plays an important role in fatigue life. Since  $R_a$  increases moving from L-PBF, cast and EBM cases, it was possible to conclude that fatigue life of Ti-6Al-4V ELI decreases with the increasing of the surface roughness.

Focusing only on one AM technique, Epasto et al. [77] studied the roughness effect on Ti-6Al-4V bulk specimens made by EBM. In order to investigate this particular effect, some of the fabricated specimens were machined. The average surface roughness was equal to 21.939  $\mu\text{m}$  and 0.782  $\mu\text{m}$  for respectively the as-built and machined specimens. After the conduction of tensile tests, the stress-strain trends were computed, and the results are showed in the table below.

As it is possible to see from Table 4, the main difference is the higher value of the elongation at failure for machined samples. This result occurs because the surface roughness of the machined sample, as mentioned earlier, has a lower value with respect to the as-built specimen.

Table 4: results of tensile tests for both as-built and machined conditions from the study by Epasto et al. [77].

Specimen	Yield stress [MPa]	Tensile strength [MPa]	Young modulus [GPa]	Elongation at failure [%]
As-built	885	895	118	5.4
Machined	873	965	108	17.5

## **1.4 Effects of thermal treatments on the mechanical behaviour of Ti-6Al-4V alloy made by EBM**

Heat treatments on EBM made parts are mainly conducted to reduce internal porosity and avoid the presence of defects. Since the porosity could appear due to the presence of porosity inside the powder itself, Cunningham et al. [48] measured the powder porosity to correlated the subsequent results on the treated parts. Two batches of powder have been analysed. Both powder batches have shown a certain quantity of porosity that has been maintained after the EBM process into the as-built specimens. To reduce the internal porosity, a HIP treatment was performed for 2 hours, at 900°C in an Argon pressure of 103 MPa, according to ASTM F2924 [86]. After the HIP treatment, the porosity was erased from one type of powder. Instead, there was a little number of pores in the other type. A solutionizing treatment was then carried out to evaluate the pore regrowth. The solutionized sample with a residual porosity after the HIP treatment showed a significant pore regrowth, while no porosity was detected in the other sample.

Tammas-Williams et al. studied the effectiveness of HIP on EBM samples produce by an Arcam S12 system [49]. The samples were HIPed for 2 hours at 920°C with a pressure of 100 MPa of Argon and a cooling rate of 6°C/min.

Figure 16 shows the comparisons between treated and untreated samples. After the HIP treatment (Fig.16b), all the porosities were removed from samples labelled C1 and MC, while for the sample labelled T3 tunnel defects connected to the surface were still visible. In general, HIP treatment confirmed led to a porosity reduction of about 60%. The following work of the same authors evaluated the porosity regrowth during subsequent treatments [46]. The specimens were HIPed in the same conditions of the previous study [56], and then three different annealing conditions were tested. In the first condition (HT1) a total time of 10 minutes at 1035°C under vacuum have been assumed. On the other hand, in the second condition (HT2) a total time of 10 hours at the same temperature and pressure conditions of the previous treatment has been fixed to evaluate the pores regrowth. Lastly, in the third condition (HT3) a total time of 10 minutes in vacuum conditions at 1200°C has been set to evaluate the temperature effect on pore regrowth.

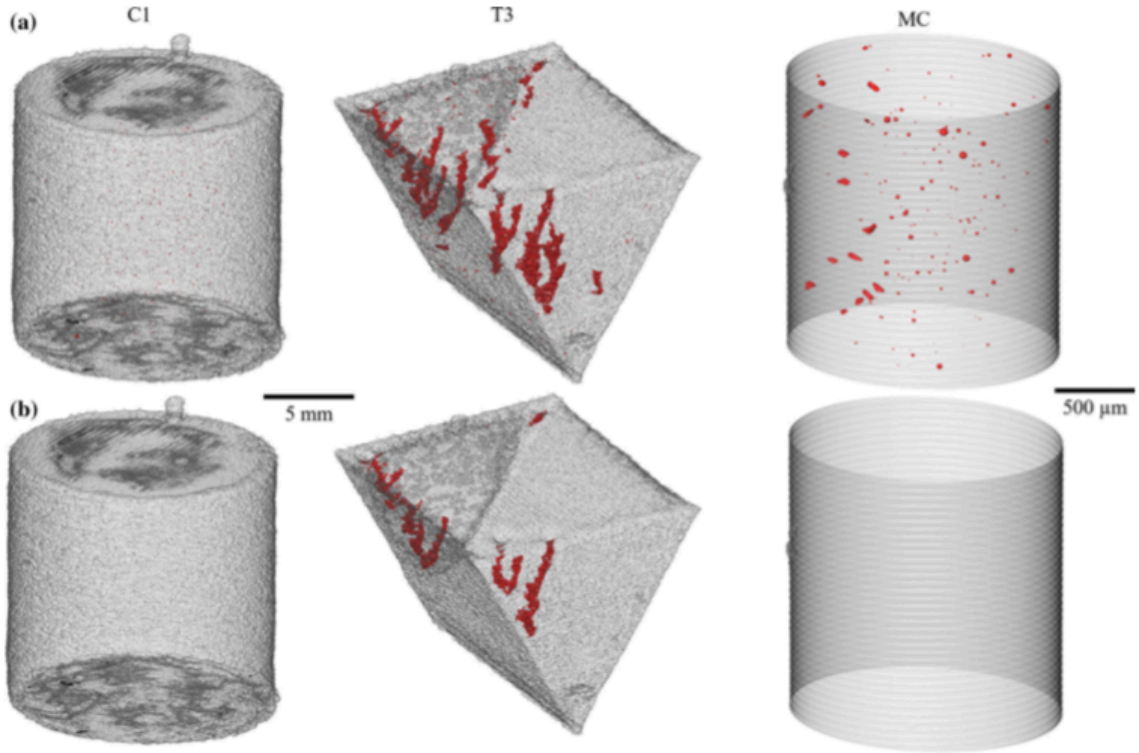


Figure 16: CT scan images showing porosity in red; (a) as-built condition, (b) after HIP conditions [49].

Table 5 shows the results of the CT scan analysis. After the HIP treatment, no porosity has been detected at the scanner resolution of  $5.2\mu\text{m}$ . After the HT1, a certain number of pore with a certain mean equivalent diameter has been detected. The number of pores increases after the HT2 and HT3. However, the volume fraction of pores was always lower than the one in the as-built conditions. Comparing HT2 and HT3 results, it is possible to understand that the temperature effect is much more significant on pore regrowth than the time effect.

Table 5: statistical data from the same sample in the five different conditions analysed [46].

Condition	Volume fraction [%]	Number of pores	Mean Equiv. Dia. [ $\mu\text{m}$ ]	Max. Equiv. Dia. [ $\mu\text{m}$ ]
As-built	0.0397	309	13.3	53.3
HIPed	0.0000	0	-	-
HT1	0.0007	49	8.4	18.6
HT2	0.0011	63	9.2	20.0
HT3	0.0026	140	9.4	21.6

The effects of heat treatments on the mechanical response of Ti-6Al-4V parts made by EBM have been investigated also by de Formanoir et al. [87]. In their study two kinds of heat treatments were evaluated: the first set of them was conducted under the  $\beta$ -transus

temperature, at 950°C for 60 minutes, while the second one was conducted over the characteristic temperature, at 1040°C for 30 minutes. In addition, in each set of the cited heat treatments, the cooling rate was changed between AC (air cooling) and FC (furnace cooling), in order to understand the effects inducted by the cooling thermal gradient. The results showed that the microstructure of the heat-treated samples under  $\beta$ -transus did not change enormously, resulting just in a slightly coarsening. On the other hand, the over  $\beta$ -transus heat treatments changed completely the microstructure. This occurred because the diffusion at temperatures above  $\beta$ -transus permitted a completely renewing of the microstructure, which stabilized in a much coarse way with also a different orientation of the  $\alpha$  and  $\beta$  phases.

As far as the effects of heat treatments on the mechanical behaviour of Ti-6Al-4V lattice structures made by EBM is concerned, only a few works have been found in the literature that addressed this topic. Epasto et al. studied the effect of thermal treatments on the compressive behaviour with the aim to investigate whenever there is an effect of residual stresses on EBM components [77]. Thus, stress relief was performed on some specimens which were heated up to 300°C; this temperature was maintained for 3 hours, and then the specimens were cooled in the furnace. At this point, compression tests were conducted, and, after the evaluation of the stress-strain trends, it was possible to see that the heat-treated samples showed values of UCS and Young modulus slightly lower. Thus, it was concluded that the possible presence of residual stresses does not significantly affect the compressive behaviour of the lattice structure. The effect of defects on the mechanical response of Ti-6Al-4V cubic lattice structure produced by EBM was analysed by Hernandez-Nava et al. studied [45]. Compression and hardness tests were carried out. Two annealing treatments were run at a lower than  $\beta$ -transus (960°C) and a higher than  $\beta$ -transus (1200°C), respectively. Both of them were conducted for a total time of 120 minutes, and air pressure of 0.1 MPa. For the as-built condition, the microstructure of the struts perpendicular to the start plate showed a combination of  $\alpha$  and  $\beta$  phases, according to previous studies on the bulk material [30,44,65]. *Figure 17* shows the differences between three different points. Diffusionless  $\alpha'$  martensite for regions closer to the construction plate was noticed. For the under  $\beta$ -transus annealing, no consistent differences were found with respect to the as-built microstructure. For the over  $\beta$ -transus annealing instead, a coarsening of the microstructure was detected. For that, the mechanical tests showed lower compressive yield stress by approximately 11 %.

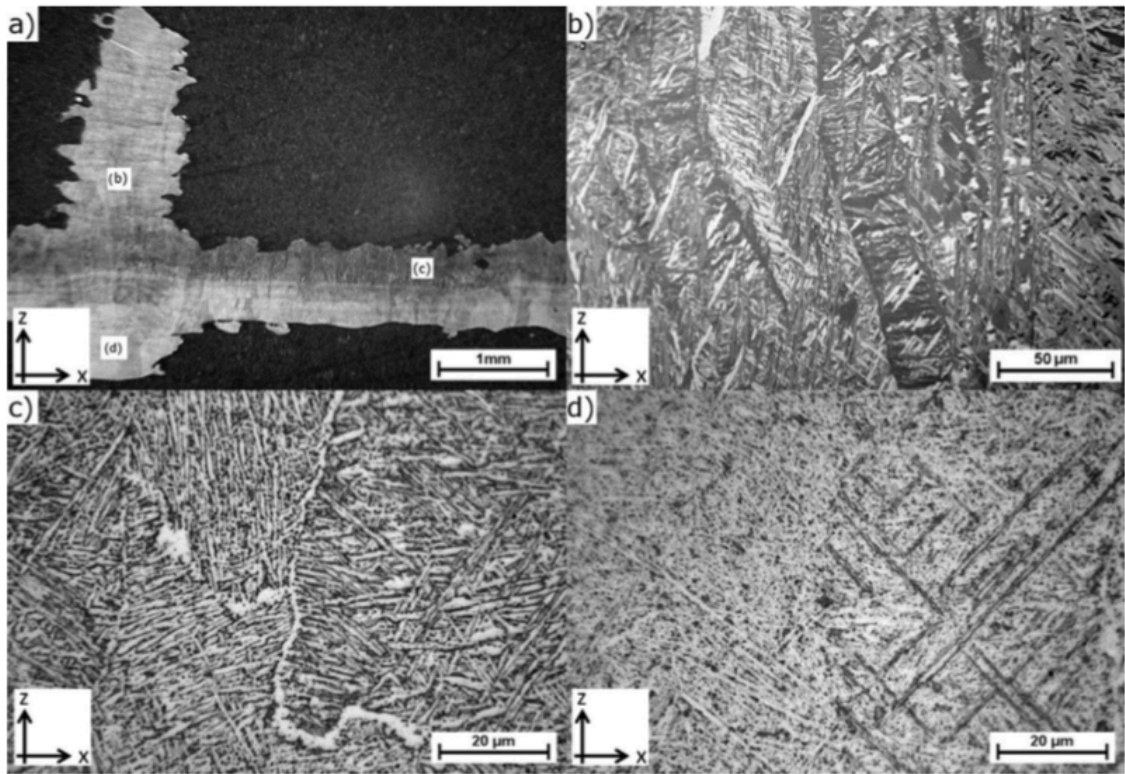


Figure 17: Optical micrograph of as-built condition (a) with three different locations of interest (b,c,d) [45].

In this last part of the present review, the effects of the heat treatments on the Ti-6Al-4V have been shown. Table 6 collects all the data regarding the parameters of the thermic cycles, showing also the target of each heat treatment.

Table 6: Heat treatments on Ti-6Al-4V made by EBM found in the literature. In the present table FC stands for "furnace cooling", AC stands for "air cooling" and WC stands for "water cooling".

Paper	Treatment	Target	Treatment parameters					Aging parameters				
			Heating ramp [°C/min]	Time [min]	Temperature [°C]	Pressure [MPa]	Atmosphere	Cooling ramp [°C/min]	Time [min]	Temperature [°C]	Cooling ramp [°C/min]	
[47]	HIP	Reduce internal defects	5	120	920	100	-	-	4.3	-	-	-
[44]	HIP	Reduce internal defects	-	120	920	100	Argon	6	-	-	-	-
[45]	Annealing	Reduce internal defects	10	120	960	0.1	Air	FC	-	-	-	-
	Annealing	Reduce internal defects	10	120	1200	0.1	Air	FC	-	-	-	-
[87]	Annealing	Simulate HIP effects	-	60	950	0.1	Argon	AC	-	-	-	-
	Annealing	Simulate HIP effects	-	60	950	0.1	Argon	FC	-	-	-	-
[9]	Annealing	Investigate microstructural changes	-	30	1040	0.1	Argon	AC	-	-	-	-
	Annealing	Investigate microstructural changes	-	30	1040	0.1	Argon	FC	-	-	-	-
[48]	Solubilization	Investigate microstructural changes	-	30	1100	0.1	Air	WC	-	-	-	-
	Solubilization	Investigate microstructural changes	-	30	1100	0.1	Air	AC	-	-	-	-
[49]	Solubilization	Investigate microstructural changes	-	30	1100	0.1	Air	FC	-	-	-	-
	Solubilization	Investigate microstructural changes	-	60	925	0.1	Air	WC	240	450	450	AC
[77]	Solubilization	Investigate microstructural changes	-	60	925	0.1	Air	AC	240	450	450	AC
	Solubilization	Investigate microstructural changes due to aging parameters	-	60	950	0.1	Air	WC	180/240/300/360/420/480	500/550/600	500/550/600	AC
[46]	HIP	Reduce internal defects	-	120	900	103	Argon	FC	-	-	-	-
	Solubilization	Investigate microstructural changes	-	10	1050	0.1	Air	FC	-	-	-	-
[77]	HIP	Reduce internal defects	-	120	920	100	Argon	6	-	-	-	-
	HIP	Reduce internal defects	-	120	920	100	Argon	6	-	-	-	-
[46]	Solubilization, after HIP	Evaluate pore regrowth	5	10	1035	< 10 <sup>-6</sup>	Vacuum	FC	-	-	-	-
	Solubilization, after HIP	Evaluate time effect on pore regrowth	5	600	1035	< 10 <sup>-6</sup>	Vacuum	FC	-	-	-	-
[77]	Solubilization, after HIP	Evaluate temperature effect on pore regrowth	5	10	1200	< 10 <sup>-6</sup>	Vacuum	FC	-	-	-	-
	Stress relief	Stress reduction	-	180	300	0.1	Air	FC	-	-	-	-

## 1.5 Objective

The presented review highlighted that there is still a lot of work and research to be accomplished before lattice structure can become an effective structure to be used for structural applications such as automotive and aerospace. In fact, several aspects appear still needed to be investigated. Among the reviewed papers, the main conclusion appeared that the mechanical behaviour of lattice structures is influenced by the cell shape, which slightly affects the value of the constants  $C_1$  and  $C_5$ , and mainly by the relative density. Structures with the same relative density have indeed similar mechanical behaviour. Additionally, a deep lack of knowledge on the mechanical behaviour on the heat-treated lattice has been detected. However, today almost all the additive manufactured metal parts are heat-treated to reduce the residual porosity and tailor the microstructure. To date, therefore it is evident that no advanced application can be designed because of the lack of detailed analysis on the effect of the most common heat treatments on the lattice performance.

The aim of the present work is to investigate the mechanical behaviour of Ti-6Al-4V lattice structures manufactured by EBM. In order to fully understand the effects of the shape of the unit cell, samples have been designed using three different unit cell types. In addition, to study the effects of cell size, for each unit cell type samples have been designed also using three different unit cell sizes. Lastly, some of the samples have been heat-treated using two different thermal cycles. The effects on the mechanical behaviour of lattice structures will be discussed in the following paragraphs.

## 2 Design of the experiments

### 2.1 Lattice design

In this study the behaviour of three different unit cell types has been analysed: 1) structure I: Dode Thin (Fig.18a), 2) structure II: GStructure 3 (Fig.18b), 3) structure III: Rombi Dodecahedron (Fig.18c).

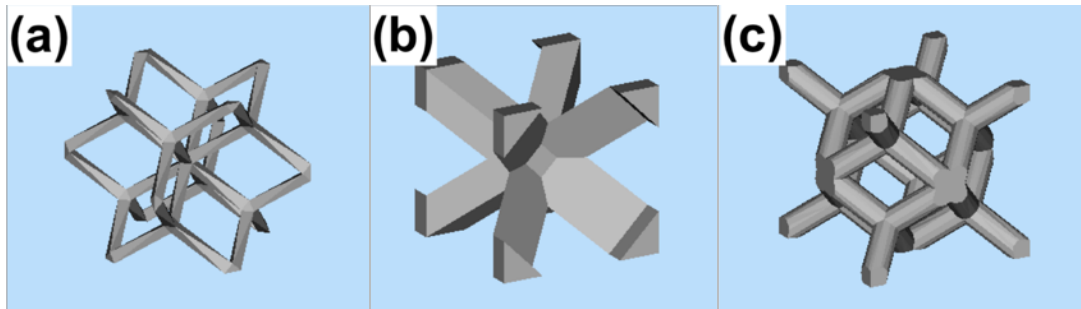


Figure 18: unit cells types analysed in the present study

The structures have been designed using Magics 21.11. The generical sample (Figure 19) has a cylindrical volume with a diameter and a height equal to 20 mm and 30 mm, respectively. The lattice structure is placed between two cylindrical caps 2 mm high that uniform the load distribution during the compression test. Therefore, total height of the lattice structure is 26 mm.

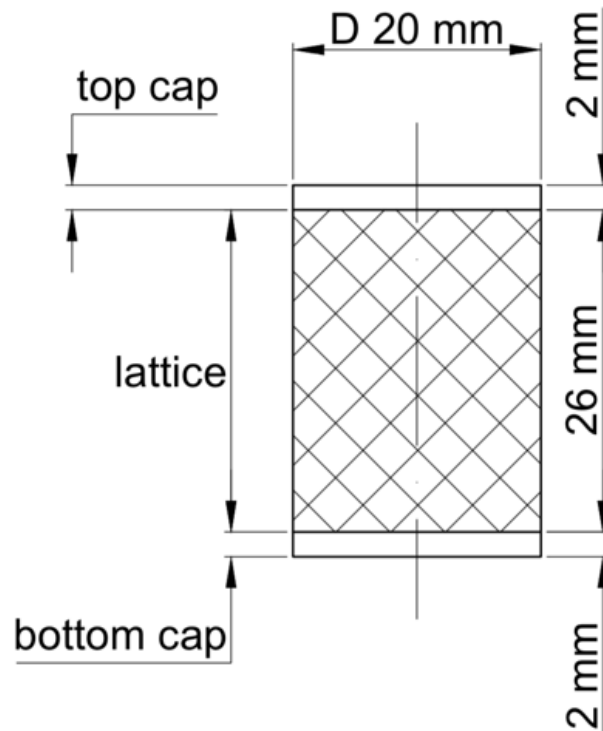


Figure 19: general design of each specimen

Each unit cell has been designed using three different sizes: 4 mm, 7 mm and 10 mm. Table 7 lists the geometrical properties of each structure.

Table 7: geometrical features of each structure type, all the values have been extract from the Magic file

Structure	Cell size [mm]	Strut size [mm]	Strut length [mm]
<b>I</b>	4	0.297	1.732
	7	0.519	2.601
	10	0.734	3.755
<b>II</b>	4	0.809	1.091
	7	1.432	1.884
	10	2.000	2.736
<b>III</b>	4	0.704	1.410
	7	1.382	2.467
	10	1.442	3.418

## 2.2 Production

In order to guarantee a robust experimental analysis, three replicas have been produced for each cell typology and size. In order to study also the behaviour of lattice structure after two different heat treatments, the build included 81 samples altogether. To refer to the as-built condition, untreated samples have been named “NTH”. On the other hand to refer to the two different heat-treated conditions, samples have been named “HT1” and “HT2”. Bulk specimens have been also designed to evaluate the actual density of the Ti-6Al-4V made by EBM process. The replicas were orientated so that the larger surface of the cups is parallel to start plate. All replicas have been produced unattached to the start plate and supported by a proper structure in order to avoid microstructure modifications. Additionally, they have been conveniently spaced along the building axis so as to have a uniform temperature distribution during the building phase. The build job was prepared using Magics 21.1. The samples were produced using an Arcam A2X system with standard Arcam Ti6Al4V powder with an average size of 75  $\mu\text{m}$ . The build job has been processed by an EBM build processor 5.0 with a Ti6Al4V

Standard Theme for the Arcam A2X system and a layer thickness of 50  $\mu\text{m}$ . After the production, the entire build has been cooled down inside the EBM chamber up to room temperature. All specimens have been cleaned by sandblasting process with compressed air at 4 bar and the Ti-6Al-4V powder. To verify that this last step had been done correctly and there was no powder stick between the struts, a Stereomicroscope was used to take pictures of the specimens. Figure 20 depicts the collected images.

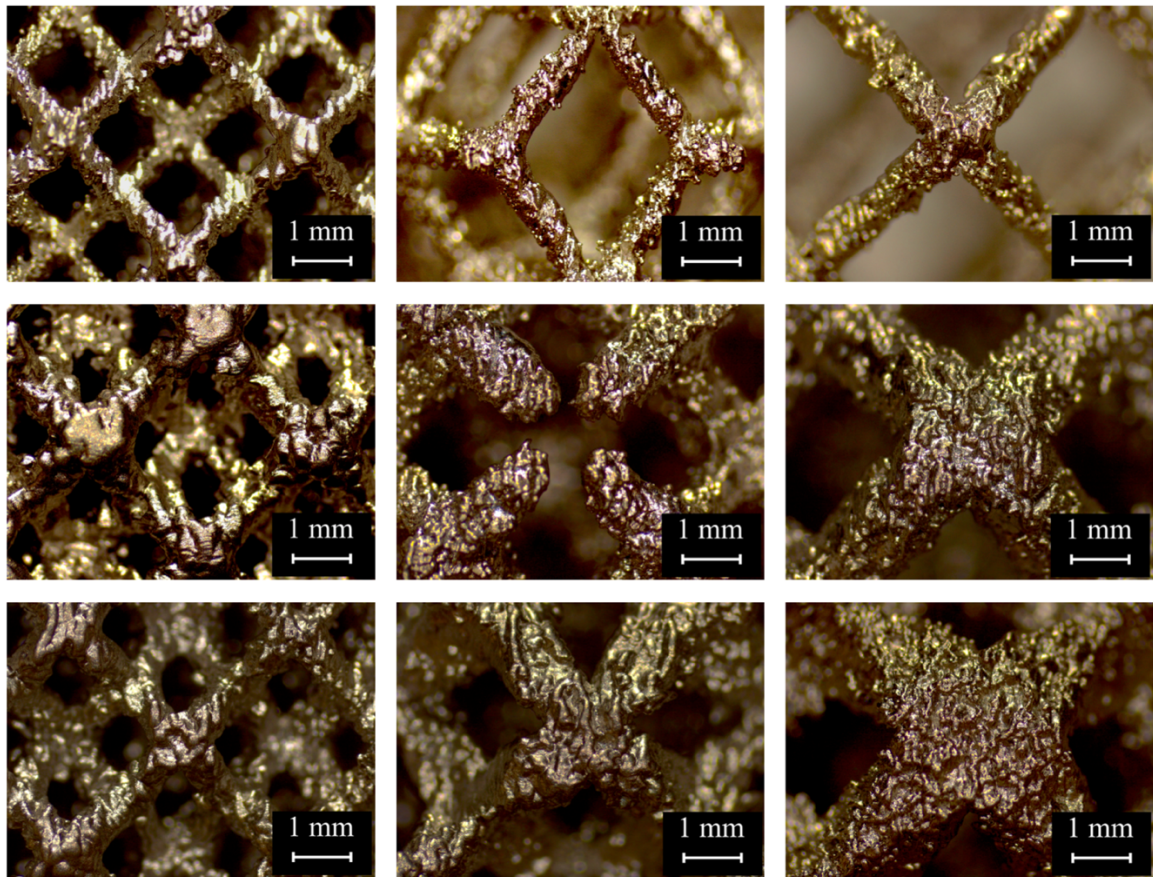


Figure 20: stereomicroscope images of each different specimen; the rows (from top to bottom) depict structures I, II and III, while the columns (from left to right) depict unit cell size of 4, 7 and 10 mm

### 2.3 Compression test

Axial compression tests have been carried out setting a strain velocity of 2 mm/min up to the full collapse of the structure. For specimens of the same unit cell type and unit cell size, similar loads/displacements trends have been observed. To evaluate the stress/strain curves, Equation 3 and Equation 4 have been used:

$$\sigma = \frac{P}{A_0} \quad (3)$$

$$\varepsilon = \frac{\delta}{l_0} \quad (4)$$

In the previous equations,  $P$  is the load and  $\delta$  is the displacement measured on the machine which carried out the compression tests;  $A_0$  is the area of the whole structure considered as the area of a circle of 20 mm diameter, while  $l_0$  is the height of the lattice part of each sample (26 mm). In the introduction of the present work it has been discussed that, as observed by Ashby and Gibson [61], cellular solids exhibit a compressive behaviour characterised by three main stages, as it is possible to see from Figure 21 which shows a simplified trend.

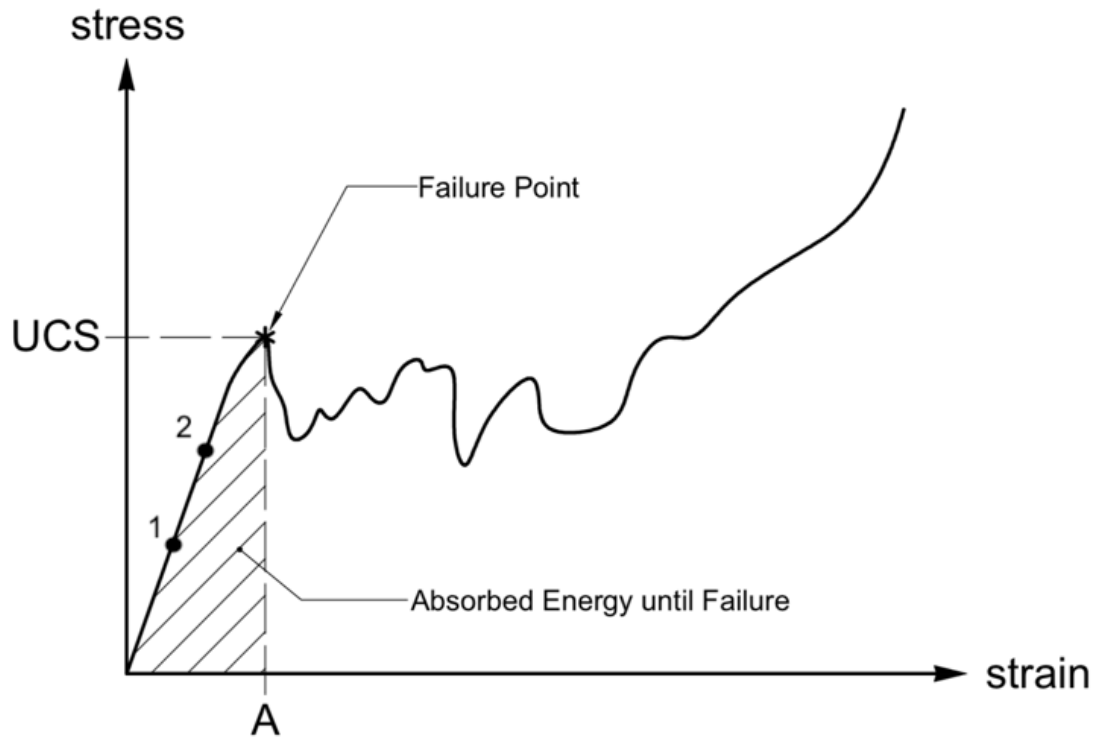


Figure 21: schematic curve obtained with the compression test

From the trend shown in Figure 21 it is possible to identify the failure point, which is the first maximum of the compressive curve. In this specific point, the stress reaches the  $UCS^*$  and the strain reaches the elongation at failure  $A^*$ . The area subtended by the trend up to the failure point represents the absorbed energy up to failure per volume unit. To compute the absorbed energy  $W^*$  it is possible to use Equation 5:

$$W^* = \int_0^{A^*} \sigma d\varepsilon \cdot V^* \quad (5)$$

In Equation 5 the second term is given by the multiplication of the cited absorbed energy up to failure per volume unit and the  $V^*$ , which in turn is evaluated dividing the mass of the structure (which will be discussed in the following paragraph) for the density of the Ti-6Al-4V alloy ( $4.42 \text{ g/cm}^3$ ). To evaluate the compressive Young modulus two points on the linear

trend, named 1 and 2 in Figure 21, have been selected. The values of  $E^*$  have been evaluated using Equation 6:

$$E^* = \frac{\sigma_2 - \sigma_1}{\varepsilon_2 - \varepsilon_1} \quad (6)$$

## 2.4 Heat treatments

In order to investigate the variations of the mechanical behaviour of heat-treated lattice structures, two different heat treatments have been designed. Figure 22 depicts the thermal-time diagram for the cited thermal cycles.

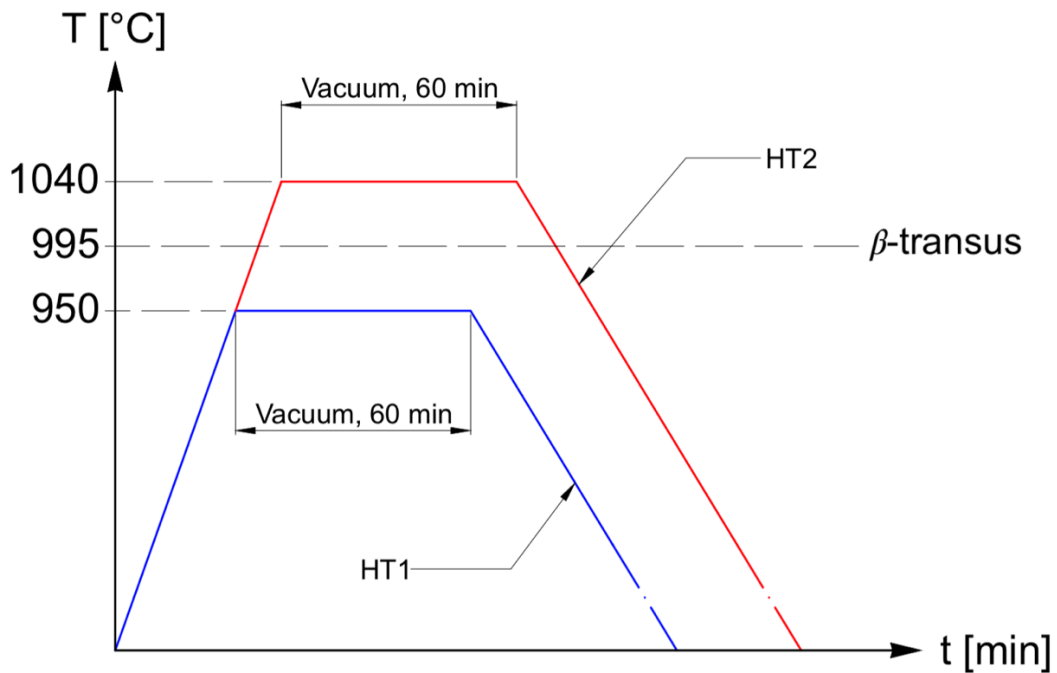


Figure 22: temperature-time diagram for the two designed heat treatments

As it is possible to notice, both heat treatments have been conducted for a total time of 60 minutes in vacuum. This specific condition has been selected in order to avoid oxidation at high temperatures. Both heat treatments have been performed with the same heating and cooling rates. The main difference between the two thermal cycles is the temperature at which they have been conducted. The first heat treatment, named HT1 and depicted in blue in Figure 22, has been performed at 950°C, temperature below  $\beta$ -transus (995°C [9]). The second heat treatment, named HT2 and depicted in red in Figure 22, has been performed at 1040°C, temperature above  $\beta$ -transus (995°C [9]). The two heat treatments have been so designed to investigate the treatment temperature effect on the mechanical properties and on the microstructure of lattice structure.

## 2.5 Characterization

To evaluate the actual average relative density of each sample, mass measures were conducted to evaluate the mass of the whole sample called  $m_{\text{meas}}$ . Later on the mass of the caps was evaluated by Equation 7:

$$m_{\text{caps}} = \rho_s \cdot 2 \cdot \pi \cdot h_{\text{cap}} \cdot \left(\frac{D}{2}\right)^2 \quad (7)$$

In this equation  $m_{\text{caps}}$  is the mass of both caps,  $\rho_s$  is the density of Ti-6Al-4V (4.420 g/cm<sup>3</sup>),  $h_{\text{cap}}$  is the height of a single cap (2 mm) and lastly  $D$  is the diameter of the specimen (20 mm). The mass of the caps is constant for all the different structure types and dimensions and is equal to 5.554 g. At this point, in order to evaluate the mass of the lattice part  $m_{\text{latt}}$ , the mass of the caps was subtracted to the measured mass. After the evaluation of this last parameter, it was possible to compute the volume of each lattice  $V^*$  which, as previously stated, is needed for the evaluation of the absorbed energy up to failure. Successively, to evaluate the density of each kind of sample the mass of the lattice part was divided by its theoretical volume, evaluated as the volume of a cylinder of 20 mm diameter and a height of 26 mm. In conclusion, the relative density  $\rho^*/\rho_s$  was evaluated dividing this last calculated parameter by the density of Ti-6Al-4V bulk material. Table 8 depicts all the data discussed in the current paragraph.

Table 8: values of averages of measured mass, lattice mass and relative densities for each cell type and size

Structure	I			II			III		
	4	7	10	4	7	10	4	7	10
Cell size [mm]	4	7	10	4	7	10	4	7	10
$m_{\text{meas}}$ [g]	11.387	8.693	7.573	17.571	13.067	12.361	15.852	15.251	14.441
$m_{\text{latt}}$ [g]	5.832	3.139	2.018	12.016	7.512	6.806	10.298	9.697	8.887
$\rho^*/\rho_s$ [%]	16.155	8.695	5.591	33.283	20.808	18.852	28.523	26.859	24.615
$V^*$ [mm <sup>3</sup> ]	1319.532	710.180	456.661	2718.602	1699.622	1539.869	2329.839	2193.841	2010.583

As far as the microstructure observation is concerned, the samples were firstly cut, then mount, ground and finally polished and etched using Kroll's reagent (2%HF, 4% HNO<sub>3</sub> in water). Images were taken using the Leica optical microscope for the cross-section of powders and Phenom table-top Scanning Electron Microscope (SEM) for the microstructure of printed samples and morphology of powder.

### 3 Results and discussion

#### 3.1 Mechanical behaviour of as-built lattice structures

##### 3.1.1 Compressive trends

As previously discussed, the compressive curves for lattice structures are characterized by three main stages: 1) elastic behaviour of the lattice structure, 2) progressive collapse of the layers until the structure has 3) the same behaviour of the bulk material.

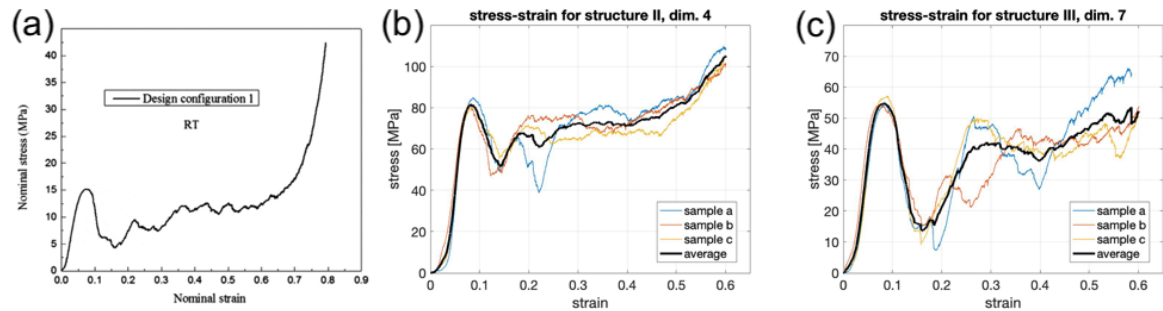


Figure 23: trends observed in the literature by Xiao et al. [78] (a), for structure II with unit cell of 4 mm (b) and for structure III with unit cell of 7 mm (c)

Figure 23 shows three different cases; the first one (Fig.23a) represents one of the trend evaluated by Xiao et al. [78]. The last two trends are the experimental results of structure II with unit cell size of 4 mm (Fig.23b) and of structure III with unit cell size of 7 mm (Fig.23c). As it is possible to see, the trends obtained in the present work are in good agreement with both the compressive mechanism proposed by Ashby and Gibson [61] and with the trends observed in the literature.

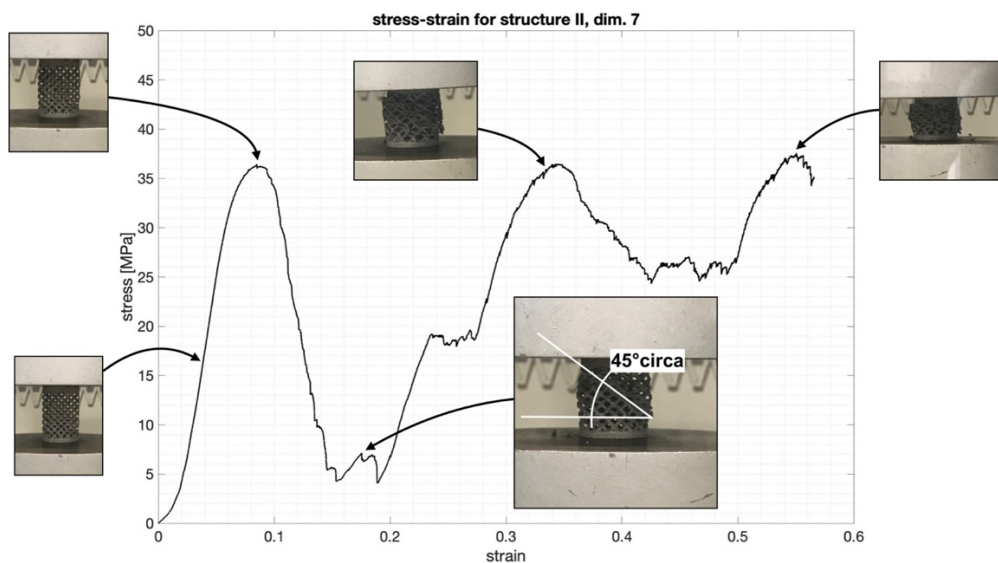


Figure 24: compressive trend for structure II with a unit cell size of 4 mm in the NTH condition

The deformation mechanism of untreated lattice structures can be observed in Figure 24. With the increase of the strain, a progressive growth of the stress carried by the structure is visible as expected. When the specimen reaches the failure point it is possible to see a consequent decreasing of the stress. Moreover, when the trend exhibits the minimum carried stress, the failure mechanism of the structure is visible. As reported by previous studies [60,69,70,80,81,84], the failure mode consists in a brittle fracture which occurs at 45° with respect to the horizontal plane. This result has been found for each sample tested. After the minimum, the stress increases with the increasing of the imposed strain, until the whole structure behaves as a bulk specimen. By analysing the trend, it is possible to see, as Figure 24 shows, that the curve is characterised by recurring twitches. This occurs because when a single strut of the whole structure collapses a sudden drop of the carried load takes place [61]. Under these circumstances, the behaviour of the lattice in the as-built condition can be compared with the behaviour of a brittle foam.

As said in paragraph 2.3, the main properties of the tested samples have been evaluated after the conduction of compressive tests. Table 9 lists the average values of the cited properties for each structure type and size.

Table 9: average properties of each different sample's unit cell type and size evaluated for the NTH condition

<b>Structure</b>	<b>Cell size [mm]</b>	<b>E* [GPa]</b>	<b>UCS* [MPa]</b>	<b>A* [%]</b>	<b>W* [J]</b>
<b>I</b>	4	0.339	19.145	10.947	1532.030
	7	0.074	4.742	10.644	200.762
	10	0.036	2.262	11.951	81.252
<b>II</b>	4	2.264	81.882	8.231	7320.737
	7	0.717	32.435	7.392	2248.406
	10	0.659	28.665	7.973	1803.502
<b>III</b>	4	1.560	60.034	8.077	4836.558
	7	1.285	54.877	8.331	4963.705
	10	0.967	39.691	7.186	2836.220

### 3.1.2 Effect of the cell size

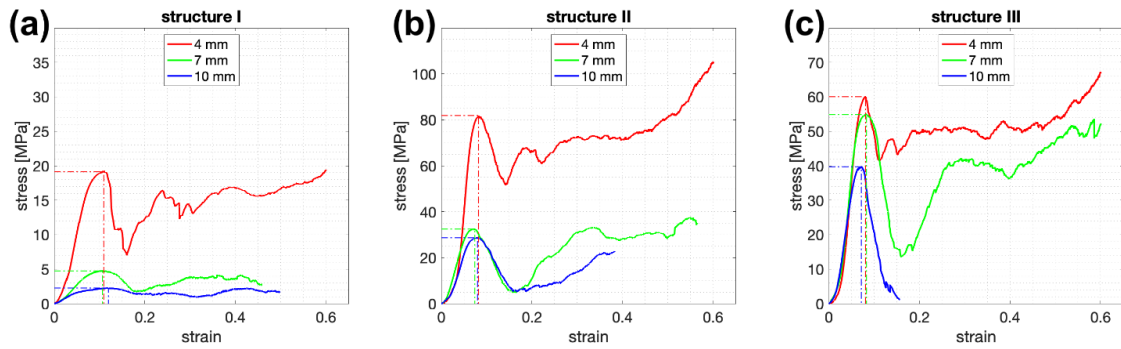


Figure 25: NTH compressive trends for structure I (a), structure II (b) and structure III (c)

For each structure type, the compressive trends of each unit cell size have been plotted in Figure 25 so as to properly study the effect of the cell size. As it is possible to notice, with the increment of the unit cell size the UCS\* decreases for each structure type. The elongation  $A^*$  does not exhibit a clear change. Analyzing the data in Table 9 also, it is possible to see that, apart from structure III, the absorbed energy up to failure decreases with the increment of the unit cell size. The Young modulus exhibits a reduction with the increasing of the unit cell size. Generally, it can be concluded that these changes are mainly imputed to the change of the relative density. As shown in the previous paragraph, there is a strong relationship between the increment of properties such as the Young modulus or the UCS and the increment of relative density. Since there is a reduction of the relative density with the increment of the unit cell size, as shown in Table 8, a decreasing of the just cited properties is well expected, following the relationships provided by Ashby and Gibson [61].

### 3.1.3 Effect of the cell type

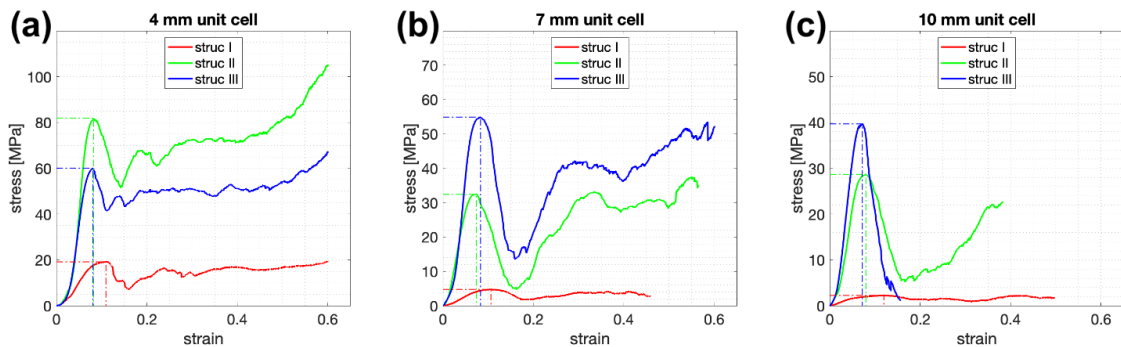


Figure 26: compressive trends for unit cells of 4 mm (a), 7 mm (b) and 10 mm (c)

Similarly to what has been done in the previous paragraph, for each unit cell size the compressive trends of each unit cell type have been plotted in Figure 26 so as to properly study the effect of the unit cell type. In this case no clear overall trend can be observed. For

instance, in relation to the 4 mm unit cell, it is indeed possible to notice that the strongest structure is structure II. Differently, in the two other cases, the strongest structure is structure III. Analyzing both the trends shown in Figure 26 and the data listed in Table 9 it is possible to conclude that the cell type does not show a clear effect since the variations of the properties are mainly imputed to the change of the relative density, as discussed in the previous paragraph.

### 3.1.4 Young modulus

From the results collected in Table 9, it is possible to make some important considerations. Firstly, the values of the Young modulus of the structures are different one from the other, ranging from 0.036 GPa for structure I-10 to 2.264 GPa for structure II-4. This behaviour can be explained with the model proposed by Ashby and Gibson [61] who, as discussed, linked the property of a generic cellular material with both the property of the bulk one and the relative density. This relationship, expressed in Equation 1, in a bi-logarithmic diagram is a straight line. Following this approach, it is possible to collect the data in this kind of graph.

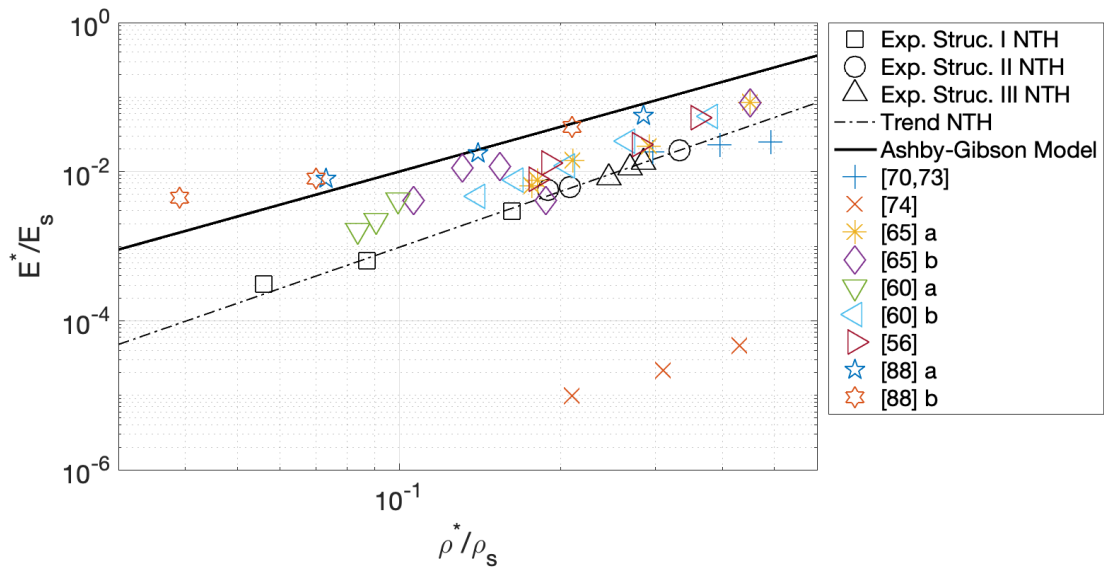


Figure 27: bi-logarithmic diagram showing the relationship between the relative Young modulus and the relative density

In Figure 27 it is possible to see that the experimental results follow a law similar to the one proposed by Ashby and Gibson [61]. The difference between the two trends is basically in the value of the constant  $C_1$  and the exponent of the relative density. This kind of result was obtained also by other works found in the literature [56,60,65,66,68–70,73,81,88]. Specifically, as far as the presented experimental results are concerned, the value of  $C_1$  is 0.301 and the value of the exponent is 2.493. As it is also possible to understand from Figure

27, the experimental trend is almost parallel to the Ashby-Gibson model and it is placed below it. This suggests that the lattice structures, contrary to cellular materials in general (for example foams), exhibit minor stiffness with the same relative density. This behaviour is given by the fact that the lattice structures have a lot of sharp edges since they are made of repetitions of a unit cell. These points behave as stress concentration points, decreasing the stiffness of the material.

From the analysis of Figure 27, another important consideration can be carried out. As it is possible to see there are a lot of data with similar values of relative density but very different values of relative Young modulus. Some of these cited data are listed in Table 10.

Table 10: comparisons between some of the collected data with similar values of relative density

Data	Structure type	Cell size [mm]	$\rho^*/\rho_s$ [%]	Strut size [mm]	Strut length [mm]	$E^*$ [GPa]
I-4	Dode Thin	4	16.155	0.297	1.732	0.339
[60]	Rombi Dode	3.75	16.480	0.940	2.540	0.890
II-7	GStructure 3	7	20.808	1.432	1.884	0.717
[60]	Rombi Dode	3	20.540	0.860	2.070	1.380
II-7	GStructure 3	7	20.808	1.432	1.884	0.717
[88]	Octet Truss	-	21.000	-	-	4.640
III-7	Rombi Dode	7	26.859	1.382	2.467	1.285
[60]	Rombi Dode	2.14	26.640	0.770	1.690	2.99
III-7	Rombi Dode	7	26.859	1.382	2.467	1.285
[56]	Dode Thin	-	28.000	0.800	-	12.900
III-4	Rombi Dode	4	28.523	0.704	1.410	1.560
[56]	Dode Thin	-	28.000	0.800	-	12.900
III-4	Rombi Dode	4	28.523	0.704	1.410	1.560
[70,73]	Cross	2.84	29.680	0.882	2.840	2.130
III-4	Rombi Dode	4	28.523	0.704	1.410	1.560
[88]	Octet Truss	10	28.500	1.660	-	6.519
[81]	Rombi Dode	4.29	14.030	1.080	3.130	0.540
[88]	Octet Truss	-	14.000	1.100	-	2.076

As it is possible to see from Table 10, there are quite a few data with similar values of relative densities showing different values of Young modulus. This results to be slightly in contrast with the Equation 1, one of the most important laws presented by Ashby and Gibson [61]. From an accurate analysis of Table 10, it is possible to notice that, despite having a similar relative densities, each pair of data shows also different values of geometrical features such

as cell size, strut size and strut length. This can suggest that, differently from foams, lattice structures may exhibit a shape effect based on the singular effects of the just cited geometrical features. To fully understand this behaviour, further analysis will be conducted to refine the Ashby-Gibson model for lattice structures with the addition of the mentioned shape effect.

### 3.1.5 Ultimate Compressive Strength

Important considerations can be also done analysing the values of UCS\* in Table 9. The Ultimate Compressive Strength ranges from 2.262 MPa for structure I-10 to 81.882 MPa for structure II-4. Ashby and Gibson, in their cited model [61], proposed another linear relationship in a bi-logarithmic diagram for the prediction of the UCS\*. This relationship, expressed in Equation 2, is a straight line in a bi-logarithmic diagram, similarly to previous discussed law regarding  $E^*$ . As analysed for the Young modulus, it is possible to collect the data in a similar diagram.

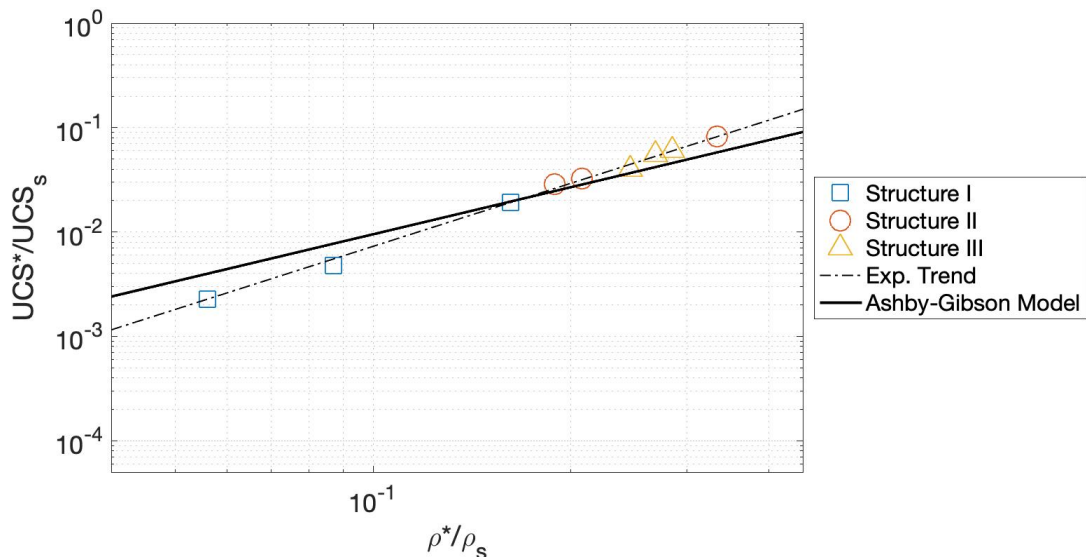


Figure 28: bi-logarithmic diagram showing the relationship between the relative UCS and the relative density

In Figure 28 the experimental results and the trend represented by Equation 2 are shown. Also in this case the collected and computed data show a trend very similar to the one proposed by Ashby and Gibson [61]. Differently from the previous analysed Young modulus, the collected experimental data are closer to the Ashby-Gibson law (Equation 2) [61]. Nevertheless, the value of the constant in the computed experimental trend is equal to 0.744 and the exponent is equal to 2.012. This kind of result was found also in other works of literature [70,73]. Despite there is a small change regarding the trend of the experimental data, the Ashby-Gibson law expressed in Equation 2, in this case, represents a good estimate for the prediction of the UCS\* of a lattice structure taking into account its relative density only.

### 3.1.6 Absorbed energy up to failure

Regarding the energy absorption, Ashby and Gibson [61] analysed the absorbed energy up to densification. In the present work, the evaluated energies listed in Table 9 have been treated with the specific aim of investigating whether there is a linear relationship in a bi-logarithmic diagram between the relative absorbed energy up to failure and the relative density. The just cited relative absorbed energy is given by the ratio between the energy absorbed by the lattice structure  $W^*$  and the energy absorbed by the bulk material  $W_s$ . In order to evaluate this last parameter the theoretical compressive trend of the bulk specimen has been. The energy absorbed by the bulk material up to failure can be evaluated by the following expression:

$$W_s = \frac{1}{2} \cdot \frac{UCS_s^2}{E_s} \cdot V_s \quad (8)$$

In Equation 8, it is possible to identify the ultimate compressive strength of the bulk material  $UCS_s$ , the Young modulus of the bulk material  $E_s$  and lastly the volume of the bulk specimen  $V_s$ , evaluated as the volume of a cylinder with a 20 mm diameter and a height of 26 mm. At this point, the experimental results can be plotted in a bi-logarithmic diagram and are shown in Figure 29.

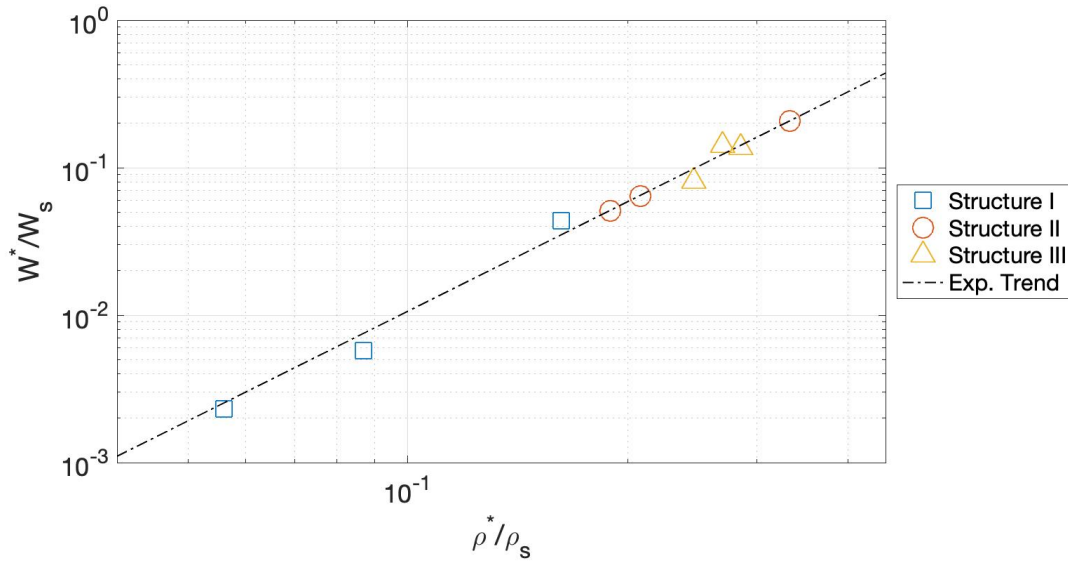


Figure 29: bi-logarithmic diagram showing the relationship between the relative absorbed energy up to failure and the relative density

As it is possible to see, the experimental results fit well in an experimental law similar to the previously described relationships expressed by Equation 1 and Equation 2. Following this, the experimental trend has been computed. Equation 9 shows this empirical law:

$$\frac{W^*}{W_s} = 3.153 \left( \frac{\rho^*}{\rho_s} \right)^{2.472} \quad (9)$$

### 3.1.7 Microstructure analysis

The microstructure of as-built bulk specimens has been discussed in the introduction of the present work. Most of the analysed studies found the presence of fine acicular  $\alpha$  and  $\beta$  [9,30,44,48,50,87]. Some other studies, apart from the cited phases, observed also the presence of the martensitic phase  $\alpha'$  [81,85]. Focusing on lattice structures, some works of literature have been able to observe a much clear presence of martensite [45,60].

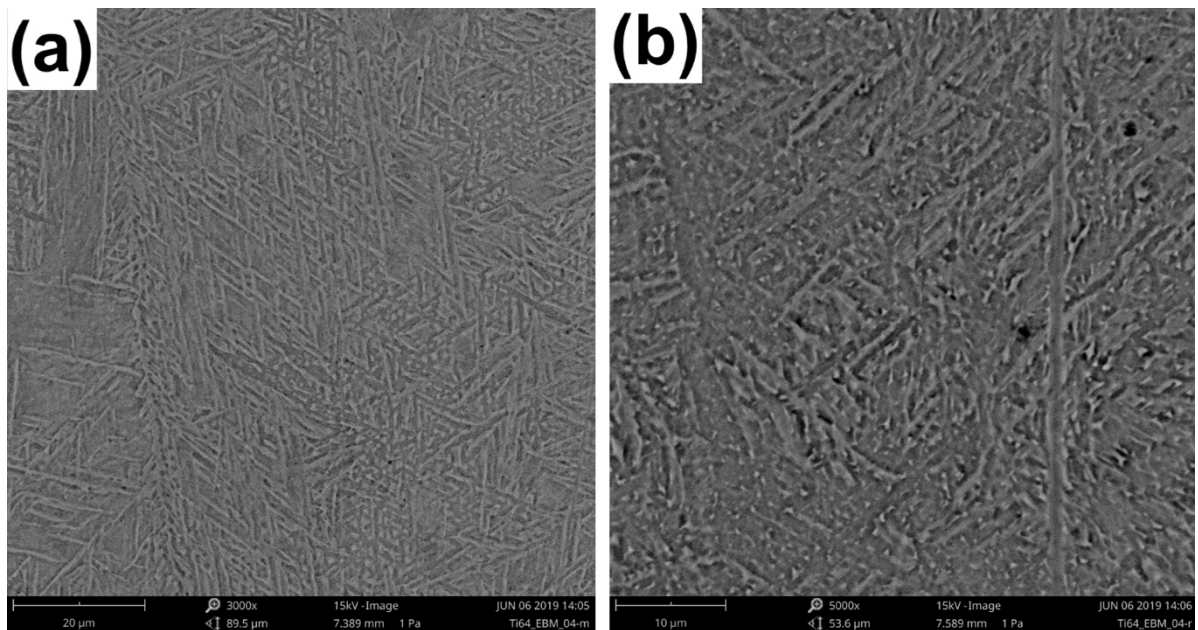


Figure 30: microstructure of the I-4 design in the NTH condition at 3000x (a) and 5000x (b)

In the present study, the microstructure of as-built samples has been analysed. Analysing Figure 30 it is clear that the as-built samples show the presence of  $\alpha'$  martensite. This specific phase forms with a metastable transformation depending by the kinetics of the cooling phase. Since the as-built condition has not been heat-treated, it can be concluded that during the EBM process the cooling rate guarantees the formation of martensite. For bulk samples, as said, this specific phase has not been always observed. Since lattice structures are porous materials, the heat exchange between the powder and the struts during the cooling phase may ensure the formation of  $\alpha'$ . This phase, despite having a great mechanical strength, is fragile. This behaviour explains the failure mode of as-built lattice structures which consists in brittle fracture with crush bands at  $45^\circ$  with respect to the horizontal plane.

## 3.2 Mechanical behaviour of heat-treated lattice structures

### 3.2.1 Compressive trends

After the conduction of both heat treatments, HT1 and HT2 samples were tested in the same conditions of the NTH samples. Figure 31 shows the stress-strain trends of the same designs discussed in paragraph 3.1.1.

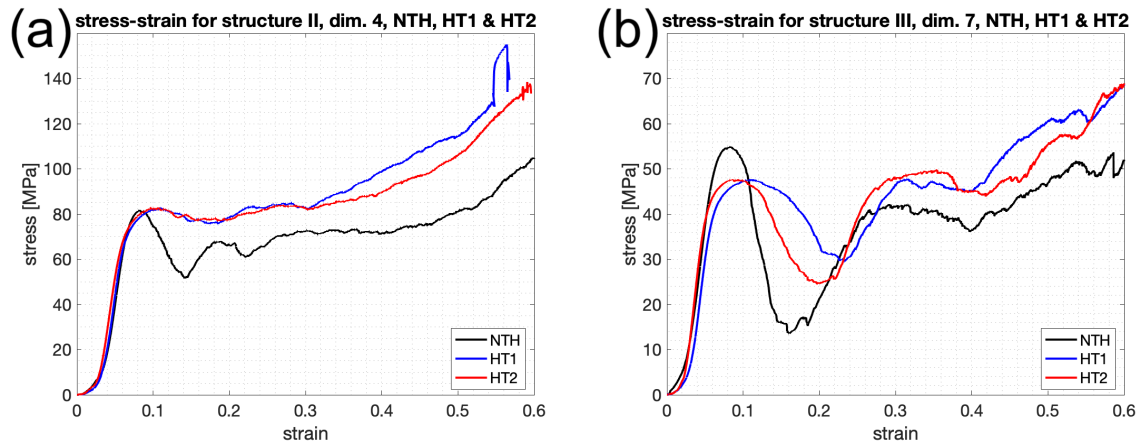


Figure 31: NTH, HT1 and HT2 trends observed regarding structure II with unit cell of 4 mm (a) and structure III with unit cell of 7 mm (c)

From the analysis of Figure 31, it is possible to compare the trends for the same design in the three different conditions analysed (NTH, HT1 and HT2). The behaviour of lattice structures after the conduction of thermal treatments is still made up of three main segments. In the first part, the behaviour of the material is very similar in all the conditions and is still characterized by the elastic behaviour of the lattice structure. Nevertheless, the failure point seems to appear in a slightly different position. The second segment of all the trends is still characterized by a plateau region in which it is possible to notice the progressive collapse of the layers of the lattice. Analyzing Fig.31b this cited trend is clear since the stress shows sudden drops after the reaching of the failure point. Nevertheless, these cited fluctuations seem to be less wide. This particular behaviour is very distinct in Fig.31a, where the cited drops are slightly recognizable. The last segment of the stress-strain trends appears to be once again characterized by the elastic behaviour of the bulk material, as previously discussed for the NTH samples. Overall, since after the failure point HT1 and HT2 stress-strain trends are almost always higher than the NTH trend, it is possible to state that lattice structures may show a ductility enhancement in the heat-treated conditions. This behaviour will be fully discussed in the following paragraphs regarding the analysis of mechanical property such as the elongation at failure  $A^*$  and the absorbed energy up to failure  $W^*$ .

Similar results have been reached also by Xiao et al. [78] studying the effects of working temperature on the compressive behaviour of lattice structures.

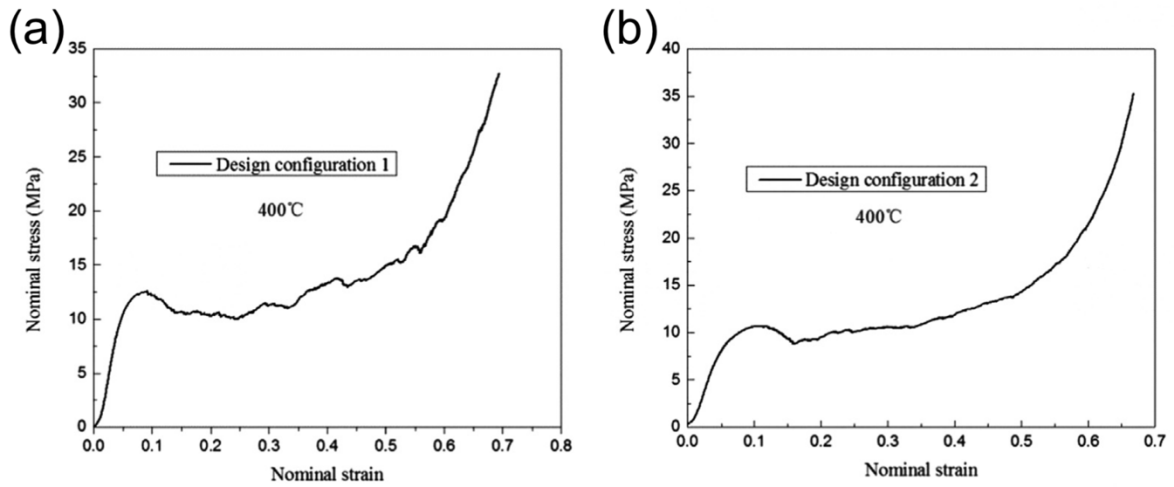


Figure 32: stress-strain trends for configuration 1 (a) and configuration 2 (b) studied by Xiao et al. [78]

As can be easily understand analyzing Figure 32, lattice structures show smoother trends when the compression test is performed at high temperatures. This behaviour has been explained by Xiao et al. [78] who suggested a change in the failure mode into a more homogeneous one since they did not notice any shear bands. The same kind of results have been observed also in the present work.

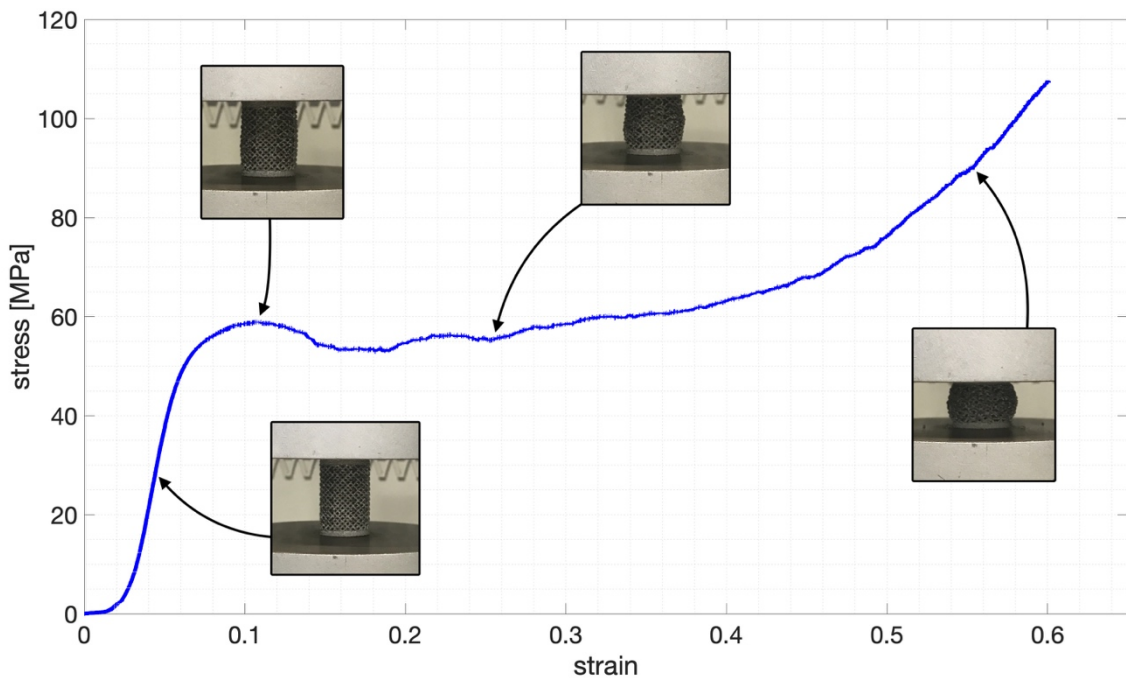


Figure 33: compressive trend for structure III with unit cell size of 4 mm in the HT1 condition

As Figure 33 depicts, there is no clear shear band, as reported by Xiao et al. [78] and the material behaves overall in a much more homogeneous way. Additionally, in the last segment of the compressive trend, the barreling phenomenon can be observed. This behaviour has never been showed in the NTH compressive trends. Thus, it can be concluded that heat-treated lattice structures show a different failure mode with respect to the untreated ones which, as previously mentioned, exhibit brittle fracture with shear bands at  $45^\circ$  with respect to the horizontal plane [60,69,70,80,81,84].

After the conduction of the compressive tests on the HT1 and HT2 samples, it has been possible to evaluate the main mechanical properties as discussed in paragraph 2.3. Table 11 lists the average values of the cited properties for each structure type and size and each heat-treated condition.

Table 11: average properties of each different sample's unit cell type and size evaluated for the HT1 and HT2 conditions

Struct.	Cell size [mm]	$E^*_{HT1}$	$E^*_{HT2}$	$UCS^*_{HT1}$	$UCS^*_{HT2}$	$A^*_{HT1}$	$A^*_{HT2}$	$W^*_{HT1}$	$W^*_{HT2}$
		[GPa]	[GPa]	[MPa]	[MPa]	[%]	[%]	[kJ]	[kJ]
<b>I</b>	4	0.357	0.357	17.067	17.782	14.850	13.300	2.393	1.907
	7	0.087	0.083	4.478	4.624	12.254	13.606	0.253	0.288
	10	0.035	0.035	2.260	2.203	14.729	12.954	0.102	0.088
<b>II</b>	4	2.401	2.304	82.658	82.694	11.031	10.721	13.462	13.569
	7	0.770	0.901	32.486	33.869	12.627	12.862	4.594	4.704
	10	0.711	0.707	26.851	26.583	8.408	8.436	2.006	1.786
<b>III</b>	4	1.683	1.639	58.940	56.156	10.823	11.031	8.408	7.692
	7	1.427	1.548	47.653	47.713	11.208	9.350	6.795	5.659
	10	1.208	1.237	40.287	39.291	7.767	7.800	3.184	3.051

### 3.2.2 Effect of the cell size and type

The compressive trends of structure I have been plotted in Figure 34 for each unit cell size so as to properly study both the effects of cell size on the heat-treated samples.

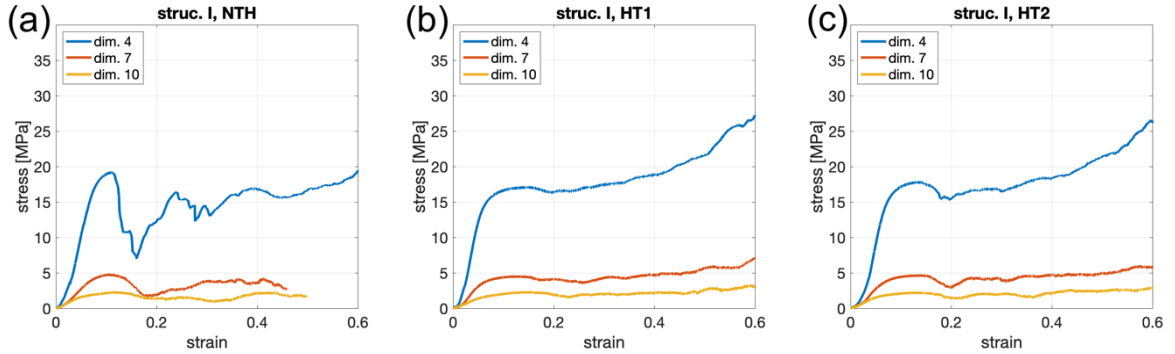


Figure 34: compressive trends for structure I in the condition NTH (a), HT1 (b) and HT2 (c)

Samples in the NTH condition display (Fig.34a), as previously said, a decrease of the UCS\* with the increment of the unit cell size. This behaviour is preserved also in the heat-treated conditions (Fig.34b and Fig.34c). As far as the elongation at failure  $A^*$  is concerned, analyzing the data in Table 11 for each heat-treated condition, it is not possible to notice a clear change. This kind of result has been obtained also, as discussed, for the NTH condition. From the analysis of the values of the energy absorbed up to failure, it can be observed that  $W^*$  decreases with the increment of the unit cell size. This behaviour is the same as the one discussed for the NTH samples. The Young modulus exhibits a reduction with the increasing of the unit cell size for both the HT1 and HT2 conditions. These results have been obtained also for structure I in the NTH condition. In addition, this kind of trend has been found also from the same analysis conducted on structures II and III. Thus it can be concluded that the heat treatments do not change the effect of the cell size on the mechanical behaviour of lattice structures. To fully understand the effect of the unit cell type, the data in Table 11 of the samples with the same unit cell size can be compared. For both the conditions HT1 and HT2 the behaviour is the same as the one discussed for the NTH condition. No clear overall trend can be indeed observed. For instance, as done previously for the NTH samples, in relation to the 4 mm unit cell, it is possible to see that the strongest structure is structure II for both the heat-treated cases. In the same way of the NTH analysis, in the two other cases, the strongest structure is structure III. This result occurs in the HT1 and HT2 conditions for the same reasons for which occurs in the NTH condition. In fact, analyzing the values displayed in Table 11 it is possible to state that the cell type does not show a clear effect since the variations of the properties in the heat-treated conditions are still mainly imputed to the relative density.

### 3.2.3 Young modulus

In the paragraph 3.1.4 the Young modulus of lattice structures in the as-built condition has been discussed. In order to better discuss the variations of Young modulus, Figure 35 depicts the values of  $E^*$  for each design in all the three different conditions analysed.

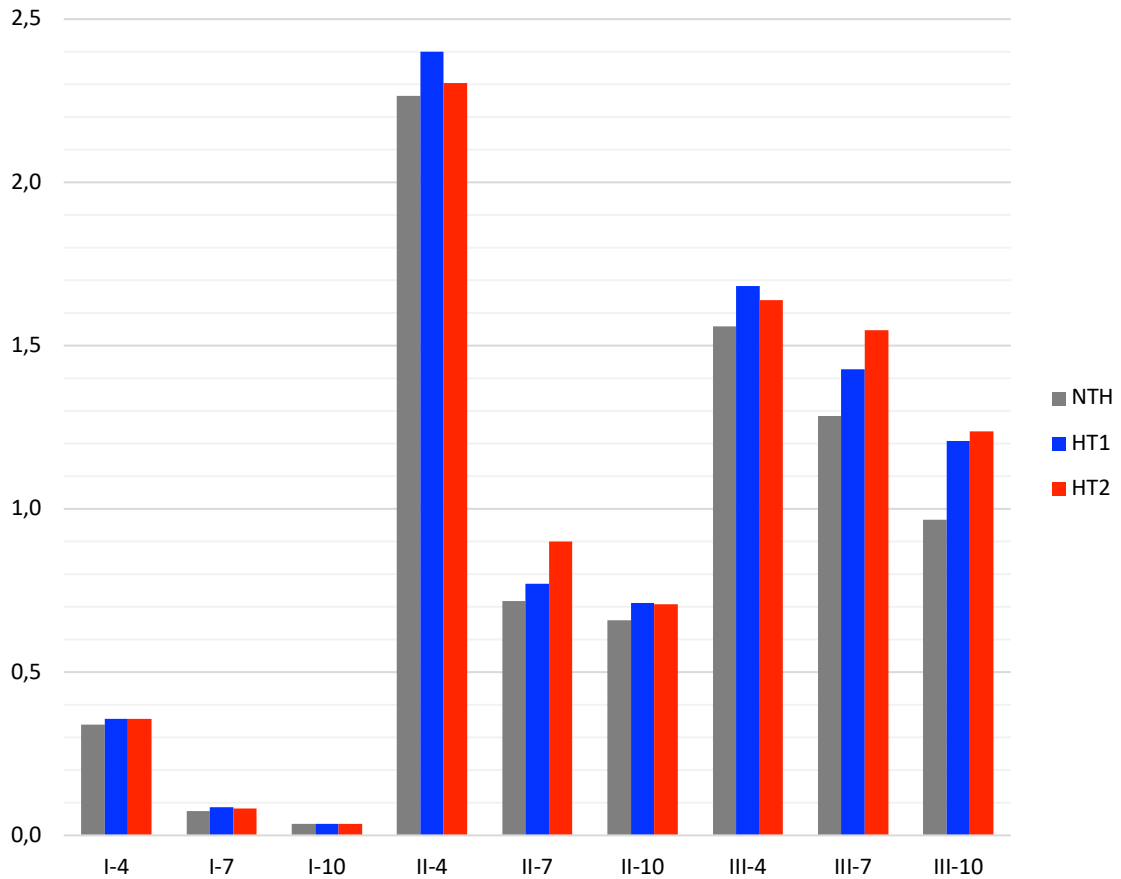


Figure 35: Young modulus values for the three analysed conditions

Analyzing the data in Figure 35 it is possible to see that the values of  $E^*$  for structure I do not show any kind of trend considering the NTH and the heat-treated conditions. In addition, there is no significant variation of the cited values. For the two other structures, the values of Young modulus change more consistently but a clear trend can not be observed since, for instance, the design III-10 shows a discrete change moving from the NTH to the HT1 and HT2 conditions, but the design II-10 does not show this type of change. Thus, it can be concluded that the heat treatments do not affect significantly the Young modulus.  $E^*$  is indeed still clearly connected to the relative density. Analyzing the data displayed in Figure 35 it can be found that, as shown for the NTH conditions, the values of the Young modulus for the heat-treated conditions follow an Ashby-Gibson-like relationship [61]. The differences between the experimental trends and the Ashby-Gibson model (Equation 1) can be found once again

in the values of the constant and the exponent of the cited law.  $C_1$  assumes indeed the values of 0.280 and 0.219 while the exponent is 2.365 and 2.168 for conditions HT1 and HT2 respectively. As said, these trends in a bi-logarithmic diagram are straight lines. Following this approach, the results are collected in Figure 36.

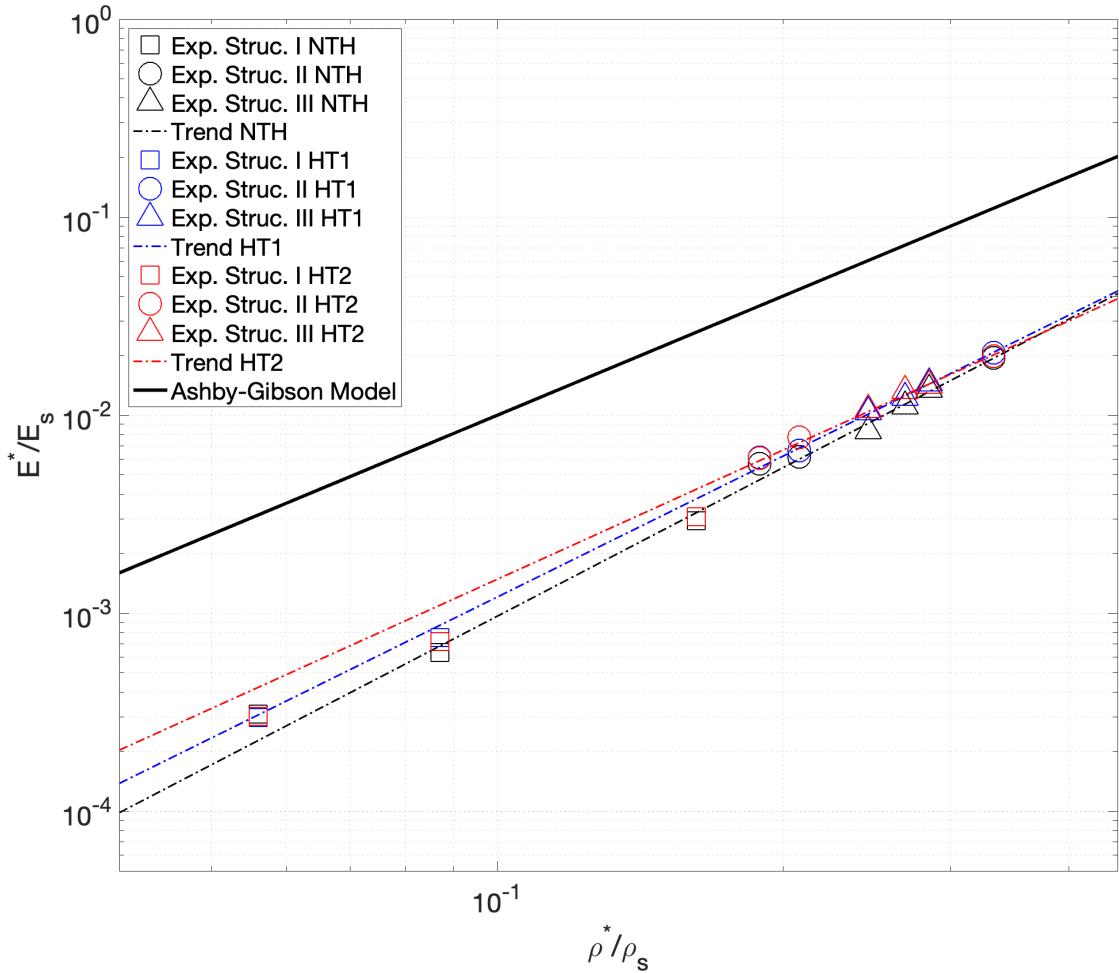


Figure 36: bi-logarithmic diagram showing the relationship between the relative Young modulus and the relative density for conditions NTH (in black), HT1 (in blue) and HT2 (in red)

As previously analysed for the NTH samples, since no significant change can be observed in HT1 and HT2 conditions, the experimental trends for heat-treated lattice structures are still almost parallel to the Ashby-Gibson model and they are still placed below it.

### 3.2.4 Ultimate Compressive Strength

In the paragraph 3.1.5 the Ultimate Compressive Strength of lattice structures in the as-built condition has been discussed. In order to better discuss its variations, Figure 37 depicts the values of UCS\* for each design in all the three different conditions analysed.

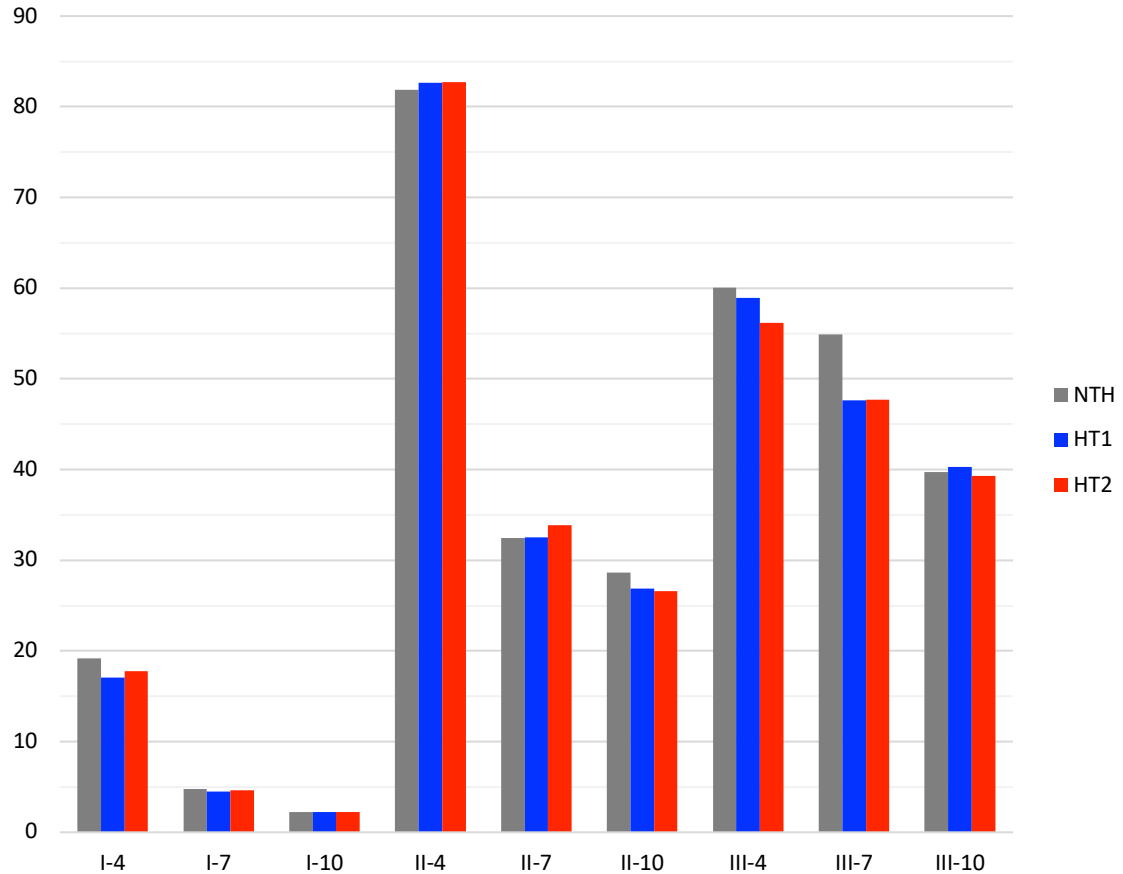


Figure 37: Ultimate Compressive Strength values for the three analysed conditions

From the analysis of the data depicted in Figure 37 it is possible to notice that for structure II no particular trend can be observed since for the II-4 and II-7 designs the heat treatments produce a slightly enhancement of the UCS\*, but for the II-10 design they cause a decreasing of the analysed property. This kind of analysis can be conducted also for structure I, which does not exhibit a considerable change of UCS\* moving from the NTH condition to the heat-treated ones. Focusing on structure III, the heat treatments cause a UCS\* worsening apart for the III-10 design, which does not show a clear change moving from the NTH to the HT1 and HT2 conditions. Thus, it can be concluded that the heat treatments do not affect significantly the Ultimate Compressive Strength. As the Young modulus, UCS\* is indeed still clearly connected to the relative density. Ashby and Gibson, as previously said, proposed another relationship in a bi-logarithmic diagram for the prediction of UCS\* (Equation 2). The differences between the experimental trends and the Ashby-Gibson model can be found also in this case in the values of the constant and the exponent of the law expressed in Equation 2.  $C_5$  assumes indeed the values of 0.697 and 0.806 while the exponent is 1.941 and 2.100 for conditions HT1 and HT2 respectively. As previously mentioned, these

trends in a bi-logarithmic diagram are straight lines. Following this approach, the results are collected in Figure 38.

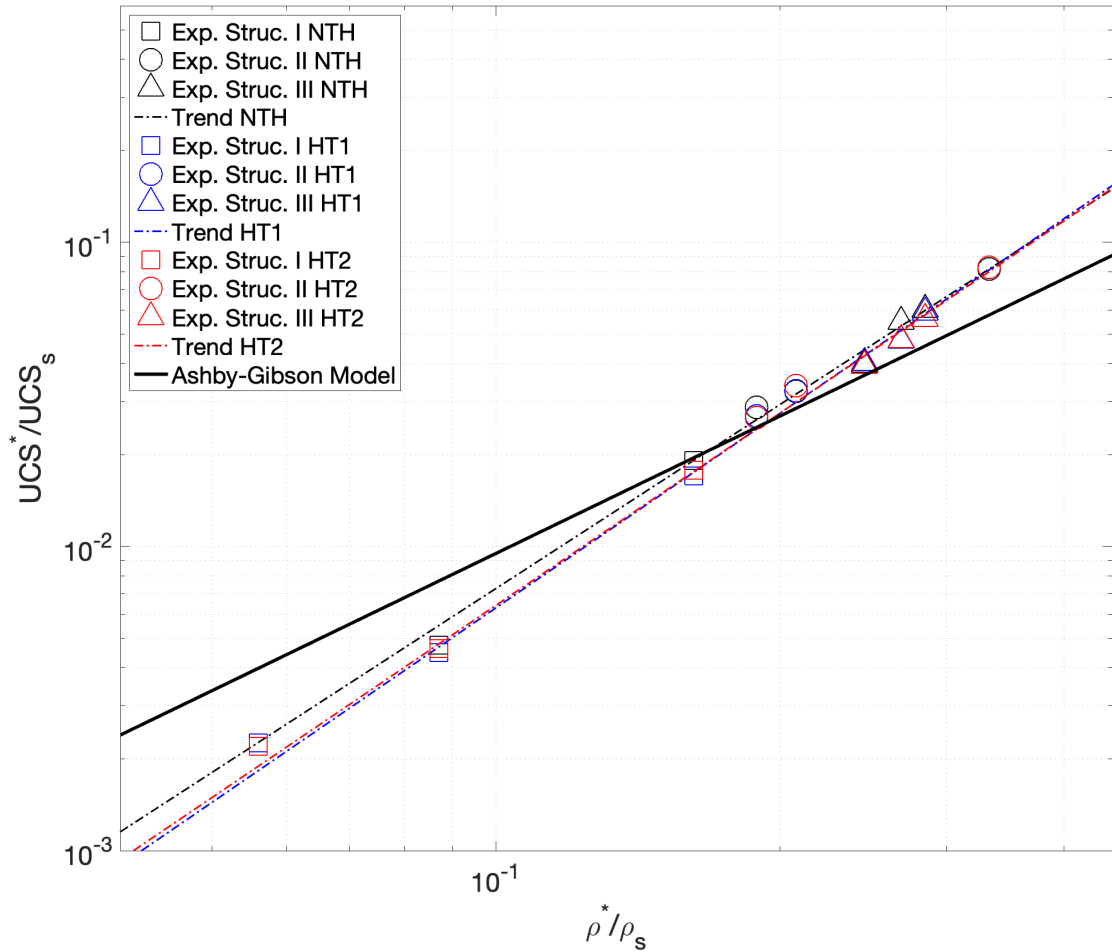


Figure 38: bi-logarithmic diagram showing the relationship between the relative Ultimate Compressive Strength and the relative density for conditions NTH (in black), HT1 (in blue) and HT2 (in red)

Analysing Figure 38, the Ashby and Gibson law expressed in Equation 2 still represents a good estimate for the prediction of the  $UCS^*$  of a lattice structure taking into account its relative density only.

### 3.2.5 Elongation at failure

As previously stated, the elongation at failure  $A^*$  represents the strain reached in the failure point by the lattice structure. In a first analysis, it has been observed that this property is dependent mainly by the structure type in the as-built condition. In the present paragraph the effects of the heat treatments on the values of  $A^*$  are discussed. Figure 39 depicts the values of the elongation at failure for each design in all the three different conditions analysed.

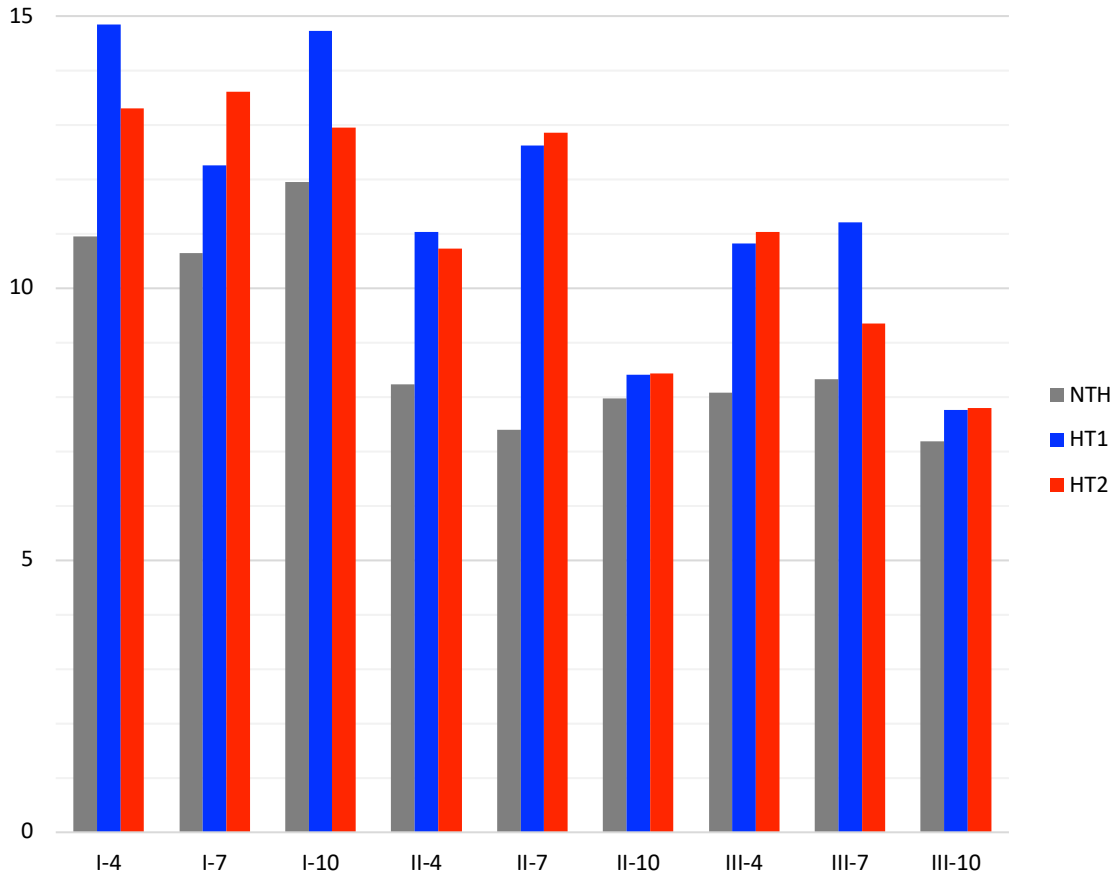


Figure 39: Elongation at failure values for the three analysed conditions

Analysing the data in Figure 39 it is possible to see that the values of  $A^*$  show in this case a clear trend. For each structure in both the heat-treated conditions an enhancement of elongation at failure can be observed. This change can be also observed analyzing the stress-strain curves depicted in Figure 31. Comparing the HT1 and HT2 conditions, a clear trend in the enhancement of  $A^*$  can not be observed since for some designs the HT1 condition ensures the best values of elongation at failure and for other the best condition is represented by HT2. Since the values of  $UCS^*$  do not show an evident change in the heat-treated conditions, it can be concluded that generally the failure point of the compressive trend moves towards higher values of strain. Thus, an enhancement of the ductility of the lattice structures is expected. In the next paragraph the absorbed energy up to failure is discussed to fully prove this trend from a mechanical point of view.

### 3.2.6 Absorbed energy up to failure

As previously said for the as-built condition, Ashby and Gibson [61] analysed the absorbed energy up to densification. Analysing the compressive trends in Figure 31 it is clear that, up to the densification point, the absorbed energy reaches higher values in both the heat-treated

conditions. This change is given by the evident increase of the area below the stress-strain trends. An enhancement of the material's ductility is expected, as suggested by the analysis conducted in the previous paragraphs. In order to better discuss this behaviour, Figure 40 depicts the values of  $W^*$  for each design in all the three different conditions analysed.

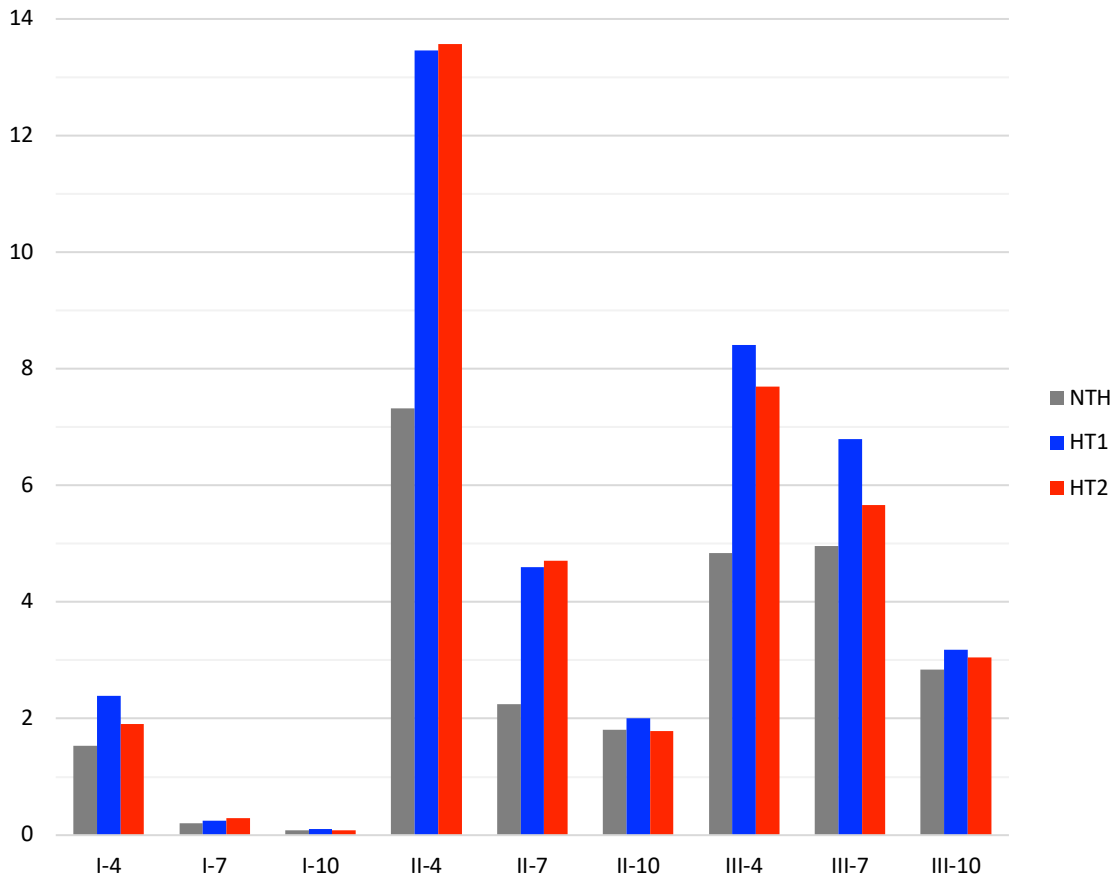


Figure 40: Absorbed energy up to failure values for the three analysed conditions

From the Figure 40 analysis the clear effect of the heat treatments on the mechanical behaviour of lattice structures can be observed. Generally, lattice structures in the HT1 and HT2 conditions show indeed a higher value of  $W^*$ . Analysing the differences between the two heat-treated conditions, no evident difference between the two heat treatments can be observed since for some designs the better condition is shown by the HT1 samples, while for other the better is shown by the HT2 samples. Thus, it can be concluded that heat treatments enhance the ductility of Ti-6Al-4V lattice structures manufactured by EBM.

As previously analysed for the as-built condition, it is possible to investigate the trends of the relative absorbed energy up to failure with respect to the relative density. In Figure 41 the experimental results have been plotted in a bi-logarithmic diagram.

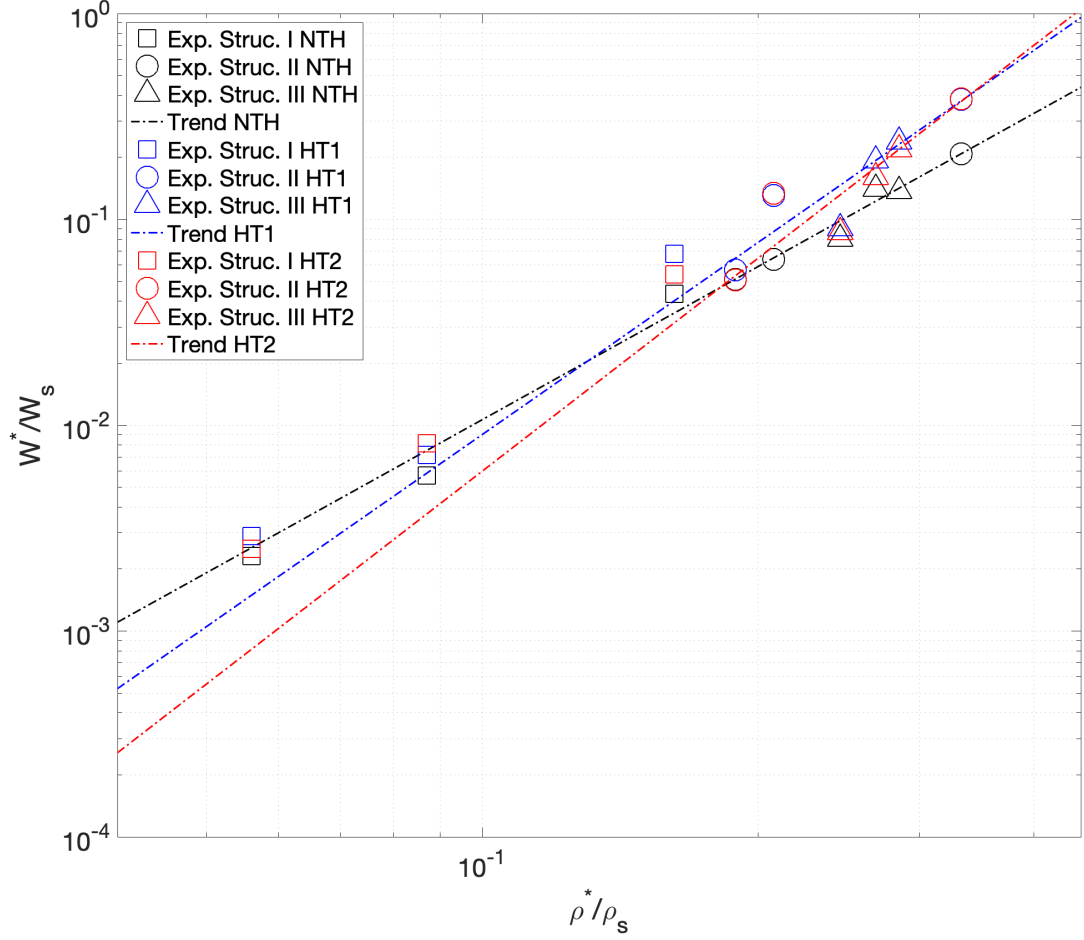


Figure 41: bi-logarithmic diagram showing the relationship between the relative absorbed energy up to failure and the relative density

As it is possible to see, the experimental results for heat-treated conditions fit once again well in an experimental law similar to the previously described relationship expressed by Equation 9. Following this, this experimental trends have been computed. Equations 10 and 11 show these empirical laws:

$$\frac{W_{HT1}^*}{W_s} = 11.370 \left( \frac{\rho^*}{\rho_s} \right)^{3.101} \quad (10)$$

$$\frac{W_{HT2}^*}{W_s} = 16.360 \left( \frac{\rho^*}{\rho_s} \right)^{3.437} \quad (11)$$

Analysing the values of the constants and exponents in Equation 9, 10 and 11 it is possible to notice a progressive increase moving from the NTH to the HT2 condition. Thus, it can be concluded that the absorbed energy up to failure is dependent by the relative density of the material. In addition this property is enhanced by performing heat treatments.

### 3.2.7 Microstructure analysis

As shown in the paragraph 3.1.7, the microstructure of as-built samples is made of martensite. Most of the works analysed show the presence of acicular  $\alpha$  and  $\beta$  in the as-built conditions. These studies, investigating the effects of heat treatment on the microstructure, have found out that the laths of  $\alpha$  show an enlargement in the heat-treated conditions.

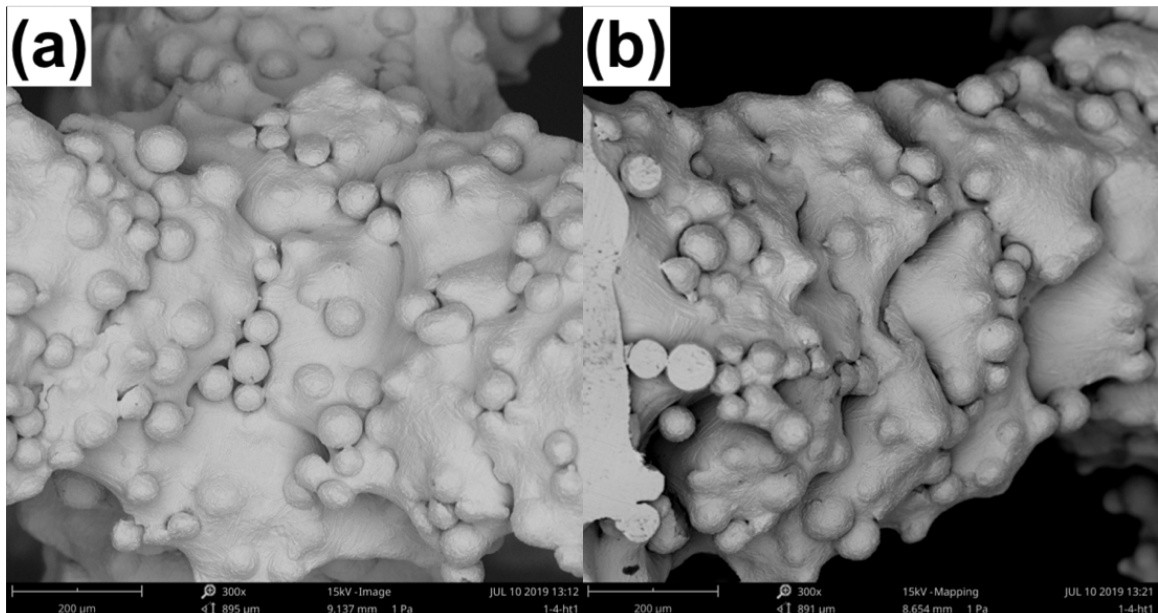


Figure 42: SEM images showing the surface of the junction of the struts (a) and the surface of a single strut (b) for the design I-4 in the HT1 condition

From Figure 42 it is possible to see that the external surface of the struts presents powder attached. In addition, the different melted layers are clearly visible. These specific points can represent crack initiation points.

In order to properly study the effects of the heat treatments, as said, two different thermic cycles have been performed on the samples. During this phase, the  $\beta$  fraction in the Ti-6Al-4V alloys increases continuously from the room temperature to 950°C and to 100%. This happens because the temperature chosen for the first performed heat treatment (HT1) is very close to the  $\beta$ -transus temperature (995°C). Increasing more the temperature of the heat treatment and reaching 1050°C (HT2), a recrystallization may occur depending on the time the lattice structures are maintained at this specific temperature. This can lead to an enlargement of the  $\beta$  grains.

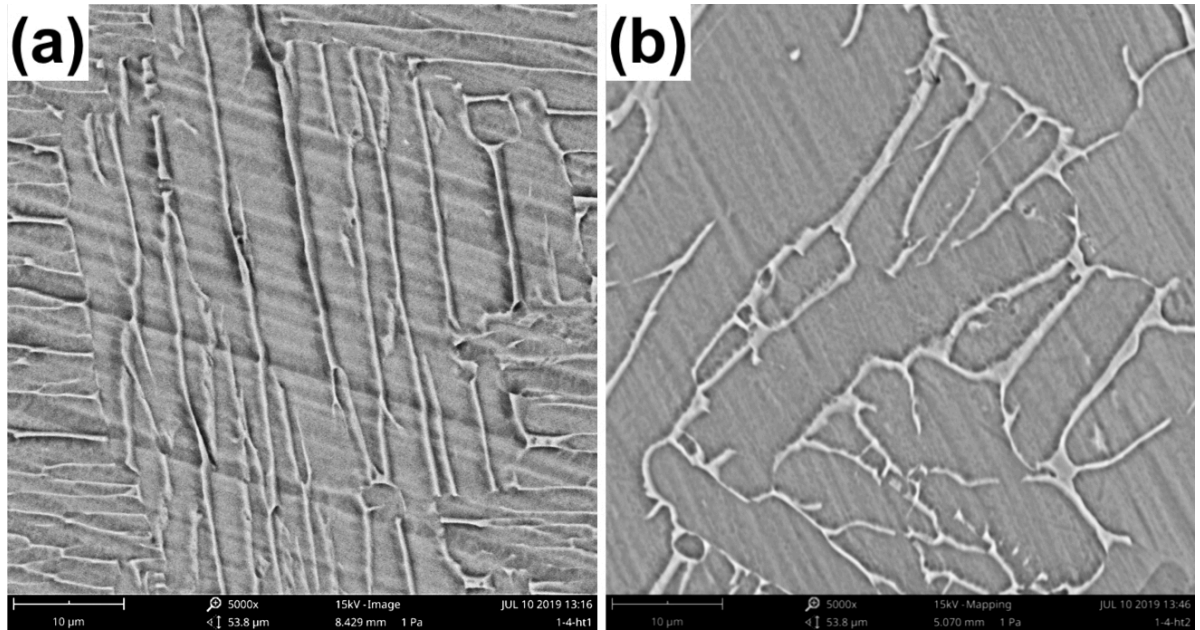


Figure 43: microstructure of the I-4 design in the HT1 (a) and HT2 (b) conditions

Figure 43 depicts the microstructure of the I-4 design in both heat-treated conditions with the same scale. Firstly, the metastable  $\alpha'$  phase is not visible. This result has been observed in each design. Thus, it can be concluded that heat treatments are able to erase the martensitic phase. Comparing Fig.43a and Fig.43b it is clear that in the HT1 condition the prior  $\beta$  grain is visible, while in the HT2 condition the prior  $\beta$  grain is not.

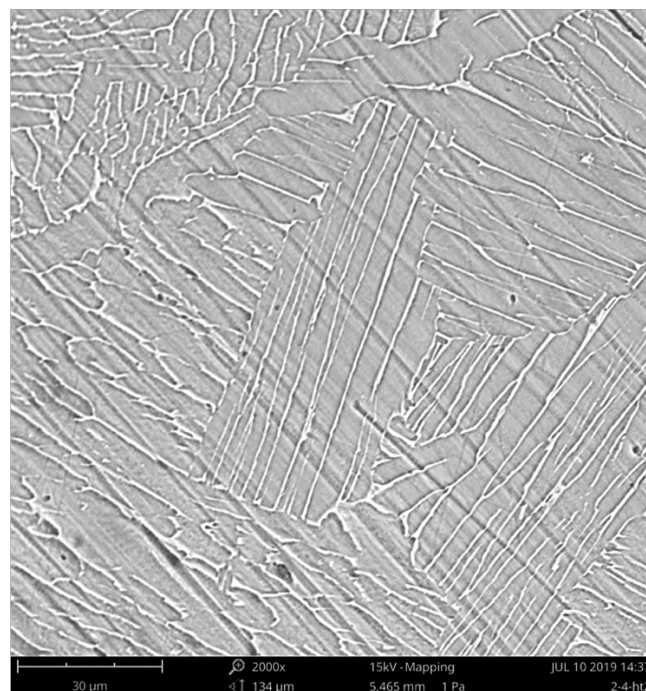


Figure 44: microstructure of the I-4 design in the HT2 condition

In addition, analysing the microstructure at a minor scale (Figure 44), it has been possible to observe also the formation of the  $\alpha$  phase in the Widmännstatten condition. As far as the width of the plates is concerned, the laths of  $\alpha$  in the HT1 condition are less coarse with respect to the one in the HT2 condition. Thus, it can be concluded that, since the microstructure of as-built lattice structures exhibits  $\alpha'$  while in the heat-treated conditions exhibits the presence of  $\alpha+\beta$ , an improving of ductility is well expected. This conclusion is in good agreement with the analysis of the mechanical behaviour of lattice structures conducted in the previous paragraphs.

## 4 Conclusions

In the present work the effects of two different heat treatments on the mechanical behaviour of Ti-6Al-4V lattice structures manufactured by EBM have been conducted. The review of the literature has highlighted that, despite the mechanical behaviour of such structures in the as-built condition has been quite comprehensively studied, a deep lack of knowledge on the effects of the heat treatments has been detected. The present study has so focused on this specific characterization and, after the analysis of the results, it can be concluded that:

- a. lattice structures in the as-built condition present a failure mode which consists in brittle fracture with the formation of crack bands at  $45^\circ$  with respect to the horizontal plane. Analysing the heat-treated conditions this has not been observed. In fact, a much more homogeneous failure mode has been detected;
- b. as far as the effect of the unit cell size is concerned, it has been found that with the increasing of the unit cell size there is a progressive reduction of properties such as  $E^*$  and  $UCS^*$  for all the three different analysed conditions. This result is in good agreement with the Ashby and Gibson model [61] since with the increasing of the unit cell size a decrease of the relative density follows. No clear effect of the unit cell size on the elongation at failure  $A^*$  has been detected;
- c. no clear effect of the unit cell type has been found analysing the values of the studied mechanical properties in all the three different mentioned conditions. Thus, it can be concluded that the Young modulus is mainly influenced by the relative density, as suggested by Ashby and Gibson [61]. In spite of this, comparing designs with similar relative density, it has been found that there is a big difference in the values of the analysed mechanical properties. Further analysis will be conducted to fully understand if there is a proper shape effect on the mechanical behaviour of lattice structure;
- d. the computed values of relative Young modulus follow an exponential law with respect to the relative density, as suggested by Ashby and Gibson [61]. In spite of this, a modification of the constant and the exponent of the cited law need to be done for both the as-built and heat-treated conditions to correctly express the compressive behaviour of lattice structures;
- e. from the comparison of the Young modulus values of as-built and heat-treated lattice structures, no clear difference has been found. Thus, it can be concluded that heat treatments do not cause a modification of Young modulus;

- f. the analysed values of relative Ultimate Compressive Strength follow an exponential law with respect to the relative density, as suggested by Ashby and Gibson [61]. In spite of this, as concluded also for the Young modulus, a modification of the constant and the exponent of the cited law need to be done for both the as-built and heat-treated conditions to correctly express the compressive behaviour of lattice structures;
- g. from the comparison of the UCS\* values of as-built and heat-treated lattice structures, no clear difference has been found. Thus, it can be concluded that heat treatments do not cause a modification of the UCS;
- h. the elongation at failure  $A^*$  increases moving from the as-built condition to the heat-treated ones;
- i. the relative absorbed energy up to failure follows an Ashby-Gibson-like law with respect to the relative density in all the three different conditions analysed. The values of  $W^*$  increase moving from the as-built condition to the heat-treated ones. Thus, from a mechanical point of view, it can be concluded that the heat treatments cause an enhancement of the ductility of lattice structures;
- j. the microstructure of as-built lattice structures exhibits the presence of  $\alpha'$  martensite. In spite of this, the effective presence of this phase depends on the actual cooling rate inside the construction chamber. This cooling gradient may depend on the design of the sample. Further analysis will be conducted to fully understand this specific behaviour;
- k. from a materialistic point of view, it can be concluded that both heat treatments leads to a fully  $\alpha+\beta$  microstructure, with no presence of the  $\alpha'$  martensitic phase detected;
- l. the heat treatment performed at the temperature above  $\beta$ -transus cause a slightly higher growth of the  $\alpha$  phase which results in a bigger value of the  $\alpha$  plates width;
- m. overall, since both heat-treated conditions showed a much more ductile microstructure with respect to the as-built condition, it can be comprehensively concluded that the heat treatments are able to enhance the ductility of lattice structures.

## 5 References

- [1] I. Polmear, D. StJohn, J.-F. Nie, and M. Qian, *Light Alloys: Metallurgy of the Light Metals* (Butterworth-Heinemann, 2017).
- [2] A. Saboori, D. Gallo, S. Biamino, P. Fino, and M. Lombardi, *Appl. Sci.* (2017).
- [3] M. Peters, *Titanium and Titanium Alloys Edited By* (WILEY-VCH Verlag GmbH & Co. KGaA, 2003).
- [4] A. Saboori, S. Tusacciu, M. Busatto, M. Lai, S. Biamino, P. Fino, and M. Lombardi, *J. Vis. Exp.* **2018**, e56966 (2018).
- [5] B. Dutta and F. H. S. Froes, *Met. Powder Rep.* 1 (2017).
- [6] E. Brandl, A. Schoberth, and C. Leyens, *Mater. Sci. Eng. A* **532**, 295 (2012).
- [7] H. M. Wang, S. Q. Zhang, and X. M. Wang, *Chin. J. Lasers* **36**, 3204 (2009).
- [8] F. G. Arcella and F. H. Froes, *JOM* **52**, 28 (2000).
- [9] H. Galarraga, R. J. Warren, D. A. Lados, R. R. Dehoff, M. M. Kirka, and P. Nandwana, *Mater. Sci. Eng. A* **685**, 417 (2017).
- [10] A. Mitchell, *Mater. Sci. Eng. A* **243**, 257 (1998).
- [11] W. E. Frazier, *J. Mater. Eng. Perform.* **23**, 1917 (2014).
- [12] B. Baufeld, O. Van der Biest, and R. Gault, *Mater. Des.* **31**, S106 (2010).
- [13] ASTM, *Rapid Manuf. Assoc.* 10 (2013).
- [14] I. Gibson, D. W. Rosen, and B. Stucker, *Additive Manufacturing Technologies* (Springer, n.d.).
- [15] W. Gao, Y. Zhang, D. Ramanujan, K. Ramani, Y. Chen, C. B. Williams, C. C. L. Wang, Y. C. Shin, S. Zhang, and P. D. Zavattieri, *Comput. Des.* **69**, 65 (2015).
- [16] B. Onuikwe and A. Bandyopadhyay, *Mater. Lett.* **252**, 256 (2019).
- [17] T. T. Wohlers, *Wohlers Report 2006: Rapid Prototyping & Manufacturing State of the Industry: Annual Worldwide Progress Report* (Wohlers Associates, 2006).
- [18] L. Hitzler, M. Merkel, W. Hall, and A. Öchsner, *Adv. Eng. Mater.* **20**, 1700658 (2018).
- [19] S. L. Sing, W. Y. Yeong, and F. E. Wiria, *J. Alloy. Compd.* **660**, 461 (2016).
- [20] Q. Jia and D. Gu, *J. Alloys Compd.* **585**, 713 (2014).
- [21] Y. Kuo, A. Kamigaichi, and K. Takechi, *Metall. Mater. Trans. A* **49**, 3831 (2018).
- [22] L. Hitzler, M. Merkel, W. Hall, and A. Öchsner, *Adv. Eng. Mater.* **20**, 1700658 (2018).
- [23] A. Saboori, F. Bosio, E. Librera, M. De Chirico, S. Biamino, M. Lombardi, and P. Fino, in *Euro PM2018 Congr. Exhibition* (Bilbao (Spain), 2018), pp. 1–6.
- [24] F. Bosio, A. Saboori, A. Lacagnina, E. Librera, M. De Chirico, S. Biamino, P. Fino,

- and M. Lombardi, in *Euro PM2018 Congr. Exhibition* (Bilbao (Spain), 2018), pp. 1–6.
- [25] S. Biamino, A. Penna, U. Ackelid, S. Sabbadini, O. Tassa, P. Fino, M. Pavese, P. Gennaro, and C. Badini, *Intermetallics* **19**, 776 (2011).
- [26] A. Atae, Y. Li, D. Fraser, G. Song, and C. Wen, *Mater. Des.* **137**, 345 (2018).
- [27] M. Ternier, S. Biamino, P. Epicoco, A. Penna, O. Hedin, S. Sabbadini, P. Fino, M. Pavese, U. Ackelid, P. Gennaro, F. Pelissero, and C. Badini, *Steel Res. Int.* **83**, 943 (2012).
- [28] Y. Zhong, L.-E. Rännar, L. Liu, A. Koptug, S. Wikman, J. Olsen, D. Cui, and Z. Shen, *J. Nucl. Mater.* **486**, 234 (2017).
- [29] D. Cormier, O. Harrysson, and H. West, *Rapid Prototyp. J.* **10**, 35 (2004).
- [30] Y. Zhai, H. Galarraga, and D. A. Lados, *Procedia Eng.* **114**, 658 (2015).
- [31] G. Baudana, S. Biamino, D. Ugues, M. Lombardi, P. Fino, M. Pavese, and C. Badini, *Met. Powder Rep.* **71**, 193 (2016).
- [32] K. Kyzioł, Ł. Kaczmarek, G. Brzezinka, and A. Kyzioł, *Chem. Eng. J.* (2014).
- [33] L. U. Larsson Morgan and H. Ola, *Solid Free. Fabr. Symp.* 438 (2003).
- [34] S. Price, J. Lydon, K. Cooper, and K. Chou, V02AT02A002 (2015).
- [35] C. Körner, E. Attar, and P. Heintl, *J. Mater. Process. Technol.* **211**, 978 (2011).
- [36] J. Milberg and M. Sigl, *Prod. Eng.* **2**, 117 (2008).
- [37] M. Galati and L. Iuliano, *Addit. Manuf.* **19**, (2018).
- [38] E. Attar, *Simulation of Selective Electron Beam Melting Processes*, 2011.
- [39] A. Safdar, L.-Y. Wei, A. Snis, and Z. Lai, *Mater. Charact.* **65**, 8 (2012).
- [40] W. He, W. Jia, H. Liu, H. Tang, X. Kang, and Y. Huang, *Xiyou Jinshu Cailiao Yu Gongcheng/Rare Met. Mater. Eng.* **40**, 2072 (2011).
- [41] Mahale, *Electron Beam Melting of Advanced Materials and Structures, Mass Customization, Mass Personalization*, 2009.
- [42] S. M. Gaytan, L. E. Murr, F. Medina, E. Martinez, M. I. Lopez, and R. B. Wicker, *Mater. Technol.* **24**, 180 (2009).
- [43] P. Heintl, A. Rottmair, C. Körner, and R. F. Singer, *Adv. Eng. Mater.* **9**, 360 (2007).
- [44] H. R. Vladimir Popov, Alexander Katz-Demyanetz, Andrey Garkun, Gary Muller, Evgeny Strokin, V. Popov, A. Katz-Demyanetz, A. Garkun, G. Muller, E. Strokin, and H. Rosenson, *Procedia Manuf.* (2018).
- [45] E. Hernández-Nava, C. J. Smith, F. Derguti, S. Tammam-Williams, F. Léonard, P. J. Withers, I. Todd, and R. Goodall, *Acta Mater.* **108**, 279 (2016).

- [46] S. Tammas-Williams, P. J. Withers, I. Todd, and P. B. Prangnell, *Scr. Mater.* **122**, 72 (2016).
- [47] T. Persenot, G. Martin, R. Dendievel, J.-Y. Buffière, and E. Maire, *Mater. Charact.* **143**, 82 (2018).
- [48] R. Cunningham, A. Nicolas, J. Madsen, E. Fodran, E. Anagnostou, M. D. Sangid, and A. D. Rollett, *Mater. Res. Lett.* **5**, 516 (2017).
- [49] S. Tammas-Williams, P. J. Withers, I. Todd, and P. B. Prangnell, *Metall. Mater. Trans. A* **47**, 1939 (2016).
- [50] L. E. Murr, S. A. Quinones, S. M. Gaytan, M. I. Lopez, A. Rodela, E. Y. Martinez, D. H. Hernandez, E. Martinez, F. Medina, and R. B. Wicker, *J. Mech. Behav. Biomed. Mater.* **2**, 20 (2009).
- [51] N. A. Fleck, V. S. Deshpande, and M. F. Ashby, *Proc. R. Soc. A Math. Phys. Eng. Sci.* **466**, 2495 (2010).
- [52] M. Suard, G. Martin, P. Lhuissier, R. Dendievel, F. Vignat, J. J. Blandin, and F. Villeneuve, *Addit. Manuf.* **8**, 124 (2015).
- [53] K. J. Maloney, K. D. Fink, T. A. Schaedler, J. A. Kolodziejska, A. J. Jacobsen, and C. S. Roper, *Int. J. Heat Mass Transf.* **55**, 2486 (2012).
- [54] A. G. Evans, J. W. Hutchinson, and M. F. Ashby, *Prog. Mater. Sci.* **43**, 171 (1998).
- [55] G. W. Kooistra, V. S. Deshpande, and H. N. G. Wadley, *Acta Mater.* **52**, 4229 (2004).
- [56] M. L. E., G. S. M., M. F., L. H., M. E., M. B. I., H. D. H., M. L., L. M. I., W. R. B., and B. J., *Philos. Trans. R. Soc. A Math. Phys. Eng. Sci.* **368**, 1999 (2010).
- [57] M. Niinomi, *Metall. Mater. Trans. A* **33**, 477 (2002).
- [58] J.-W. Park, H.-K. Kim, Y.-J. Kim, J.-H. Jang, H. Song, and T. Hanawa, *Acta Biomater.* **6**, 2843 (2010).
- [59] P. Heintz, L. Müller, C. Körner, R. F. Singer, and F. A. Müller, *Acta Biomater.* **4**, 1536 (2008).
- [60] X. Y. Cheng, S. J. Li, L. E. Murr, Z. B. Zhang, Y. L. Hao, R. Yang, F. Medina, and R. B. Wicker, *J. Mech. Behav. Biomed. Mater.* **16**, 153 (2012).
- [61] L. J. Gibson and M. F. Ashby, *Cellular Solids: Structure and Properties* (Cambridge university press, 1999).
- [62] M. F. Ashby, *Philos. Trans. R. Soc. A Math. Phys. Eng. Sci.* **364**, 15 (2006).
- [63] V. S. Deshpande, M. F. Ashby, and N. A. Fleck, *Acta Mater.* **49**, 1035 (2001).
- [64] J. C. Maxwell, London, Edinburgh, Dublin *Philos. Mag. J. Sci.* **27**, 294 (1864).
- [65] L. E. Murr, S. M. Gaytan, F. Medina, E. Martinez, J. L. Martinez, D. H. Hernandez, B.

- I. Machado, D. A. Ramirez, and R. B. Wicker, *Mater. Sci. Eng. A* **527**, 1861 (2010).
- [66] E. Hernández-Nava, C. J. Smith, F. Derguti, S. Tammas-Williams, F. Léonard, P. J. Withers, I. Todd, and R. Goodall, *Acta Mater.* **85**, 387 (2015).
- [67] A. Mortensen, Y. Conde, A. Rossoll, and C. San Marchi, *J. Mater. Sci.* **48**, 8140 (2013).
- [68] T. J. Horn, O. L. A. Harrysson, D. J. Marcellin-Little, H. A. West, B. D. X. Lascelles, and R. Aman, *Addit. Manuf.* **1**, 2 (2014).
- [69] O. Cansizoglu, O. Harrysson, D. Cormier, H. West, and T. Mahale, *Mater. Sci. Eng. A* **492**, 468 (2008).
- [70] J. Parthasarathy, B. Starly, S. Raman, and A. Christensen, *J. Mech. Behav. Biomed. Mater.* **3**, 249 (2010).
- [71] Z. Fang, B. Starly, and W. Sun, *Comput. Des.* **37**, 65 (2005).
- [72] B. Starly, A. Lau, W. Sun, W. Lau, and T. Bradbury, *Comput. Des.* **37**, 387 (2005).
- [73] J. Parthasarathy, B. Starly, and S. Raman, *J. Manuf. Process.* **13**, 160 (2011).
- [74] W. van Grunsven, E. Hernandez-Nava, G. Reilly, and R. Goodall, *Metals (Basel)*. **4**, 401 (2014).
- [75] M. Jamshidinia, L. Wang, W. Tong, and R. Kovacevic, *J. Mater. Process. Technol.* **214**, 1728 (2014).
- [76] M. Jamshidinia, L. Wang, W. Tong, R. Ajlouni, and R. Kovacevic, *J. Mater. Process. Technol.* **226**, 255 (2015).
- [77] G. Epasto, G. Palomba, D. D. Andrea, E. Guglielmino, S. Di, and F. Traina, *Mater. Sci. Eng. A* **753**, 31 (2019).
- [78] L. Xiao, W. Song, C. Wang, H. Liu, H. Tang, and J. Wang, *Mater. Sci. Eng. A* **640**, 375 (2015).
- [79] L. Yang, *Rapid Prototyp. J.* (2015).
- [80] L. Xiao, W. Song, C. Wang, H. Tang, Q. Fan, N. Liu, and J. Wang, *Int. J. Impact Eng.* **100**, 75 (2017).
- [81] S. J. Li, L. E. Murr, X. Y. Cheng, Z. B. Zhang, Y. L. Hao, R. Yang, F. Medina, and R. B. Wicker, *Acta Mater.* **60**, 793 (2012).
- [82] M. Karl and J. R. Kelly, *Dent. Mater.* **25**, 1426 (2009).
- [83] Y. Y. Sun, S. Gulizia, C. H. Oh, D. Fraser, M. Leary, Y. F. Yang, and M. Qian, *Jom* **68**, 791 (2016).
- [84] M. Suard, P. Lhuissier, R. Dendievel, J.-J. Blandin, F. Vignat, and F. Villeneuve, *Powder Metall.* **57**, 190 (2014).
- [85] K. S. Chan, M. Koike, R. L. Mason, and T. Okabe, *Metall. Mater. Trans. A* **44**, 1010

- (2013).
- [86] ASTM, **i**, 1 (2019).
- [87] C. De Formanoir, S. Michotte, O. Rigo, L. Germain, and S. Godet, *Mater. Sci. Eng. A* **652**, 105 (2016).
- [88] C. de Formanoir, M. Suard, R. Dendievel, G. Martin, and S. Godet, *Addit. Manuf.* **11**, 71 (2016).

## 6 List of figures

Figure 1: Thermal evolution in the EBM process [9].....	4
Figure 2: The range of properties available to the engineer through foaming: (a) density; (b) thermal conductivity; (c) Young modulus; (d) compressive strength [61].....	7
Figure 3: Optical micrographs showing different microstructures for a bulk material (a) and a foam (b) [65].....	8
Figure 4: charts summarizing the relationship between relative density and relative modulus of elasticity (a) and relative compressive strength (b) derived from Ti-6Al-4V cellular structures [68].....	10
Figure 5: Variation of Effective E as a function of porosity [73].....	11
Figure 6: Mechanical behaviour of the graded lattice structure [74].....	12
Figure 7: experimental results for relative Young modulus from literature.....	14
Figure 8: Nominal stress-strain curves for configuration 1 with an l/d ratio of 2.5 (a) and configuration 2 with an l/d ratio of 1.5 (b) [78].....	15
Figure 9: Nominal stress-strain curves at different temperature for configuration 1 (a,c,e) and configuration 2 (b,d,f) [78]. ....	16
Figure 10: Optical microstructure of the foams (a,b) and the lattice structures (c,d) from [60]. .....	17
Figure 11: a strain-cycles diagram showing the trends of strain accumulation for different load conditions [81]. ....	19
Figure 12: FESEM surface images of as-fabricated (a), surface-etched (b) and machined (c) specimens; surface conditions of as-fabricated (a'), surface-etched (b') and machined (c') specimens observed under Alicona IFM [83]. ....	21
Figure 13: images showing a global octet-truss unit cell (a), a 3D reconstruction of one strut (b) and an isometric view of a 1 mm strut (c) [84]. ....	22
Figure 14: (a) comparisons between the CAD design (in blue) and the build struts (in green) at different construction angles; (b) aspect ratio with respect to construction angle [52]. ....	23
Figure 15: Relative elastic modulus with respect to relative density for different strut sizes: green curve for DCAD, the red dashed curve for DEQNUM, the orange curve for DEQGEOM. Experimental results are depicted in black [52]. ....	24
Figure 16: CT scan images showing porosity in red; (a) as-built condition, (b) after HIP conditions [49]. ....	27

Figure 17: Optical micrograph of as-built condition (a) with three different locations of interest (b,c,d) [45].	29
Figure 18: unit cells types analysed in the present study.	32
Figure 19: general design of each specimen.	32
Figure 20: stereomicroscope images of each different specimen; the rows (from top to bottom) depict structures I, II and III, while the columns (from left to right) depict unit cell size of 4, 7 and 10 mm	34
Figure 21: schematic curve obtained with the compression test	35
Figure 22: temperature-time diagram for the two designed heat treatments	36
Figure 23: trends observed in the literature by Xiao et al. [78] (a), for structure II with unit cell of 4 mm (b) and for structure III with unit cell of 7 mm (c).	38
Figure 24: compressive trend for structure II with a unit cell size of 4 mm in the NTH condition	38
Figure 25: NTH compressive trends for structure I (a), structure II (b) and structure III (c)	40
Figure 26: compressive trends for unit cells of 4 mm (a), 7 mm (b) and 10 mm (c)	40
Figure 27: bi-logarithmic diagram showing the relationship between the relative Young modulus and the relative density	41
Figure 28: bi-logarithmic diagram showing the relationship between the relative UCS and the relative density	43
Figure 29: bi-logarithmic diagram showing the relationship between the relative absorbed energy up to failure and the relative density	44
Figure 30: microstructure of the I-4 design in the NTH condition at 3000x (a) and 5000x (b)	45
Figure 31: NTH, HT1 and HT2 trends observed regarding structure II with unit cell of 4 mm (a) and structure III with unit cell of 7 mm (c)	46
Figure 32: stress-strain trends for configuration 1 (a) and configuration 2 (b) studied by Xiao et al. [78]	47
Figure 33: compressive trend for structure III with unit cell size of 4 mm in the HT1 condition	47
Figure 34: compressive trends for structure I in the condition NTH (a), HT1 (b) and HT2 (c)	49
Figure 35: Young modulus values for the three analysed conditions.	50

Figure 36: bi-logarithmic diagram showing the relationship between the relative Young modulus and the relative density for conditions NTH (in black), HT1 (in blue) and HT2 (in red).....	51
Figure 37: Ultimate Compressive Strength values for the three analysed conditions .....	52
Figure 38: bi-logarithmic diagram showing the relationship between the relative Ultimate Compressive Strength and the relative density for conditions NTH (in black), HT1 (in blue) and HT2 (in red) .....	53
Figure 39: Elongation at failure values for the three analysed conditions .....	54
Figure 40: Absorbed energy up to failure values for the three analysed conditions .....	55
Figure 41: bi-logarithmic diagram showing the relationship between the relative absorbed energy up to failure and the relative density.....	56
Figure 42: SEM images showing the surface of the junction of the struts (a) and the surface of a single strut (b) for the design I-4 in the HT1 condition.....	57
Figure 43: microstructure of the I-4 design in the HT1 (a) and HT2 (b) conditions .....	58
Figure 44: microstructure of the I-4 design in the HT2 condition.....	58

## 7 List of tables

Table 1: Testing conditions for compression tests conducted in literature. ....	14
Table 2: Hardness Vickers of the cell for specimens tested by Cheng et al. [60]. ....	17
Table 3: values of CAD, numerical and geometrical equivalent diameters with respect to strut's construction angle [52]. ....	24
Table 4: results of tensile tests for both as-built and machined conditions from the study by Epasto et al. [77]. ....	25
Table 5: statistical data from the same sample in the five different conditions analysed [46]. ....	27
Table 6: Heat treatments on Ti-6Al-4V made by EBM found in the literature. In the present table FC stands for "furnace cooling", AC stands for "air cooling" and WC stands for "water cooling" ....	30
Table 7: geometrical features of each structure type, all the values have been extract from the Magic file. ....	33
Table 8: values of averages of measured mass, lattice mass and relative densities for each cell type and size ....	37
Table 9: average properties of each different sample's unit cell type and size evaluated for the NTH condition ....	39
Table 10: comparisons between some of the collected data with similar values of relative density ....	42
Table 11: average properties of each different sample's unit cell type and size evaluated for the HT1 and HT2 conditions ....	48

## Summary

<b>1</b>	<b>Literature Review .....</b>	<b>1</b>
1.1	Introduction.....	1
1.2	Mechanical behaviour of Ti-6Al-4V lattice structures made by EBM.....	6
1.2.1	<i>The behaviour of the lattice structure under compression test: experimental and numerical models.....</i>	<i>8</i>
1.2.2	<i>Effect of working temperature on the compression behaviour of the lattice structures .....</i>	<i>15</i>
1.2.3	<i>Hardness .....</i>	<i>17</i>
1.2.4	<i>The behaviour of the lattice structure under cyclic loads: fatigue investigations</i>	<i>18</i>
1.3	Effect of the precision of the EBM process and the surface roughness on the mechanical properties .....	19
1.4	Effects of thermal treatments on the mechanical behaviour of Ti-6Al-4V alloy made by EBM .....	26
1.5	Objective.....	31
<b>2</b>	<b>Design of the experiments .....</b>	<b>32</b>
2.1	Lattice design.....	32
2.2	Production.....	33
2.3	Compression test.....	34
2.4	Heat treatments .....	36
2.5	Characterization.....	37
<b>3</b>	<b>Results and discussion .....</b>	<b>38</b>
3.1	Mechanical behaviour of as-built lattice structures .....	38
3.1.1	<i>Compressive trends.....</i>	<i>38</i>
3.1.2	<i>Effect of the cell size .....</i>	<i>40</i>
3.1.3	<i>Effect of the cell type.....</i>	<i>40</i>
3.1.4	<i>Young modulus.....</i>	<i>41</i>
3.1.5	<i>Ultimate Compressive Strength .....</i>	<i>43</i>

3.1.6	<i>Absorbed energy up to failure</i>	44
3.1.7	<i>Microstructure analysis</i>	45
3.2	Mechanical behaviour of heat-treated lattice structures	46
3.2.1	<i>Compressive trends</i>	46
3.2.2	<i>Effect of the cell size and type</i>	49
3.2.3	<i>Young modulus</i>	50
3.2.4	<i>Ultimate Compressive Strength</i>	51
3.2.5	<i>Elongation at failure</i>	53
3.2.6	<i>Absorbed energy up to failure</i>	54
3.2.7	<i>Microstructure analysis</i>	57
<b>4</b>	<b>Conclusions</b>	<b>60</b>
<b>5</b>	<b>References</b>	<b>62</b>
<b>6</b>	<b>List of figures</b>	<b>67</b>
<b>7</b>	<b>List of tables</b>	<b>70</b>